Title
Synthesis and Spectroscopy of Aluminum Molecules and Materials for Investigating Electronic Structure in f-Element-Aluminum Bimetallics

Author
Altman, Alison Beth

Publication Date
2017

Peer reviewed|Thesis/dissertation

Synthesis and Spectroscopy of Aluminum Molecules and Materials for Investigating Electronic Structure in f-Element-Aluminum Bimetallics

By

Alison Beth Altman

A dissertation submitted in partial satisfaction of the
requirements for the degree of
Doctor of Philosophy
in
Chemistry
in the
Graduate Division
of the
University of California, Berkeley

Committee in Charge:

Professor John Arnold, Chair
Professor Angelica Stacy
Professor Jeffrey Reimer

Summer 2017

Abstract

Synthesis and Spectroscopy of Aluminum Molecules and Materials for Investigating Electronic Structure in f-Element-Aluminum Bimetallics

By

Alison Beth Altman

Doctor of Philosophy in Chemistry

University of California, Berkeley

Professor John Arnold, Chair

Chapter 1:

Polarized aluminum K-edge X-ray Absorption Spectroscopy (XAS) and first principle calculations were used to probe electronic structure in a series of (BDI)Al, (BDI)AlX_2, and (BDI)AlR_2 coordination compounds (X = F, Cl, I; R = H, Me; BDI = 2,6-diisopropylphenyl-β-diketiminate). Spectral interpretations were guided by examination of the calculated transition energies and polarization-dependent oscillator strengths, which agreed well with the XAS measurements. Pre-edge features were assigned to transitions associated with the Al 3p orbitals involved in metal–ligand bonding. Qualitative trends in core energy and valence orbital occupation were established through a systematic comparison of excited states derived from Al 3p orbitals with similar symmetries in a molecular orbital framework. These trends suggested that the higher transition energies observed for (BDI)AlX_2 systems with more electronegative X^{1-} ligands could be ascribed to a decrease in electron density around the aluminum atom, which causes an increase in the attractive potential of the Al nucleus and concomitant increase in the binding energy of the Al 1s core orbitals. For (BDI)Al and (BDI)AlH_2 the experimental Al K-edge XAS spectra and spectra calculated using the eXcited electron and Core-Hole (XCH) approach had nearly identical energies for transitions to final state orbitals of similar composition and symmetry. These results implied that the charge distributions about the aluminum atoms in (BDI)Al and (BDI)AlH_2 are similar relative to the (BDI)AlX_2 and (BDI)$AlMe_2$ compounds, despite having different formal oxidation states of +1 and +3, respectively. However, (BDI)Al was unique in that it exhibited a low-energy feature that was attributed to transitions into a low-lying p-orbital of b_1 symmetry that is localized on Al and orthogonal to the (BDI)Al plane. The presence of this low energy unoccupied molecular orbital on electron-rich (BDI)Al constitutes a more distinguishing aspect of its valence electronic structure relative to the formally trivalent compounds (BDI)AlX_2 and (BDI)AlR_2. The work shows that Al K-edge XAS can be used to provide valuable insight into electronic-structure to reactivity relationships for main-group coordination compounds.

Chapter 2:

Oxygen and aluminum K-edge XAS, imaging from a scanning transmission X-ray microscope (STXM), and first principles calculations were used to probe the composition and morphology of bulk aluminum metal, α- and γ-Al_2O_3, and several types of aluminum nanoparticles. The imaging results agreed with earlier transmission electron microscopy studies that showed a 2 to 5 nm thick layer of Al_2O_3 on all the Al surfaces. Spectral interpretations were guided by examination of the calculated transition energies, which agreed well with the spectroscopic measurements. Features observed in the experimental O and Al K-edge XAS were used to determine the chemical structure and phase of the Al_2O_3 on the aluminum surfaces. For unprotected 18 and 100 nm Al nanoparticles, this analysis revealed an oxide layer that was similar to γ-Al_2O_3 and comprised of both tetrahedral and octahedral Al coordination sites. For oleic-acid

protected Al nanoparticles, only tetrahedral Al oxide coordination sites were observed. The results were correlated to trends in the reactivity of the different materials, which suggests that the structures of different Al_2O_3 layers have an important role in the accessibility of the underlying Al metal towards further oxidation. Combined, the Al K-edge XAS and STXM results provided detailed chemical information that was not obtained from powder X-ray diffraction or imaging from a transmission electron microscope.

Chapter 3:

Correlated electron phenomena in lanthanide and actinide materials are driven by a complex interplay between the f and d orbitals. In this study, aluminum K-edge XAS and Density Functional Theory calculations were used to evaluate the electronic structure of the dialuminides, MAl_2 (M = Ce, Sm, Eu, Yb, Lu, U, and Pu). The results showed how the energy and occupancy of the 4f or 5f orbitals impacted mixing of Al 3p character into the 5d or 6d conduction bands, which has implications for understanding the magnetic and structural properties of correlated electron systems.

Chapter 4:

The synthesis and reactivity of paramagnetic heterometallic complexes containing a Ti(III)-μH-Al(III) moiety are presented. Combining different stoichiometries of Cp_2TiCl and $KH_3AlC(SiMe_3)_3$ (Cp = cyclopentadienyl) resulted in the formation of either bimetallic $Cp_2Ti(\mu\text{-}H)_2(H)AlC(SiMe_3)_3$ or trimetallic $(Cp_2Ti)_2(\mu\text{-}H)_3(H)AlC(SiMe_3)_3$ *via* salt metathesis pathways. While these complexes were indefinitely stable at room temperature, the bridging hydrides were readily activated upon exposure to heteroallenes, heating, or electrochemical oxidation. In each case, formal hydride oxidation occurred, but the isolated product maintained the +3 oxidation state at both metal centers. The nature of this reactivity was explored using deuterium labelling experiments and Density Functional Theory (DFT) calculations. It was found that while C-H activation from the Ti(III) bimetallic may occur through a σ-bond metathesis pathway, chemical oxidation to Ti(IV) promotes bimolecular reductive elimination of dihydrogen to form a Ti(III) product.

Chapter 5:

Here, we present the synthesis of a low-valent thorium heterobimetallic containing the Th(III)-μH-Al(III) motif *via* reduction of a Th(IV)Cl precursor, as well as the direct synthesis by salt metathesis of a uranium(III) aluminum heterobimetallic analogue. These complexes were structurally characterized and compared using electron paramagnetic resonance techniques to a related titanium(III) system, and evidence was found for significant aluminum participation in the orbital occupied by the unpaired electron in the thorium system. DFT calculations confirmed the Th→Al character of this interaction.

Synthesis and Spectroscopy of Aluminum Molecules and Materials for Investigating Electronic Structure in f-Element-Aluminum Bimetallics

Table of Contents

Preface

Background. Bimetallic molecules and materials have the potential to address some of the long-standing challenges of inorganic chemistry. By putting two metal centers in electronic contact, either through direct bonds or electron delocalization, the electronic behavior of the system expands, allowing it to perform chemical transformations that challenge typical understanding of the behavior of each metal on its own. The advantage of this is evident in small molecule activation chemistry of which there are an increasing number of reports of using bimetallics containing early or first row transition metals to perform chemistry most commonly observed in precious metal systems (*Dalton Trans.,* 2017, **46**, 5472-5473). Additionally, bimetallics have historically been foundational in developing new models of inorganic electronic structure and magnetism. Specifically, compounds containing metal-metal bonds have been fruitful systems for fine-tuning models of metal bonding because they often highlight covalent interactions which can be otherwise obscured by electrostatic forces (Cotton, F. A.; Murillo, C. A.; Walton, R. A. *Multiple Bonds Between Metal Atoms*, 3rd ed.; Springer Science: New York, NY, 2005). Although bimetallics are inherently complicated systems whose properties are governed by convoluted and competing factors, they are particularly amenable to characterization by element specific spectroscopy which give insight into the overall electronic structure filtered through a single metal's perspective. Such models and techniques provide not just a framework for understanding the reactivity observed in these systems, but also inform design principles for targeting new chemistry.

One area of inorganic chemistry that could benefit from increased understanding and chemical control is actinide and lanthanide research. Of particular current interest is the safe handling of the f-elements during nuclear energy processing and waste remediation. Small differences in covalent bonding have been evoked to explain successful methods for separating lanthanides from actinides. However, the limited examples of f-element complexes compared with s, p and d element compounds inhibit development of new design principles. Furthermore, chemical intuition informed by transition metal behavior is not sound in predicting lanthanide and actinide chemistry due to the unique involvement of f-orbitals and the expanded coordination sphere. The need for nuanced models of bonding specific to f-elements makes lanthanide and actinide bimetallics of particular interest as a productive target of basic research that may have a large impact on applied chemistry.

We hypothesized that aluminum would be able to interact covalently with f-elements due to the sizes and energies of its valence orbitals. While examples of f-element–metal bonds in molecular systems are limited, low-valent aluminum molecules have been shown to coordinate both lanthanides and actinides, although new types of synthesis and characterization are needed to further elucidate bonding modes and potential reactivity (*J. Am. Chem. Soc.* **2009**, *131*, 13767-13783). Such molecular bimetallics would be interesting model complexes for f-element aluminum alloys, which are known for their unusual properties that vary greatly across the both the lanthanide and actinide series (*Phys. Rev. B.* **1985**, *31*, 3251-3259). This work presents our efforts in developing methods of synthesizing and characterizing f-element–aluminum bimetallics to expand their chemistry and gain insight into their fundamental nature.

Research. The first part of this work (Chapters 1-3) describes the development of Al K-edge X-ray Absorption Spectroscopy (XAS) as a probe of electronic structure. Al K-edge XAS had previously been limited to aluminum materials of geological significance which demonstrated edge energies and shape resonances diagnostic of geometry at the aluminum centers. Therefore, it

was necessary to systematically expand the range of analytes in order to build up methods for interpreting new systems. By beginning with simple aluminum molecules, molecular orbital theory supported by spectral simulations was used to understand how differences in aluminum oxidation state and ligand environment affected the observed spectra (Chapter 1). A combined XAS and density functional theory study of simple aluminum materials revealed how this understanding could be translated to a band structure and density of states framework (Chapter 2). Together, these chapters laid the foundation for using Al K-edge XAS to evaluate the electronic structure of multimetallic materials (Chapter 3). For the isostructural MAl_2 alloys (M= Ce, Sm, Eu, Yb, Lu, U, and Pu), Al K-edge spectra showed that while M f orbitals are not directly involved in bonding, they do perturb the energy of the M d orbitals which determines the composition of their conduction band and affects their magnetic properties.

Together, these studies found evidence that aluminum orbitals engage in hybridization and covalent interactions, such that spectroscopic signatures did not correlate exactly with formally assigned oxidation states. Specifically, it was observed that trivalent aluminum hydride complexes can support a significant build-up of charge at the aluminum center that would ease the energetic requirements for reduction chemistry. The second part of this work (Chapters 4-5) explores the implications of these results through the synthesis of molecular aluminum bimetallics. For these studies, two projects were pursued in parallel: Chapter 4 describes the synthesis and reactivity of a titanium aluminum bimetallic based on a Ti-μH-Al motif and Chapter 5 describes syntheses of thorium and uranium structural analogues as well as an electron paramagnetic resonance (EPR) comparison of their electronic structure. It was initially hypothesized that such compounds could be precursors to metal-metal bonded complexes through hydride oxidation and metal reduction. While hydrogen evolution was never shown to result in unsupported metal-metal bonded complexes, these complexes tolerated other low-valent chemistry. Although titanium and thorium are most commonly found in the +4 oxidation state with no valence electrons, the aluminum containing alanate ligand supported reduced M(III) systems, allowing for the isolation of a thorium (III) heterobimetallic, and a titanium (III) bimetallic that underwent reductive elimination of hydrogen upon oxidation. EPR studies of the low-valent bimetallics showed that the unpaired electron in these systems was delocalized to varying extent onto the aluminum, allowing the bimetallic to support greater electron density than typically found for either metal alone.

While the sensitivity of these systems limits their practical applications, they expand the range of bonding observed in f-element chemistry. Previously reported f-element–aluminum bimetallics relied on low valent aluminum centers that participated in dative M←Al bonding interactions. In comparison, the complexes described in this work employ trivalent aluminum precursors that engage in M→Al interactions. Furthermore, by using established metal halides starting materials and robust salt metathesis pathways for synthesis, this procedure is amenable to systematic modification that may be used to further tease out subtle factors affecting electronic structure. Thus, these aluminum bimetallics serve as a powerful platform for gaining insight into fundamental questions of f-element bonding.

Acknowledgements

There is a myriad of people who this document would not exist without and deserve my gratitude, but I would like to begin by thanking Jim Haley, my high school chemistry teacher, who taught me to be proud of the small sphere of understanding that I gained through his guidance. From him I learned how to learn about chemistry, and that is the framework on which all of this that follows is built.

This is ultimately a story about education, and many teachers from both Yale and Berkeley have been instrumental in fostering my chemical curiosity. I am especially grateful to Professor McBride for his unique perspective on organic chemistry, and Professor Hazari for making chemistry seem a lot less impersonal. Professor Crabtree was kind enough to offer me the training and freedom to be unproductive for two years in his group, which I attribute to allowing me to be somewhat productive subsequently. Similarly, I must thank Laura Allen for her endless patience and enthusiasm which I did very little to deserve. She taught me perhaps the most important lesson of this endeavor, which is that mistakes are not just inevitable, they are (mostly) fixable.

Once I started graduate school, I was lucky enough to have found three advisors who generously assumed responsibility for ensuring my success and invested significantly in teaching me how to perform research. David Shuh worked tireless to make sure I had the resources I needed, while John Arnold gave me the freedom and connections to explore all my interests and Stefan Minasian pushed me to search for a fundamental (and well-articulated) understanding of my results. Many thanks to all of you for teaching me through the great examples you set of performing rigorous and significant science.

Of course, a large component of this work relied on hands-on physical skills, and the Arnold group has my eternal gratitude for providing a supportive home for this work. Each member of the group left an indelible mark on my graduate career, from Ashleigh Ward who taught me Schlenk technique to Bernard Parker who dealt with the "scary things." Also, this chemistry would not have survived without the attention and efforts of Michael and Jessica to the care for our glovebox.

I would especially like to thank Alex Brown who is directly and indirectly responsible for multiple portions of this thesis. Rewarding is far too self-congratulatory a description of the two and half years she listened to me tell her what to do (i.e. take all her starting material) in the guise of a mentee-mentor relationship. Alex, you are the most fearless chemist I know, and it was truly inspirational to have worked along-side you.

This work was hugely collaborative and would also not exist without the tireless efforts of my many collaborators. Firstly, the beamline scientists Tolek Tyliszczak, Jian Wang and David Vine fixed my many mistakes and just made things work. Trevor Lohrey showed impressive dedication to often thorny crystallographic problems, while David Prendergast and Das Pemmaraju were patient teachers of theoretical chemistry techniques and provided new perspective on the important parts of this work. Additionally, Guodong Rao and David Britt, who were later acquaintances in this project, made skilled contributions that profoundly changed the way I thought about these results. There are numerous other people at Berkeley who are true experts in their field and I am deeply appreciative of the culture of generosity and teaching fostered throughout the department. I would also like to thank Professors Stacy and Reimer for being supportive committee members and helping me through the qualifying and thesis writing process.

While each of these people provided a vital contribution for making my graduate school experience a fulfilling one, there are numerous others who were instrumental in making it an enjoyable one as well. I would like to thank all members of the cookbook club for being awesome

cooks and better company (the importance of Matt and Charlene's Emilia's pizza nights cannot be overstated). Also, thank you Oakland farmer's market raspberry guy and Song tea for the fuel to write this thesis, as well as Geoffrey Suguitan for balancing out all these food adventures.

Lastly, because graduate school is hard in often surprising ways, I would like to thank the people who provided continuous and unmitigated support; it is not an exaggeration to say I would not have finished this without you. My parents and my brother (and Posie) were always happy to see me, especially when it seemed like this chemistry was being particularly perverse. Thank you for continuing to spoil me. Lastly, lastly, there is Jared whose support was as constant and vital as air is for breathing (I swear that even though I am an inorganic chemist, that is a compliment). Your fingerprints are all over this document.

Chapter 1

Theory and X-ray absorption spectroscopy for aluminum coordination compounds: Al K-edge studies of charge and bonding in (BDI)Al, (BDI)AlR_2, and (BDI)AlX_2 complexes

Overview

Low-valent aluminum molecules have unique electronic structures making them useful synthons for forming dative aluminum-metal bonds. However, due to the high reactivity of such electron rich complexes, syntheses are challenging and limited. The following chapter covers efforts to understand the electronic structure and develop spectroscopic signatures of a low valent aluminum coordination compound compared with trivalent structural analogues. It was found that while the Al(I) complex have unique frontier orbitals, there is not a significant increase in charge at the aluminum center compared with an analogous Al(III) dihydride. These results explain how specific aluminum hydrides undergo reduction chemistry under mild conditions which has important implications for expanding their chemistry. This work has been recently published: A. B. Altman, C. D. Pemmaraju, C. Camp, J. Arnold, S. G. Minasian, D. Prendergast, D. K. Shuh and T. Tyliszczak "Theory and X-ray absorption spectroscopy for aluminum coordination complexes – Al K-edge studies of charge and bonding in (BDI)Al, (BDI)AlR_2, and (BDI)AlX_2 complexes." *J. Am. Chem. Soc.* 2015, **137**, 10304-10316.

Introduction

Aluminum is the most abundant metal in the earth's crust, and an essential component of many scientific and large-scale industrial processes. With steady improvements in production efficiency and manufacturing methods, aluminum metal is likely to replace other metals in applications owing to its desirable physical and mechanical properties, low cost, relatively-low toxicity, and recyclability.[1] At present, intermetallics, alloys, and compounds of aluminum are widely employed in d- and f-block materials science,[2] nanomaterials synthesis,[3,4] and solid-state lighting devices.[5] Aluminum coordination compounds are also valued participants in chemical transformations where they can activate substrates during Friedel-Crafts alkylations and during Ziegler-Natta olefin polymerizations where aluminum organometallic derivatives such as methylaluminoxane are commonly used as cocatalysts.[6,7] More recently, aluminum containing molecules were paired with phosphines possessing sterically-demanding ligands to activate CO_2 for reduction to CO.[8,9] In many of these systems, aluminum was regarded as a redox inert, electropositive, Lewis-acidic metal with a formal +3 charge and small ionic radius. However, this simple model was found to be inadequate for describing electronic structure in several instances. For example, low-valent aluminum coordination compounds,[10-17] often with double or triple bonds involving the aluminum atoms,[18-20] were isolated and characterized in depth by a variety of techniques including NMR[21-23] and reactivity studies.[24-28] Together with computational[29-35] and spectroscopic[36-41] techniques, this led to improved models of aluminum electronic structure grounded in molecular orbital theory. Some compounds containing aluminum in the +1 formal oxidation state exhibit singlet carbene character: they possess a nonbonding pair of electrons and behave as Lewis bases[42,43] and can undergo oxidative reactions readily with organic and main-group molecules.[14,29,42,44-47] More recent work by Nikonov,[48] Fischer[49] and Crimmin[50] showed that specific oxidative reactions were reversible, allowing for reductive elimination from an Al compound with a +3 formal oxidation state to form a Al compound with a +1 formal oxidation state. Along similar lines, work by Berben and coworkers showed that aluminum compounds supported by non-innocent ligands had tunable reduction potentials based on the electronics of the ancillary ligands, demonstrating reactivity and physical properties that were previously reserved for redox-active d-block transition metals.[51-56] Clearly, more powerful analytical techniques are needed to evaluate current models of electronic structure and understand the diverse and expanding role aluminum plays across chemical synthesis,

materials science and technology.

Metal K-edge X-ray Absorption Spectroscopy (XAS) is a widely used technique for probing changes in geometry, ligand environment and oxidation state in coordination compounds and materials.[57-62] For d-block metals, K-edge XAS probes both dipole-allowed transitions from the core 1s → empty *n*p orbitals, as well as weaker quadrupole-allowed transitions to the *n*d orbitals (*n* = principle quantum number) from which most bonding information is derived.[63] In principle, aluminum K-edge XAS can also be used to extract valuable information because the Al 3p valence orbitals are directly involved in bonding. However, earlier efforts to measure, model, and interpret Al K-edge XAS data were limited[64-71] because the intermediate energy regime that includes the Al K-edge (ca. 1555 – 1585 eV)[72] had historically been difficult to access at many synchrotron radiation facilities and beamlines. As a result, Al K-edge measurements were often subject to poor energy resolution, reduced X-ray photon flux, and incompatible sample preparation methodologies that resulted in self-absorption and saturation effects. Furthermore, there are few series of stable aluminum compounds that exhibit a wide range of ligand environments and formal oxidation states while preserving structural similarities that are desirable for systematic spectroscopic studies.

The results provided herein show that these challenges could be overcome for a series of molecular aluminum complexes with 2,6-diisopropylphenyl-β-diketiminate (BDI) supporting ligands. This ligand system was chosen because it provided access to a series of structurally-related (BDI)AlR_2 and (BDI)AlX_2 complexes (R = H, Me; X = F, Cl, I) in addition to (BDI)Al, which is a rare example in the literature of an monomeric aluminum(I) complex that is stable at room temperature and isolable in the solid state.[13,73-75] The work took advantage of several recent advances in synchrotron radiation instrumentation including the development of scanning transmission X-ray microscopes (STXMs) and diffraction grating monochromators capable of reaching more than 2 keV, now installed at many beamlines.[76-79] Pre-edge transitions in the aluminum K-edge XAS spectra of crystalline samples were experimentally identified through an in-depth comparison of the polarization dependence of transition intensities. The assignments were further confirmed using first-principles density functional theory calculations within the eXcited electron and Core-Hole (XCH) approach.[80] Comparison of transitions into comparable excited states of (BDI)Al and (BDI)AlH_2 revealed only slight differences in electron density on the Al atoms relative to (BDI)AlMe_2 and (BDI)AlX_2 (X = F, Cl, I), which has important implications for understanding the reductive and oxidative reactivity of aluminum coordination compounds.

Results and Discussion

Ground State Electronic Structure and Molecular Orbital Description. β-diketiminate groups are frequently employed as ancillary ligands in coordination chemistry because they provide steric stabilization and desirable solubility properties but do not participate in chemical transformations.[81] Aluminum complexes based on the β-diketiminate ligand were selected for this study because they provided access to a series of structurally-related (BDI)Al, (BDI)AlR_2 and (BDI)AlX_2 complexes (R = H, Me; X = F, Cl, I) with relatively high symmetries (Figure 1.1). These materials were analyzed to evaluate how changing the steric and electronic properties of the reactive R^{1-} or X^{1-} ligands or changing the aluminum formal oxidation state from +1 to +3 affected the aluminum K-edge spectra. In addition, (BDI)Al is the only published example of a monomeric low-valent aluminum compound that is stable and isolable at room temperature. This facilitated comparisons with the +3 compounds without introducing Al–Al

bonds that are typically found in other Al^{1+} compounds.[82-84]

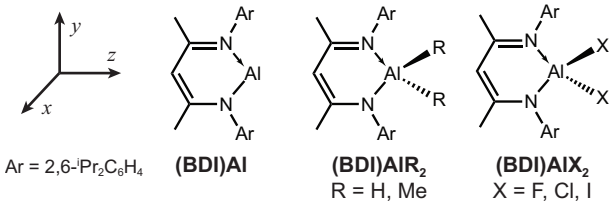

Figure 1.1. Representation of the (BDI)Al, (BDI)AlR_2 and (BDI)AlX_2 analytes and Cartesian axes system.

Before discussing the Al K-edge XAS in detail, it is instructive to provide a framework for evaluating molecular orbital interactions in each complex. Expectations from group theory were derived for (BDI)Al, (BDI)AlR_2 and (BDI)AlX_2 compounds assuming a C_{2v}-symmetric geometry. We note that the experimentally-determined solid-state structures deviated to varying extents from this idealized coordination environment (Table 1.1). However, based on this approximation, it was possible to develop the qualitative molecular orbital picture presented in Figure 1.2 with the relevant core and valence orbitals that were necessary for initial assignment of Al K-edge XAS spectral features. Beginning with the $(BDI)^{1-}$ ligand, the nitrogen 2p orbitals that are directed towards the metal-coordination site combine to form orbitals of a_1 and b_2 symmetry, and those that are perpendicular to the ligand plane have a_2 and b_1 symmetry. In C_{2v}-symmetry, the Al 3s orbital has a_1 symmetry, while the Al 3p orbitals span $b_1 + a_1 + b_2$ symmetries. With these designations, the ligand and metal orbitals combine to form an Al 3s-based HOMO of a_1 symmetry, and a low-lying Al 3p-based unoccupied orbital of b_1 symmetry (Figure 1.3). In this picture, the HOMO is directed away from the BDI ligand and is capable of σ-donation, while the vacant b_1* orbital is orthogonal to the (BDI)Al plane and resides at low energy relative to the other antibonding orbitals. In this sense, (BDI)Al is reminiscent of $(C_5Me_5)Al$ in that it is formally isolobal with carbon monoxide and singlet carbenes.[84] The remaining Al 3p orbitals of a_1 and b_2 symmetry interact with ligand orbitals of appropriate symmetry to form unoccupied and antibonding a_1* and b_2* orbitals. It is important to note that the filled Al 3s-based HOMO of a_1 symmetry can also mix with the unoccupied and antibonding Al 3p-based orbital of a_1 symmetry, and previous calculations have suggested that s-p_z mixing is a relevant factor and results in some stabilization of the a_1* orbital.[85] Thus, for the (BDI)Al system, it was predicted that three features would be observed corresponding to transitions into the $1b_1$*, $2a_1$* and $1b_2$* orbitals at increasing energies as shown in the first column of Figure 1.2.

Table 1.1. Relevant bond distances (Å) and angles (°) of (BDI)Al and (BDI)AlL$_2$ compounds (L = H, Me, F, Cl, I).

Compound	Ave Al-N distance (Å)	Ave Al-L Distance (Å)	N-Al-N Angle (°)	X-Al-X Angle (°)	BDI plane-Al Distance (Å)	BDI-BDI plane Angle (°) [a]
(BDI)Al	1.958(1)	–	89.86(8)	–	0.010	15.49
(BDI)AlH$_2$	1.899(1)	1.52(1)	96.41(5)	113(1)	0.006	11.56
(BDI)AlMe$_2$	1.929(2)	1.965(2)	96.2(1)	117.4(1)	0.721	24.59
(BDI)AlF$_2$	1.866(1)	1.652(1)	99.30(6)	107.81(6)	0.001	12.68
(BDI)AlCl$_2$	1.8752(6)	2.1265(3)	99.36(4)	108.02(2)	0.525	49.82
(BDI)AlI$_2$	1.877(1)	2.5220(4)	100.07(6)	108.41(2)	0.600	0

[a] The BDI-BDI plane angle reflects the alignment of molecules within the unit cell between non-symmetry related molecules.

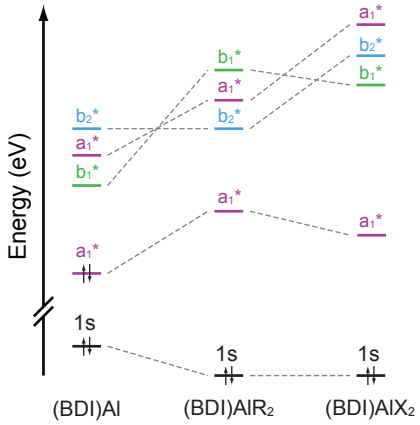

Figure 1.2. Qualitative molecular orbital diagram showing the relationship between (BDI)Al, (BDI)AlR$_2$ (R = H, Me), and (BDI)AlX$_2$ (X = F, Cl, I).

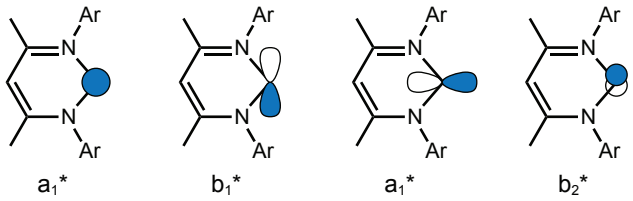

Figure 1.3. Representation of the Al 3s and 3p hybrid orbitals for (BDI)Al.

Molecular orbitals for each of the (BDI)AlR$_2$ and (BDI)AlX$_2$ compounds can be considered a perturbation of those derived for the (BDI)Al compound by first introducing interactions with the reactive R^{1-} and X^{1-} ligands, and by then considering the change in Al formal charge and orbital occupation. Group theory shows that the σ donating orbitals on the R^{1-} and X^{1-} ligands combine to form orbitals of a_1 and b_1 symmetry. These have the correct symmetry to interact with and destabilize the (BDI)Al fragment orbitals of a_1 and b_1 symmetry derived above. Interaction with the strictly σ-bonding ligands does not affect the $1b_2$* orbital energy; however, some destabilization would be expected for the (BDI)AlX$_2$ complexes due to

π-interactions with the halide ligands. Within this framework, some hybridization of the Al 3s (a_1) and Al $3p_z$ (a_1) orbitals is also possible through s-p mixing. Since the Al 3s orbitals are unoccupied in the (BDI)AlR_2 and (BDI)AlX_2 compounds, this introduces the opportunity for a fourth transition into an additional orbital of a_1 symmetry that is filled for (BDI)Al. Finally, the Al 1s core level is expected to be more stabilized in the (BDI)AlR_2 and (BDI)AlX_2 compounds than in (BDI)Al due to the increase in effective nuclear charge.[63] Thus, it was anticipated that features for compounds with Al^{3+} centers would be higher in energy overall than those observed for the (BDI)Al compound.

Sample preparation and imaging. The STXM at the Molecular Environmental Science beamline 11.0.2 of the ALS was used to collect images, elemental maps, and Al K-edge XAS spectra for each of the compounds described above. Samples were prepared in an argon-filled glovebox, and the STXM was filled with a partial atmosphere of helium during acquisition to minimize degradation of the air- and water-sensitive compounds. Figure 1.4 shows representative contrast images and Al elemental maps of small crystalline particles.

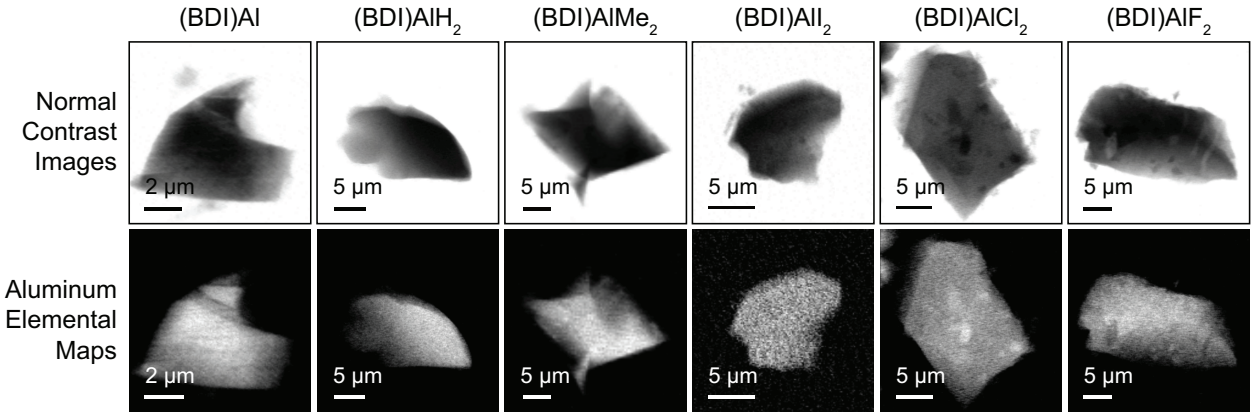

Figure 1.4. Images from the crystallites of (BDI)Al, (BDI)AlR_2, and (BDI)AlX_2 from which Al K-edge XAS spectra were obtained: top row, normal contrast images obtained with photon energies of 1565 eV; bottom row, aluminum elemental maps obtained by subtraction using photon energies of 1565 and 1555 eV.

Al K-edge measurements and data reduction. Figure 1.5 shows the background subtracted and normalized Al K-edge spectra obtained for crystalline samples of (BDI)Al, (BDI)AlR_2 and (BDI)AlX_2 complexes (R = H, Me; X = F, Cl, I). The spectra exhibited some similarities to those observed previously for Al oxides and materials in that a large edge was observed between 1559 and 1566 eV,[64,67,86] and different in that several well-resolved pre-edge features were also apparent at low energy. These were associated with dipole-allowed transitions from the Al 1s orbital into unoccupied orbitals with Al 3p character. Moreover, in many cases aspects of the symmetry of the individual molecules were preserved by the overall crystal symmetry such that the polarized X-ray beam interacted anisotropically with each particle and relative spectral intensities changed with the changing polarization of the X-ray beam (see Experimental Details). These changes were consistent with spectral assignments in that features observed at different polarizations were assigned to orbitals of different symmetry.

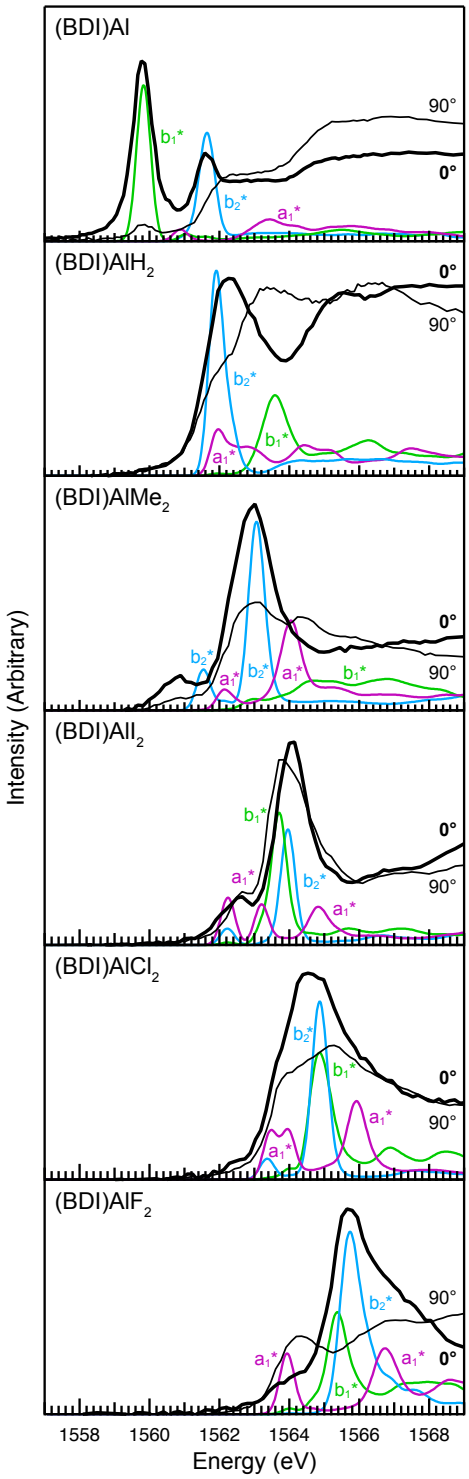

Figure 1.5. Aluminum K-edge XAS spectra with horizontal (0°, solid black trace) and vertical (90°, dashed black trace) light polarization settings. XCH calculated spectra are overlaid on the experimental data and are split into directional components based on the b_1* (green), b_2* (blue), and a_1* (purple) final state orbitals in idealized C_{2v} symmetry.

To accurately determine peak energies, spectra were modeled using pseudo-Voigt line shapes and a step function (see Table 1.2 and Experimental Details).[87] First and second derivatives of the experimental data were used as a guide to derive curve-fitting models and suggested that the pre-edge regions in all spectra were best modeled by 2 to 4 functions. The curve-fitting models were also examined to ensure consistency for a given analyte regardless of sample orientation or beam polarization. In each case, these analyses provided high quality fits of the experimental data as reflected by low correlation coefficients, residual data that deviated slightly from zero and symmetric residual peaks that matched well with the parent pseudo-Voigt functions. For (BDI)AlH_2, a fully unconstrained deconvolution did not converge with reasonable parameters that were consistent for different polarizations. Therefore, to obtain a realistic and consistent model, the energy of the step function for the horizontally polarized spectrum was constrained to match that for the vertically polarized spectrum. Similarly, to obtain a realistic fit of the horizontal spectrum of (BDI)AlF_2, the widths of the functions at 1566.5(3) and 1567.8(3) eV were constrained to less than 0.9 eV.

Table 1.2. Comparison of experimental and calculated Al K-edge energies to given final state orbitals in idealized C_{2v} symmetry for (BDI)Al, (BDI)AlR_2 and (BDI)AlX_2 (R = H, Me, X = F, Cl, I).

	Final State	Transition Energy (eV)	
Compound	Orbital	Exptl[a]	Calcd[b]
(BDI)Al	b_1	1559.8(2)	1559.8
	a_1	[c]	1560.9
	b_2	1561.7(2)	1561.6
(BDI)AlH_2	b_2	1561.9(2)	1561.9
	a_1	1562.8(2)	1563[d]
	b_1	1564.5(2)	1563.6
(BDI)$AlMe_2$	b_2	1560.8(2)	1561.5
	a_1	1562.4(2)	1562.1
	b_2	1563.0(2)	1563.0
	a_1	1564.3(2)	1564.0
(BDI)AlI_2	a_1	1562.5(2)	1562.3, 1563.2
	b_1	1563.7(2)	1563.7
	b_2	1564.2(2)	1564.0
	a_1	1564.9(2)	1564.8
(BDI)$AlCl_2$	a_1	1563.7(2)	1563.5, 1564.0
	b_2	1564.2(2)	1564.9
	b_1	1565.0(2)	1565.0
	a_1	1565.9(2)	1566.0
(BDI)AlF_2	a_1	1564.1(2)	1564.0
	b_1	1565.6(3)	1565.4
	b_2	1565.6(3)	1565.6
	a_1	1566.3(2)	1566.7

[a] Experimental values were determined from the curve fitting analysis (see Figure 1.6)
[b] Calculated values were based on the energy the XCH calculated transition with the greatest oscillator strength for a given feature.
[c] This transition was not resolved in the experimental spectrum.
[d] Because orbital mixing in $(BDI)AlH_2$ resulted in a large number of bound-state Al 1s → a_1* transitions, this given value is estimated.

Pre-edge Spectral Assignments. To guide spectral interpretations, the Al K-edge XAS of (BDI)Al, $(BDI)AlR_2$ and $(BDI)AlX_2$ were calculated using an eXcited electron and Core-Hole (XCH) density functional theory approach. This approach has been successfully applied to other XAS simulations for s- and p-block inorganic complexes and organic ligands.[88-91] Simulations performed on entire unit cells and on individual molecules showed excellent agreement in the pre-edge region; the spectra for individual molecules were deconvoluted into their directional components and are presented in Figure 1.5. In order to facilitate comparison to experiment, each calculated spectrum has been shifted rigidly along the energy axis by matching the energies of the most intense features in the calculated and experimental spectra (see Experimental Details). The total calculated spectrum and directionally-dependent components showed good qualitative agreement with the experimental data and results from the curve fitting analyses, respectively. To facilitate assigning spectral features to excited states associated with specific orbitals, these calculations were also used to generate isosurface plots of the final state electronic orbitals that corresponded to each transition. Figure 1.6 provides plots of the final state orbital isosurfaces that corresponded to the most significant transitions in the (BDI)Al, $(BDI)AlR_2$ and $(BDI)AlX_2$ spectra.

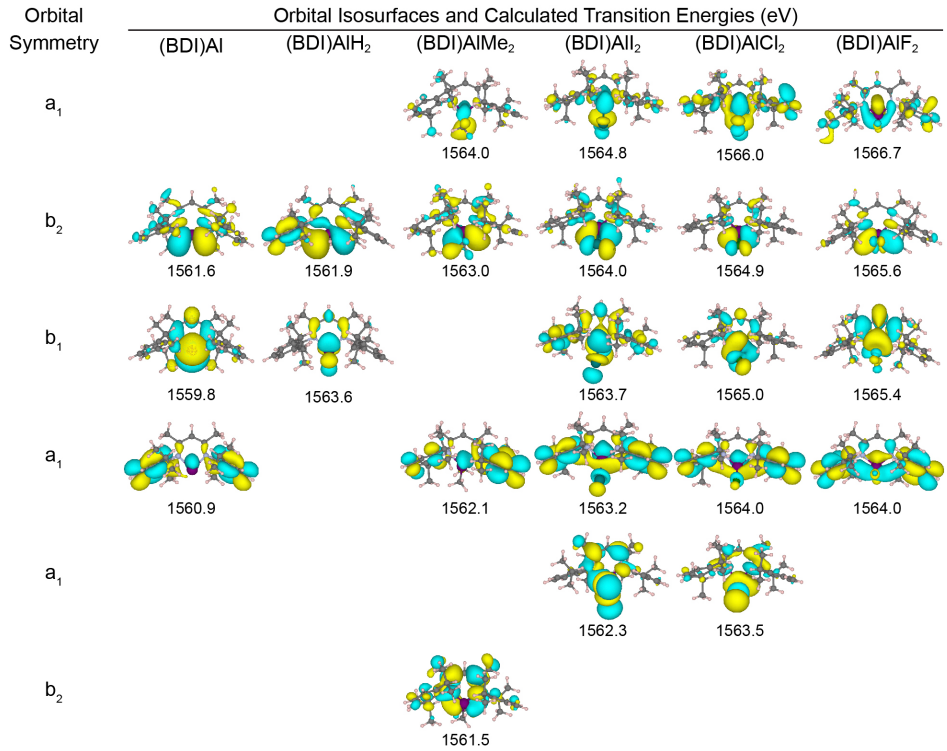

Figure 1.6. Isosurfaces of the excited states corresponding to the transitions with the greatest oscillator strength for a given feature calculated using the XCH approach.

(BDI)Al and (BDI)AlR$_2$ complexes: For (BDI)Al, two distinct features were observed in the experimental spectrum at 1559.8(2) and 1561.7(2) eV whose intensities decreased significantly when the polarization vector was rotated to 90° (Figure 1.7). Comparison with the XCH calculations suggested that these features corresponded to transitions into the b_1* and b_2* orbitals, respectively. The Al 1s → b_1* transition for (BDI)Al is significantly lower in energy than the lowest energy feature that was previously reported at 1561.2 eV for $[(C_5Me_5)Al]_4$ (Al 1s → t_2*),[92] which may reflect the differences in ligand, geometry, or the presence of Al–Al bonds, and justifies differences in the determined Lewis basicty of these compounds.[42,93] The calculations also indicated that a weak transition into the a_1* orbital occurred at 1560.9 eV. However, because Al 1s → Al 3s transitions are dipole forbidden, the a_1* transition intensity resulting primarily from hybridization effects was predicted to be low and was not resolved in the experimental spectrum.

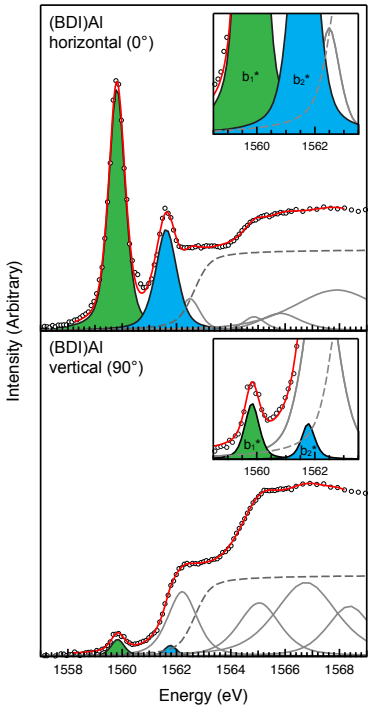

Figure 1.7. Al K-edge XAS spectra (STXM) experimental data for (BDI)Al at perpendicular light polarization settings (black circles). Pseudo-Voigt functions used to model pre-edge features (solid blue, and green traces), step-function used to model the edge (dashed grey trace), and pseudo-Voigt functions used to model post-edge features (solid grey traces) summed to generate the curve-fits (red traces). The inset shows the pre-edge features over a smaller energy range with the final state orbital labels corresponding to the transition assigned to each feature. Similar procedures were employed to determine the transitions energies for the other compounds.

In contrast to (BDI)Al, which exhibited multiple sharp pre-edge features, fewer features stood out in the Al K-edge spectrum of (BDI)AlH$_2$. One broad and asymmetric feature was observed near 1562 eV, and after rotating the polarization vector another feature was resolved at higher energy near 1564 eV. The asymmetric feature near 1562 eV was modeled with two

functions at 1561.9(2) eV and 1562.8(2) eV, while the higher energy feature was modeled with one function centered at 1564.5(2) eV. As described for (BDI)Al, the calculations ascribed the low energy feature centered near 1561.9(2) eV and the high energy feature at 1564.5(2) eV to transitions from the Al 1s core-level to orbitals with b_2* and b_1* character, respectively. In addition, the function at 1562.8(2) eV was assigned to a transition into an orbital with a_1* character.

The experimental (BDI)$AlMe_2$ spectra contained several features that were modeled with three well-resolved functions at 1560.8(2) eV, 1562.4(2) eV, and 1563.0(2) eV and one broad function at higher energy near 1564.3(2) eV. The polarization study and XCH calculations revealed that the transitions corresponding to the functions at 1560.8(2) eV and 1563.0(2) eV were polarized perpendicularly to the transitions corresponding to the functions at 1562.4(2) and 1564.3(2) eV (see Table 1.2 for XCH values). Examination of the calculated isosurfaces for each of the final state orbitals corresponding to the functions at 1560.8(2) and 1563.0(2) eV indicated that both were best described as having b_2* character (*y*-polarized). This splitting was not predicted from the simple group theory model for (BDI)AlR_2 derived in C_{2v}-symmetry, and the calculations indicated that it was caused by breaking of symmetry in the *x*-direction as the $AlMe_2$ fragment sat above the plane of the BDI ligand. This facilitated a non-negligible σ-type interaction with the BDI ligand that was not observed for (BDI)Al or (BDI)AlH_2. The slight underestimation of the splitting between the two b_2* features is attributed to the use of the semi-local GGA functional within the XCH approach. At higher energy, the functions at 1562.4(2) eV and 1564.3(2) eV were ascribed to two orbitals having a_1* character (*z*-polarized), resulting from mixing between Al 3s and 3p orbitals and the BDI backbone. The simulated spectra also showed two Al 1s → a_1* transitions: one weaker transition centered at 1562.1 eV and another with greater intensity at 1564.0 eV. Al 1s → 3s transitions are dipole forbidden, and the isosurfaces in Figure 1.6 suggested that this difference in relative intensity reflected a smaller amount of Al 3p character in the lower energy a_1* orbital. Finally, the calculations indicated that transitions to the b_1* orbital (*x*-polarized) were not resolved as distinct peaks in the experimental spectra, as a possible consequence of the strongly destabilizing interaction between the Al p_x orbitals and Me ligands.

(BDI)AlX_2 complexes: At first glance, the experimental Al K-edge XAS spectra for the (BDI)AlX_2 complexes resembled the spectra observed for (BDI)$AlMe_2$, in that they contained one intense, asymmetric feature at higher energy and one weaker feature at low energy (resolved as a shoulder in the (BDI)$AlCl_2$ spectrum). The spectrum for (BDI)AlF_2, was modeled with three functions, and changing polarizations indicated that the function at 1565.6(3) eV was polarized perpendicularly to two functions at 1564.1(2) and 1566.3(2) eV. As described for the (BDI)$AlMe_2$ complex, the XCH calculations ascribed the well resolved function at 1564.1(2) and the broader function at 1566.3(2) eV to transitions into orbitals with a_1* character resulting from mixing between Al 3s and 3p orbitals and the BDI and F ligands (*z*-polarized). Relative to (BDI)Al and the (BDI)AlR_2 compounds, the simulated spectra and calculated isosurfaces suggested that both Al 1s to a_1* transitions were allowed for (BDI)AlF_2 due to enhanced Al 3s and 3p hybridization. The calculations also suggested that the main feature was comprised of two closely-spaced transitions with maxima at 1565.4 and 1565.6 eV, respectively. The calculated isosurfaces indicated that the transition at 1565.4 eV corresponded to a b_1*-type orbital that was Al–F σ-antibonding, while the slightly higher energy transition at 1565.6 eV was assigned to a transition into a b_2*-type orbital that was Al–F π-antibonding. These transitions could not be separately resolved in the experimental spectra, and incorporating additional pseudo-Voigt

functions into the curve fitting models resulted in energies with large errors.

No significant polarization dependence was observed in the experimental spectra of the remaining halides because the individual molecules of $(BDI)AlI_2$ and $(BDI)AlCl_2$ are not oriented along crystallographic axes within the unit cell. However, each of the XCH calculations supported an interpretation that was analogous to that described for the Al K-edge XAS of $(BDI)AlF_2$. For example, the lowest energy functions at 1563.7(2) eV for $(BDI)AlCl_2$ (shoulder) and 1562.5(2) eV for $(BDI)AlI_2$ were ascribed to transitions into a_1*-type orbitals derived from hybridization between the Al 1s and Al $3p_z$. Moving to higher energy, two closely-spaced transitions into orbitals of b_1* and b_2* symmetry were predicted and assigned to the functions at 1563.7(2) and 1564.2(2) eV for $(BDI)AlI_2$ and 1565.0(2) and 1564.2(2) eV for $(BDI)AlCl_2$, respectively.

Discussion. Spectral features at the K-edge for first-row transition metals often follow Kunzl's law, in which 1s → 4p transition energies increase with decreases in the 3d-orbital occupation of the absorbing metal atom.[63] In principle, relative changes in the 1s → 3p transition energies recorded at the Al K-edge can also be used to evaluate differences in valence orbital occupation for the (BDI)Al, $(BDI)AlR_2$, and $(BDI)AlX_2$ complexes. However, because the Al 3p-orbitals participate in bonding directly, significant differences in the relative order and composition of the unoccupied molecular orbitals are observed with different geometries and ligand environments. Hence, it is necessary to compare the energy of "isolobal" transitions to final state orbitals that have similar orbital compositions and symmetries within a molecular orbital framework. In notation adopted for the simplified C_{2v} symmetric representation, transitions to the Al p_y orbitals that have b_2* symmetry meet this criterion and were observed for all six analytes. Because these orbitals are orthogonal to the Al–R and Al–X bonds and are strictly non-bonding with respect to the R^{1-} ligands, they are more likely to reflect changes in Al electron density or bonding with the BDI supporting ligands.

For $(BDI)AlX_2$ complexes, Al 1s → b_2* transitions were observed in the experimental Al K-edge XAS spectra at increasing energies such that $(BDI)AlF_2$ > $(BDI)AlCl_2$ ≈ $(BDI)AlI_2$ (1565.6(3), 1564.2(2), and 1564.2(2) eV for X = F, Cl, and I, respectively). The XCH calculations supported this trend, predicting Al 1s → b_2* transitions centered at 1565.6, 1564.9, and 1564.0 eV for X = F, Cl, and I, respectively. Halide ligand π-donation was expected to destabilize the b_2* orbital and increase the energy of the corresponding Al 1s → b_2* transition. However, examination of the isosurfaces provided in Figure 1.6 showed that the b_2* orbitals had more halide character for $(BDI)AlCl_2$ and $(BDI)AlI_2$, and approach Al–F nonbonding for $(BDI)AlF_2$. Hence, the data suggested that the increase in energy of the Al 1s → b_2* transitions for $(BDI)AlF_2$ correlated with increasing electronegativities of the halide ligands. Along these lines, the Al 1s → b_2* transition for $(BDI)AlMe_2$ decreased further to 1563.0(2) eV, which was in agreement with the group electronegativity of 2.3 ascribed to Me^{1-} ligands.[94]

Figure 1.8 plots values for the experimental Al K-edge transitions associated with final state orbitals of a_1, b_1, or b_2 parentage in C_{2v} symmetry relative to Pauling electronegativities (4.0, 3.0, and 2.5 for F, Cl, and I, respectively).[62] Each of the transitions to a_1* (Al–L σ), b_1* (Al–L σ) or b_2* (Al–X π, Al–R nb) final state orbitals showed a trend towards higher energies when analytes with more electronegative ligands were examined. Hence, the effects of metal–ligand bonding could be accounted for by comparing "isolobal" final states within a molecular orbital framework, which showed that core Al 1s orbital stabilization due to changes in metal electron density plays a significant role in the Al K-edge XAS. This phenomenon had been observed frequently in metal K-edge XAS spectra for d-block transition metals. The shifts in

energy had been attributed to metal valence electrons becoming attracted to more electronegative ligands, effectively decreasing the electron density on the metal center and stabilizing the remaining core and valence electrons.[26,63] The generality of this trend for each of the (BDI)Al, (BDI)AlX$_2$, and (BDI)AlR$_2$ compounds and for all of the final state orbital symmetries indicated that the Al K-edge XAS transition energies were also driven by changes in electron density at aluminum. In some cases, the range in transition energies were substantial. For example, the Al 1s → b$_2$* transition energy for (BDI)AlF$_2$ compound was 2.6(3) eV higher in energy than the corresponding transition for (BDI)AlMe$_2$, suggesting that significant differences in electron density around the aluminum occurred.

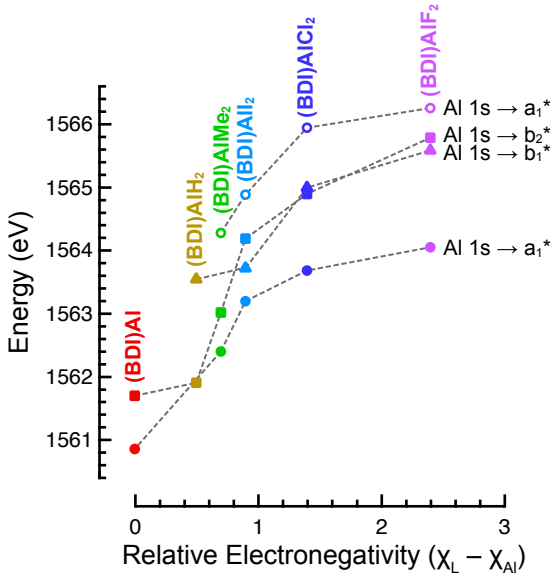

Figure 1.8. Comparison of the experimental Al K-edge XAS transition energies (eV) from Table 1.2 and the relative aluminum and ligand electronegativities ($\chi_L - \chi_{Al}$). Calculated transition energies were used in instances when the transitions were poorly resolved in the experimental spectra (see Table 1.2).

For (BDI)Al, an Al 1s → b$_2$* transition was observed in the Al K-edge XAS spectrum at 1561.7(2) eV. Despite having different spectral profiles, the curve-fitting analysis suggested that the energy of the Al 1s → b$_2$* transition was within error of the Al 1s → b$_2$* transition observed at 1561.9(2) eV for (BDI)AlH$_2$. In addition, the XCH calculations predicted very similar Al 1s → b$_2$* transition energies of 1561.6 and 1561.9 eV for (BDI)Al and (BDI)AlH$_2$, respectively. Compared with the higher energy Al 1s → b$_2$* transitions observed for (BDI)AlMe$_2$ and the (BDI)AlX$_2$ compounds, the close correspondence between these transitions suggested that the nominal charge at Al and bonding with the BDI supporting ligands was similar for (BDI)Al and (BDI)AlH$_2$, despite having very different formal charges of +1 and +3, respectively. To further explore this surprising result, the Al 1s core-level binding energies as well as the unoccupied Al projected density-of-states were analyzed in both complexes. The Al 1s → b$_2$* X-ray transition energy can be decomposed into a non-interacting term equal to the difference in the 1s and b$_2$* single-particle energy levels and an exciton binding energy. Differences in the Al 1s core-level binding energies are expected to reflect changes in the local electron density environment around the Al atom while differences in the energy position of the b$_2$* orbital in the unoccupied manifold should indicate changes in Al bonding to the ligands. The Al 1s core-level binding

energies in the two complexes were determined from pseudopotential DFT total energy differences. The Al 1s core-level binding energy in a molecular complex ε_{1s}^{mol} is given by:

$$\varepsilon_{1s}^{mol} = \{[E_{FCH,PP}^{mol} - E_{GS,PP}^{mol}] - [E_{FCH,PP}^{atom} - E_{GS,PP}^{atom}]\} + \Delta_{CL}$$

where $E_{FCH,PP}^{mol}$, $E_{GS,PP}^{mol}$, $E_{FCH,PP}^{atom}$, $E_{GS,PP}^{atom}$ represent pseudopotential based total energies of the Al 1s core-ionized molecular ion, the molecular ground-state, an isolated 1s core-ionized Al ion and an isolated Al atom in the ground-state respectively, while Δ_{CL} represents a fixed empirical energy calibration term consistent with the rigid shift Δ applied to the XAS spectrum of (BDI)Al. The abbreviations FCH, GS, PP and CL stand for full core-hole, ground-state, pseudopotential and core-level respectively. Similarly, the single-particle energy of the b_2* orbital $\varepsilon_{b_2^*}$ was approximated as

$$\varepsilon_{b_2^*} = -EA + (\epsilon_{b_2^*}^{KS} - \epsilon_{LUMO}^{KS})$$

where EA is the electron affinity determined in a ΔSCF calculation, and $\epsilon_{b_2^*}^{KS}$, ϵ_{LUMO}^{KS} are the ground-state Kohn-Sham eigenvalues of the b_2* and LUMO orbitals respectively. The calculated Al 1s and b_2* single-particle energies are shown in Table 1.3 and the unoccupied ground-state DOS as well as the ground-state isosurfaces for the lowest b_2* state are presented in Figure 1.9.

Table 1.3. Single-particle energies of the Al 1s core levels (ε_{1s}^{mol}) and unoccupied b_2* orbitals.

	ε_{1s}^{mol} (eV)	$\varepsilon_{b_2^*}$(eV)
(BDI)Al	-1564.26	1.960
(BDI)AlH_2	-1564.30	1.994

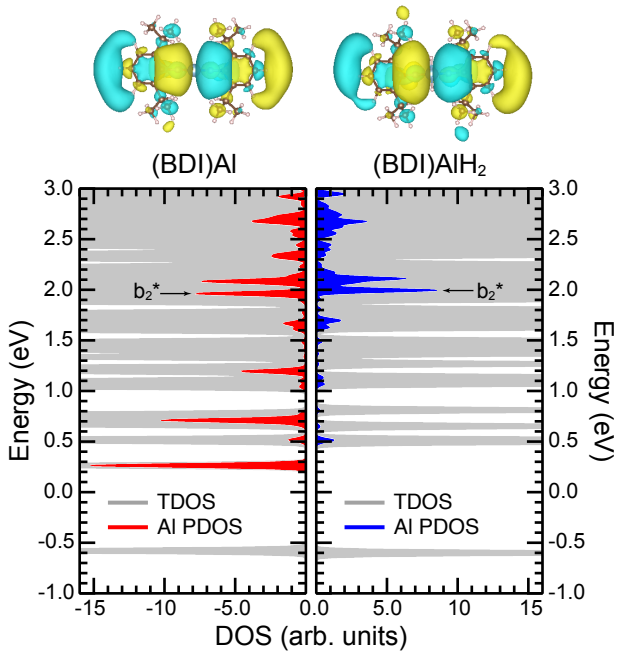

Figure 1.9. Total (gray) and Al projected (red, blue) unoccupied density-of-states and ground-state orbital isosurfaces for the lowest single particle b_2* state for (BDI)Al and (BDI)AlH_2 complexes.

Remarkably, both the Al 1s core-level and unoccupied b_2* single-particle energies in (BDI)Al and (BDI)AlH_2 were found to be very similar, differing by no more than 40 meV, in spite of the very different formal charges on Al. Test calculations employing hybrid-DFT functionals (not shown) confirmed the robustness of this result with respect to DFT functional. The calculations therefore supported the experimental results and the interpretation that the ligand field environment induced similar charges for the aluminum atoms in both (BDI)Al and (BDI)AlH_2. This finding was consistent with the generally accepted model that main group elements form covalently bonded hydrides, relative to transition metal hydrides that can have either more hydridic or more protic character.[95] Additional spectroscopic and theoretical experiments that directly probe the core-state binding energies in (BDI)Al, (BDI)AlX_2, (BDI)AlR_2 and other aluminum coordination compounds are needed to test the limits of this interpretation.

Conclusions

The application of X-ray spectroscopies to probe electronic structure in main-group coordination compounds represents a long-standing experimental challenge. The results presented in this study showed that polarized Al K-edge XAS spectroscopy combined with theory could be used to identify experimental trends that support a detailed picture of σ- and π-bonding interactions between the aluminum metal and associated ligands. Pre-edge features associated with transitions involving the three Al 3p orbitals were observed in the polarized Al K-edge XAS spectra of (BDI)Al, (BDI)AlX_2, and (BDI)AlR_2 (X = F, Cl, I; R = H, Me), and were assigned with the aid of XCH calculations. Metal–ligand bonding played a significant role in establishing the relative energies and ordering of molecular orbitals probed by the 1s → 3p transitions; significant differences were observed depending on the σ- and π-bonding abilities of the X^{1-} and R^{1-} ligands.

By comparing transitions into excited states with similar orbital compositions and symmetries within a molecular orbital framework, it was possible to identify differences in core orbital energies and valence orbital occupation across the series of (BDI)Al, (BDI)AlR_2 and (BDI)AlX_2 complexes while accounting for changes in the ligand environment. The observed transition energies primarily reflected a change in the electron density on aluminum in the presence of ligands with different electronegativities. This analysis indicated that the charge distribution on aluminum in (BDI)Al was nearly identical to the charge distribution on (BDI)AlH_2, despite having very different valence orbital occupations and formal oxidation states of +1 and +3, respectively. However, (BDI)Al also exhibited a low-energy feature that was attributed to a transition into an unoccupied b_1* orbital, which was best described as a vacant, low energy Al 3p-orbital that is orthogonal to the (BDI)Al plane. This has important implications for the novel reactivity of (BDI)Al, and is a distinguishing aspect of the electronic structure of (BDI)Al relative to (BDI)AlX_2 and (BDI)AlR_2. The combination of theory and XAS in this instance provided insight regarding the nature of Al σ- and π-bonding in specific molecular orbitals that could not be obtained from ^{27}Al NMR spectroscopy or analysis of metrical parameters obtained by single-crystal X-ray diffraction. However, Al K-edge XAS could become a powerful complement to ^{27}Al NMR, which is also sensitive to a range of factors including formal charge and the nature of bonding ligands, their geometry and coordination number.[21-23,96,97] Studies on a wider range of aluminum molecules and extended solids are needed to explore possible correlations between observables provided by the two techniques.

Whereas first-row transition metals can adopt a range of oxidation states under normal conditions, the $Al^{3+} + 2e^- \rightarrow Al^{1+}$ reduction generally requires strong chemical reducing agents.

These studies supported the recently observed reversible hydride transfer reactivity between the (BDI)Al and (BDI)AlH_2 complexes, and justified the accessibility of 2-electron reductive elimination pathways at aluminum centers.[48,49] This work may impact efforts to destabilize or regenerate aluminum hydrides, which are utilized as reducing agents and hydride sources during organic transformations,[98] and as media for hydrogen storage.[99-102] Additional studies to assess the utility of Al K-edge XAS in other hydride systems are underway.

Experimental Details

General Synthetic Details. All reactions were performed either using standard Schlenk line techniques or in a MBraun inert atmosphere glovebox under a purified nitrogen atmosphere (<0.1 ppm O_2/H_2O). Hexanes, toluene, diethyl ether (Et_2O), and tetrahydrofuran (THF) were dried and degassed using a commercially available Phoenix Solvent Drying System from JC Meyer Solvent Systems. C_6D_6 and $CDCl_3$ were dried over sodium/benzophenone and CaH_2 respectively, and vacuum transferred to a storage flask before being stored in a drybox. Solution NMR spectra were collected on either Bruker AVB-400, AVQ-400, or DRX-500 spectrometers at ambient temperature. ^{1}H-NMR chemical shifts (δ in ppm) were calibrated to residual solvent peaks. All reagents were acquired from commercial sources and used without further purification, with the exception of iodine and aluminum trichloride which were purified by sublimation, and $LiAlH_4$ which was purified by extraction with dry Et_2O. (BDI)H,[103] (BDI)Li•Et_2O,[104] (BDI)$AlMe_2$,[73] (BDI)AlI_2,[13] (BDI)Al,[13] (BDI)AlF_2,[75] and (BDI)$AlCl_2$[74] were synthesized according to literature procedures and characterized using single-crystal X-ray diffraction and/or ^{1}H and ^{27}Al NMR prior to use. The crystal structure of (BDI)AlI_2 was determined to allow for comparison of its metrical parameters with the (BDI)AlX_2 analogues. ^{27}Al NMR has been used previously to compare changes in Al coordination number, oxidation state, and to determine thermodynamic parameters.[21,105] Chemical shifts for the formally Al(III) species were consistent with previous results and generally fell within the known range of 180 to 80 ppm for four-coordinate aluminum complexes (Table 1.4).[21,105,106]

Table 1.1. ^{27}Al NMR chemical shifts (δ) determined for each of the synthesized compounds.

Compound	^{27}Al NMR shift (ppm)
(BDI)Al	*a*
(BDI)$AlMe_2$	160.0
(BDI)AlH_2	130.2
(BDI)$AlCl_2$	100.7
(BDI)AlI_2	84.0
(BDI)AlF_2	67*b*

[a]No ^{27}Al resonance was observed.[13] [b]Resonance was coincident with a large background resonance from the instrument.

Synthesis of (BDI)AlH_2. A modified version of a published procedure was used.[107] A mixture of $LiAlH_4$ (0.448 g, 11.8 mmol) and (BDI)H (4.20 g, 10.0 mmol) was suspended in toluene (80 ml). The mixture was heated at 90 °C for five days. The solution was then filtered, concentrated to approximately 20 mL by removal of solvent *in vacuo*, and cooled to -30 °C resulting in formation of a colorless crystalline solid (1.44 g, 32 % yield). ^{1}H NMR data matched reported

values.[108]

Sample Preparation and Orientation. Sample preparation and methodology for handling air-sensitive analytes was similar to that described previously.[109-112] Samples were prepared in an argon-filled glovebox by grinding crystals of the analyte into a fine powder with a mortar and pestle, and brushing the powder onto a Si_3N_4 membrane (100 nm, Silson) with a fiber. This method arranged a large number of micron-scale crystals in a relatively compact area that are suitable for Al K-edge measurements. A second membrane was placed over the sample, and the edges were sealed together using Hardman Double/Bubble® 5 minute epoxy.

Beamline Characteristics. STXM methodology was similar to that discussed previously.[109-112] Single-energy images and Al K-edge XAS spectra were acquired using the STXM instrument at the Environmental Science (MES) beamline 11.0.2 at the Advanced Light Source (ALS), which was operated in topoff mode at 500 mA, in a ~0.5 atm He-filled chamber.[113] The beamline used photons from an elliptically polarizing undulator that delivered photons in the 100 to 2000 eV energy range to a variable-angle included plane-grating monochromator. For Al K-edge measurements, the photon energy of the high energy diffraction grating was calibrated to the Al K-edge for a 1000 Å aluminum filter sample (Luxel, inflection point = 1559.0 eV). The maximum energy resolution $E/\Delta E$ was previously determined at better than 7500,[78] which was consistent with the observed standard deviation for spectral transitions of ± 0.3 eV determined from comparison of spectral features over multiple particles and beam runs. For these measurements, the X-ray beam was focused with a zone plate onto the sample, and the transmitted light was detected. The spot size and spectral resolution were determined from characteristics of the 25 nm zone plate. Images at a single energy were obtained by raster-scanning the sample and collecting transmitted monochromatic light as a function of sample position. Spectra at particular regions of interest on the sample image were extracted from the "stack", a collection of images recorded at multiple, closely spaced photon energies across the absorption edge.[114] Dwell times used to acquire an image at a single photon energy were 1 or 2 ms per pixel. To quantify the absorbance signal, the measured transmitted intensity (I) was converted to optical density using Beer−Lambert's law: $OD = \ln(I/I_0) = \mu\rho d$, where I_0 is the incident photon flux intensity, d is the sample thickness, and μ and ρ are the mass absorption coefficient and density of the sample material, respectively. Incident beam intensity was measured through the sample-free region of the Si_3N_4 windows. Regions of particles with an absorption of >1.5 OD were omitted to ensure the spectra were in the linear regime of the Beer−Lambert law.

Polarized Al K-edge XAS Studies. Initial imaging surveys of the samples revealed a large number of crystalline particles that had adopted random orientations on the Si_3N_4 membranes during sample preparation. To determine the nature of any polarization dependence, the EPU was adjusted to horizontal and spectra were recorded on different crystalline particles until spectra were observed that had maximized or minimized transition intensities. The polarization vector was then rotated by 90° by setting the EPU to vertical, and the Al K-edge XAS measurement was repeated (see Figure 1.10). Additional spectra were also recorded at intermediate beam polarizations in steps of 10 to 15° between the limits of 0 and 90°. Relative changes in transition intensities observed in the directionally-dependent spectra were compared for measurements on the same particle, which greatly aided spectral assignments. During the STXM experiment, single-energy images showed no signs of radiation damage to the particles, and the polarization-dependence of the spectra was reproduced from multiple independent crystallites and beam-runs.

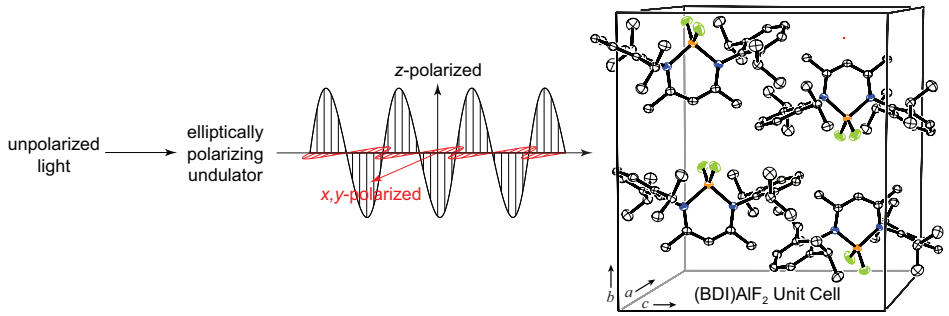

Figure 1.10. Projection of the crystal structure of (BDI)AlF_2 onto the *bc* plane with respect to polarized synchrotron radiation. Thermal ellipsoids are shown with 50% probability, with atoms colored as white (carbon), blue (nitrogen), orange (aluminum), and green (fluorine). Hydrogen atoms have been omitted for clarity. Adapted with permission from S. Singh, H. –J. Ahn, A. Stasch, V. Jancik, H. W. Roesky, A. Pal, M. Biadene, R. Herbst-Irmer, M. Noltemeyer, and H. –G. Schmidt, *Inorganic Chemistry*, 2006, **45**, 1853-1860. Copyright 2006 American Chemical Society.

Data Analysis. The data were background subtracted using the *MBACK* algorithm in *MATLAB*.[115] Fits for the Al K-edge data were generated using the program IGOR 6.0 and a modified version of EDG_FIT.[116] Spectra were modeled using pseudo-Voigt line shapes consisting of an equal mixture of Gaussian and Lorentzian character as well as a step function with a 1:1 ratio of arctangent and error function contributions.[87] In each case, these analyses provided high quality fits of the experimental data as reflected by low correlation coefficients, residual data that deviated slightly from zero and symmetric residual peaks that matched well with the parent pseudo-Voigt functions. Uncertainty in the transition energies was estimated at ± 0.3 eV based on the resolving power of instrument and on the variation in energy of functions comprising the curve fits.

Electronic Structure Calculations. Geometries of all the Al complexes considered were optimized within density functional theory (DFT)[117,118] simulations based on a projector augmented wave (PAW)[119] pseudopotential and plane-wave basis set framework as implemented in the VASP package.[120] The exchange-correlation energy was treated at the level of the Perdew-Burke-Ernzerhof (PBE)[121] generalized gradient approximation (GGA). Dispersion forces were taken into account using the DFT-D2 approach.[122] In conjunction with a plane-wave energy cut-off of 350 eV, pseudopotentials with the following valence electronic configurations were employed: Al($3s^2 3p^1$), C($2s^2 2p^2$), N($2s^2 2p^3$), H($1s^1$), F($2s^2 2p^5$), Cl($3s^2 3p^5$), I($5s^2 5p^5$). The Brillouin zone was sampled at the Γ point. Geometries were optimized until all forces were smaller than 0.02 eV/Å. Structures so obtained were used in subsequent X-ray absorption spectroscopy simulations.

Al K-edge Spectral Simulations. XAS at the Al K-edge were calculated using the XCH approach.[80] The XCH approach has been described previously in detail.[80,123,124] In this method, the lowest energy X-ray excited state of the system was modeled within an occupation-constrained DFT framework wherein the core-excited atom was described through a core-hole pseudopotential and the screening due to the excited electron was taken into account self-consistently. Higher lying X-ray excited state energies were approximated through eigenvalue differences obtained from the Kohn-Sham (KS) spectrum of the lowest energy core-excited state. X-ray transition matrix elements were calculated using Fermi's golden rule and typically for light-element K-edges, within a dipole approximation. The XCH method was utilized as

implemented in a development version of the Quantum-Espresso package[125] which provided a plane-wave pseudopotential DFT framework for electronic structure calculations. Ultra-soft pseudopotentials[126] with the same valence electronic configuration as described above were used together with a plane-wave energy cut-off of 25 Ry. To describe 1s core-excited Al in XAS simulations, a core-hole pseudopotential with the electronic configuration $1s^1 2s^2 2p^6 3s^2 3p^2$ was generated. The Brillouin zone was sampled at the zone-center during the self-consistent field calculation but the band structure was interpolated over a uniform Γ-centered 5 x 5 x 5 k-point grid using the Shirley interpolation scheme[127] in order to generate spectra.

XAS spectra were obtained both for the molecular crystal unit-cells containing multiple Al complexes as well as for individual molecular units extracted from the optimized crystal geometries. The spectra of molecular crystals differed insignificantly from that of isolated molecular units in the near edge region of interest. Therefore, spectra obtained from molecular unit simulations were used in the subsequent analysis as they facilitate a convenient decomposition of the spectrum into contributions from different polarization directions.

Within the XCH approach, the relative energy alignment of XAS spectra corresponding to core-excitations on atoms in different chemical environments was carried out through total energy differences.[123] However, since the method was based on core-hole pseudopotentials and did not explicitly include the energy of core electrons, calibration of the absolute energy position of the calculated spectra with respect to experiment involved a rigid energy shift Δ, which depended on the core-excitation edge being considered.[123] For a wide range of light-element K-edges, the shift Δ may be calculated once for a given excitation-edge based on a reference chemical system and the same shift can be applied to all XCH spectra calculated at that excitation-edge in different chemical environments.[91,123,124] At the Al K-edge for the complexes in this study, the (BDI)Al complex was used as the reference system and determined a value of Δ = 1560.27 eV. However, such an alignment scheme led to a systematic red-shift of +0.9 to 1.8 eV in the calculated spectra of all other complexes with respect to experiment, although the spectral line shapes were well reproduced. The discrepancy was traced to a lack of error-cancellation in the KS orbital eigenvalues of the lowest unoccupied molecular orbital (LUMO) and higher lying virtual orbitals in the (BDI)AlR_2 and (BDI)AlX_2 systems. KS eigenvalues calculated at the level of semi-local GGA functionals often suffer from significant self-interaction (SI) errors but can nevertheless yield good spectra provided that the relative SI errors cancel.[128] In the present case, the lowest energy XCH reference configuration was based on an Al 1s → BDI π* excitation that had no Al 3p character, and the eigenvalue difference of the LUMO π* state with respect to higher lying states having significant Al 3p character was underestimated by +0.9 to 1.8 eV. Therefore, this led to a systematic underestimation of the energy positions of various Al 3p derived spectral features that lie higher in energy, and it was necessary to align the spectra individually. The energies of the transitions with the greatest oscillator strength in the calculated spectra were set to be equal to the energies of most intense functions used in the curve-fitting analysis of the experimental spectra, which provided energy shifts of +1561.34, +1561.51, +1561.16, +1561.78, +1562.07 for the (BDI)AlH_2, (BDI)$AlMe_2$, (BDI)AlI_2, (BDI)$AlCl_2$, and (BDI)AlF_2, respectively.

XCH final state electronic wavefunctions corresponding to core-excitations into the virtual orbital manifold were approximated by unoccupied KS wavefunctions obtained from the self-consistent occupation-constrained DFT calculation including the core-hole. Orbital isosurfaces were visualized using VESTA-3.[129]

References

1 *U.S. Energy Requirements for Aluminum Production: Historical Perspective, Theoretical Limits, and Current Practices*, U.S. Department of Energy, 2007.
2 R. Jullien and B. Coqblin, *Phys. Lett-Paris*, 1974, **35**, 197–201.
3 L. R. Meza, S. Das and J. R. Greer, *Science*, 2014, **345**, 1322–1326.
4 S.-H. Kim, H. Kim and N. J. Kim, *Nature*, 2015, **518**, 77–79.
5 Y. Taniyasu, M. Kasu and T. Makimoto, *Nature*, 2006, **441**, 325–328.
6 E. Y. X. Chen and T. J. Marks, *Chem. Rev.*, 2000, **100**, 1391–1434.
7 E. Zurek and T. Ziegler, *Prog. Polym. Sci.*, 2004, **29**, 107–148.
8 G. Ménard and D. W. Stephan, *J. Am. Chem. Soc.*, 2010, **132**, 1796–1797.
9 G. Ménard and D. W. Stephan, *Angew. Chem. Int. Ed.*, 2011, **50**, 8396–8399.
10 C. Dohmeier, D. Loos and H. Schnöckel, *Angew. Chem. Int. Ed. Engl.*, 1996, **35**, 129–149.
11 A. Downs, *Coord. Chem. Rev.*, 1999, **189**, 59–100.
12 P. P. Power, *Chem. Rev.*, 1999, **99**, 3463–3504.
13 C. Cui, H. W. Roesky, H.-G. Schmidt, M. Noltemeyer, H. Hao and F. Cimpoesu, *Angew. Chem. Int. Ed.*, 2000, **39**, 4274–4276.
14 H. W. Roesky and S. S. Kumar, *Chem. Commun.*, 2005, **0**, 4027–4038.
15 S. Dagorne and D. A. Atwood, *Chem. Rev.*, 2008, **108**, 4037–4071.
16 S. Nagendran and H. W. Roesky, *Organometallics*, 2008, **27**, 457–492.
17 S. González-Gallardo, T. Bollermann, R. A. Fischer and R. Murugavel, *Chem. Rev.*, 2012, **112**, 3136–3170.
18 P. P. Power, A. Moezzi, D. C. Pestana and M. A. Petrie, *Pure & Appl. Chem.*, 1991, **63**, 859–866.
19 R. J. Wright, M. Brynda and P. P. Power, *Angew. Chem. Int. Ed.*, 2006, **45**, 5953–5956.
20 E. Rivard and P. P. Power, *Inorg. Chem.*, 2007, **46**, 10047–10064.
21 J. Gauss, U. Schneider and R. Ahlrichs, *J. Am. Chem. Soc.*, 1993, **115**, 2402–2408.
22 R. W. Schurko, I. Hung, C. L. B. Macdonald and A. H. Cowley, *J. Am. Chem. Soc.*, 2002, **124**, 13204–13214.
23 D. Bono, J. Hartig, M. Huber, H. Schnöckel and L. J. de Jongh, *J. Clust. Sci.*, 2007, **18**, 319–331.
24 A. H. Cowley, F. P. Gabbai, H. S. Isom and A. Decken, *J. Organomet. Chem.*, 1995, **500**, 81–88.
25 J. Weiss, D. Stetzkamp and B. Nuber, *Angew. Chem. Int. Ed. Engl.*, 1997, **35**, 70–72.
26 J. D. Gorden, A. Voigt, C. L. B. Macdonald, J. S. Silverman and A. H. Cowley, *J. Am. Chem. Soc.*, 2000, **122**, 950–951.
27 M. Huber, P. Henke and H. Schnöckel, *Chem. Eur. J.*, 2009, **15**, 12180–12183.
28 N. Dettenrieder, H. M. Dietrich, C. Schädle, C. Maichle-Mössmer, K. W. Törnroos and R. Anwander, *Angew. Chem. Int. Ed.*, 2012, **51**, 4461–4465.
29 R. Ahlrichs, H. Horn and M. Ehrig, *Chem. Phys. Lett.*, 1991, **183**, 227–233.
30 W. H. Fink, P. P. Power and T. L. Allen, *Inorg. Chem.*, 1997, **36**, 1431–1436.
31 B. L. Kormos and C. J. Cramer, *Inorg. Chem.*, 2003, **42**, 6691–6700.
32 I. McKenzie, P. W. Percival and J. A. C. Clyburne, *Chem. Commun.*, 2005, **0**, 1134–1136.
33 C. R. Landis and F. Weinhold, *J. Am. Chem. Soc.*, 2006, **128**, 7335–7345.
34 D. J. Grant and D. A. Dixon, *J. Phys. Chem. A*, 2006, **110**, 12955–12962.
35 C. A. Caputo and P. P. Power, *Organometallics*, 2013, **32**, 2278–2286.

36 A. Haaland, D. J. Shorokhov, H. V. Volden and K. W. Klinkhammer, *Inorg. Chem.*, 1999, **38**, 1118–1120.
37 C. Klemp, M. Bruns, J. Gauss, U. Häussermann, G. Stösser, L. van Wüllen, M. Jansen and H. Schnöckel, *J. Am. Chem. Soc.*, 2001, **123**, 9099–9106.
38 H.-J. Himmel and J. Vollet, *Organometallics*, 2002, **21**, 5972–5977.
39 A. Grubisic, X. Li, S. T. Stokes, J. Cordes, G. F. Ganteför, K. H. Bowen, B. Kiran, P. Jena, R. Burgert and H. Schnöckel, *J. Am. Chem. Soc.*, 2007, **129**, 5969–5975.
40 P. Henke, T. Pankewitz, W. Klopper, F. Breher and H. Schnöckel, *Angew. Chem. Int. Ed.*, 2009, **48**, 8141–8145.
41 X. Zhang, H. Wang, E. Collins, A. Lim, G. Ganteför, B. Kiran, H. Schnöckel, B. Eichhorn and K. Bowen, *J. Chem. Phys.*, 2013, **138**, 124303.
42 Z. Yang, X. Ma, R. B. Oswald, H. W. Roesky, H. Zhu, C. Schulzke, K. Starke, M. Baldus, H.-G. Schmidt and M. Noltemeyer, *Angew. Chem. Int. Ed.*, 2005, **44**, 7072–7074.
43 T. Nakamura, K. Suzuki and M. Yamashita, *J. Am. Chem. Soc.*, 2014, **136**, 9276–9279.
44 R. J. Wright, A. D. Phillips and P. P. Power, *J. Am. Chem. Soc.*, 2003, **125**, 10784–10785.
45 P. W. Roesky, *Dalton Trans.*, 2009, **0**, 1887–1893.
46 W. W. Schoeller, *Inorg. Chem.*, 2011, **50**, 2629–2633.
47 G. Tan, T. Szilvási, S. Inoue, B. Blom and M. Driess, *J. Am. Chem. Soc.*, 2014, **136**, 9732–9742.
48 T. Chu, I. Korobkov and G. I. Nikonov, *J. Am. Chem. Soc.*, 2014, **136**, 9195–9202.
49 C. Ganesamoorthy, S. Loerke, C. Gemel, P. Jerabek, M. Winter, G. Frenking and R. A. Fischer, *Chem. Commun.*, 2013, **49**, 2858–2860.
50 O. Ekkert, A. White, H. Toms and M. R. Crimmin, *Chemical Science*, 2015, **6**, 5617–5622.
51 T. W. Myers, N. Kazem, S. Stoll, R. D. Britt, M. Shanmugam and L. A. Berben, *J. Am. Chem. Soc.*, 2011, **133**, 8662–8672.
52 T. W. Myers, A. L. Holmes and L. A. Berben, *Inorg. Chem.*, 2012, **51**, 8997–9004.
53 T. W. Myers and L. A. Berben, *J. Am. Chem. Soc.*, 2013, **135**, 9988–9990.
54 T. W. Myers and L. A. Berben, *Chem. Commun.*, 2013, **49**, 4175–4177.
55 L. A. Berben, *Chem. Eur. J.*, 2015, **21**, 2734–2742.
56 L. A. Berben, B. de Bruin and A. F. Heyduk, *Chem. Commun.*, 2015, **51**, 1553–1554.
57 A. L. Roe, D. J. Schneider, R. J. Mayer, J. W. Pyrz, J. Widom and L. Que Jr., *J. Am. Chem. Soc.*, 1984, **106**, 1676–1681.
58 L. S. Kau and D. J. Spira-Solomon, *J. Am. Chem. Soc.*, 1987, **109**, 6433–6442.
59 J. L. DuBois, P. Mukherjee and A. M. Collier, *J. Am. Chem. Soc.*, 1997, **119**, 8578–8579.
60 T. E. Westre, P. Kennepohl and J. G. DeWitt, *J. Am. Chem. Soc.*, 1997, **119**, 6297–6314.
61 N. W. Aboelella, S. V. Kryatov, B. F. Gherman, W. W. Brennessel, V. G. Young, R. Sarangi, E. V. Rybak-Akimova, K. O. Hodgson, B. Hedman, E. I. Solomon, C. J. Cramer and W. B. Tolman, *J. Am. Chem. Soc.*, 2004, **126**, 16896–16911.
62 P. Chaurand, J. Rose, V. Briois, M. Salome, O. Proux, V. Nassif, L. Olivi, J. Susini, J.-L. Hazemann and J.-Y. Bottero, *J. Phys. Chem. B*, 2007, **111**, 5101–5110.
63 J. Wong, F. W. Lytle, R. P. Messmer and D. H. Maylotte, *Phys. Rev. B*, 1984, **30**, 5596–5610.
64 D. A. McKeown, *Phys. Chem. Miner.*, 1989, **16**, 678–683.
65 D. E. Li, G. M. Bancroft, M. E. Fleet, X. H. Feng and Y. M. Pan, *Am. Mineral.*, 1995, **80**, 432–440.

66 D. Cabaret, P. Sainctavit, P. Ildefonse and A. M. Flank, *J. Phys.: Condens. Matter*, 1996, **8**, 3691–3704.
67 P. Ildefonse, D. Cabaret, P. Sainctavit, G. Calas, A. M. Flank and P. Lagarde, *Phys Chem Minerals*, 1998, **25**, 112–121.
68 C. P. Balde and A. E. Mijovilovich, *J. Phys. Chem. C*, 2007, **111**, 11721–11725.
69 A. Léon, A. Balerna, G. Cinque, C. Frommen and M. Fichtner, *J. Phys. Chem. C*, 2007, **111**, 3795–3798.
70 L. R. Aramburo, Y. Liu, T. Tyliszczak, F. M. F. de Groot, J. C. Andrews and B. M. Weckhuysen, *ChemPhysChem*, 2013, **14**, 496–499.
71 H. E. van der Bij, D. Cicmil, J. Wang, F. Meirer, F. M. F. de Groot and B. M. Weckhuysen, *J. Am. Chem. Soc.*, 2014, **136**, 17774–17787.
72 J. A. Bearden and A. F. Burr, *Rev. Mod. Phys.*, 1967, **39**, 125–142.
73 B. Qian, D. L. Ward and M. R. Smith II, *Organometallics*, 1998, **17**, 3070–3076.
74 M. Stender, B. E. Eichler, N. J. Hardman, P. P. Power, J. Prust, M. Noltemeyer and H. W. Roesky, *Inorg. Chem.*, 2001, **40**, 2794–2799.
75 S. Singh, H.-J. Ahn, A. Stasch, V. Jancik, H. W. Roesky, A. Pal, M. Biadene, R. Herbst-Irmer, M. Noltemeyer and H.-G. Schmidt, *Inorg. Chem.*, 2006, **45**, 1853–1860.
76 W. Hunziker, M. R. Walters and A. W. Norman, *J. Biol. Chem.*, 1980, **255**, 9534–9537.
77 B. Kaulich, D. Bacescu, D. Cocco, J. Susini, M. Salome, O. Dhez, C. David, T. Weitkamp, E. Di Fabrizio, S. Cabrini, G. Morrison, P. Charalambous, J. Thieme, T. Wilhein, J. Kovac, M. Podnar and M. Kiskinova, *J. Phys. IV*, 2003, **104**, 103–107.
78 H. Bluhm, K. Andersson, T. Araki, K. Benzerara, G. E. Brown, J. J. Dynes, S. Ghosal, M. K. Gilles, H. C. Hansen, J. C. Hemminger, A. P. Hitchcock, G. Ketteler, A. L. D. Kilcoyne, E. Kneedler, J. R. Lawrence, G. G. Leppard, J. Majzlam, B. S. Mun, S. C. B. Myneni, A. Nilsson, H. Ogasawara, D. F. Ogletree, K. Pecher, M. Salmeron, D. K. Shuh, B. Tonner, T. Tyliszczak, T. Warwick and T. H. Yoon, *J. Electron Spectrosc. Relat. Phenom.*, 2006, **150**, 86–104.
79 K. V. Kaznatcheev, C. Karunakaran, U. D. Lanke, S. G. Urquhart, M. Obst and A. P. Hitchcock, *Nucl. Instrum. Methods Phys. Pres., Sect. A*, 2007, **582**, 96–99.
80 D. Prendergast and G. Galli, *Phys. Rev. Lett.*, 2006, **96**, 215502.
81 Y.-C. Tsai, *Coord. Chem. Rev.*, 2012, **256**, 722–758.
82 M. Rao, H. W. Roesky and G. Anantharaman, *J. Organomet. Chem.*, 2002, **646**, 4-14.
83 W. Uhl, *Naturwissenschaften*, 2004, **91**, 305–319.
84 C. Jones and A. Stasch, in *The Group 13 Metals Aluminium, Gallium, Indium and Thallium: Chemical Patterns and Peculiarities*, eds. S. Aldridge and A. J. Downs, John Wiley & Sons, Ltd, Chichester, UK, 2011, pp. 285–341.
85 N. J. Hardman, A. D. Phillips and P. P. Power, *Group 13 Chemistry—From Fundamentals to Application*, ACS Symp. Ser., 2002, vol. 822.
86 T. H. Yoon, S. B. Johnson, K. Benzerara, C. S. Doyle, T. Tyliszczak, D. K. Shuh and G. E. Brown, *Langmuir*, 2004, **20**, 10361–10366.
87 S. G. Minasian, J. L. Krinsky, V. A. Williams and J. Arnold, *J. Am. Chem. Soc.*, 2008, **130**, 10086–10087.
88 W. S. Drisdell, R. Poloni, T. M. McDonald, J. R. Long, B. Smit, J. B. Neaton, D. Prendergast and J. B. Kortright, *J. Am. Chem. Soc.*, 2013, **135**, 18183–18190.
89 I. Zegkinoglou, M.-E. Ragoussi, C. D. Pemmaraju, P. S. Johnson, D. F. Pickup, J. E. Ortega, D. Prendergast, G. de la Torre and F. J. Himpsel, *J. Phys. Chem. C*, 2013, **117**,

13357–13364.
90 T. A. Pascal, K. H. Wujcik, J. Velasco-Velez, C. Wu, A. A. Teran, M. Kapilashrami, J. Cabana, J. Guo, M. Salmeron, N. Balsara and D. Prendergast, *J. Phys. Chem. Lett.*, 2014, **5**, 1547–1551.
91 T. A. Pascal, U. Boesenberg, R. Kostecki, T. J. Richardson, T.-C. Weng, D. Sokaras, D. Nordlund, E. McDermott, A. Moewes, J. Cabana and D. Prendergast, *J. Chem. Phys.*, 2014, **140**, 034107.
92 S. G. Minasian, J. L. Krinsky, J. D. Rinehart, R. Copping, T. Tyliszczak, M. Janousch, D. K. Shuh and J. Arnold, *J. Am. Chem. Soc.*, 2009, **131**, 13767–13783.
93 C. L. B. Macdonald and A. H. Cowley, *J. Am. Chem. Soc.*, 1999, **121**, 12113–12126.
94 P. R. Wells, *Prog. Phys. Org. Chem*, 1968, **6**, 111–144.
95 F. A. Cotton and G. Wilkinson, *Advanced Inorganic Chemistry 5th Ed*, J. Wiley Sons. N. Y., 1988.
96 C. Dohmeier, M. Mocker, H. Schnöckel, A. Lotz, U. Schneider and R. Ahlrichs, *Angew. Chem. Int. Ed. Engl.*, 1993, **32**, 1428–1430.
97 P. Shapiro, *Coord. Chem. Rev.*, 1999, **189**, 1–17.
98 R. Noyori and T. Ohkuma, *Angew. Chem. Int. Ed.*, 2001, **40**, 40–73.
99 S.-I. Orimo, Y. Nakamori, J. R. Eliseo, A. Zuettel and C. M. Jensen, *Chem. Rev.*, 2007, **107**, 4111–4132.
100 B. Sakintuna, F. Lamari-Darkrim and M. Hirscher, *Int. J. Hydrogen Energy*, 2007, **32**, 1121–1140.
101 R. Zidan, B. L. Garcia-Diaz, C. S. Fewox, A. C. Stowe, J. R. Gray and A. G. Harter, *Chem. Commun.*, 2009, **0**, 3717–3719.
102 J. Graetz, J. J. Reilly, V. A. Yartys, J. P. Maehlen, B. M. Bulychev, V. E. Antonov, B. P. Tarasov and I. E. Gabis, *J. Alloys Compd.*, 2011, **509**, S517–S528.
103 J. Feldman, S. J. McLain and A. Parthasarathy, *Organometallics*, 1997, **16**, 1514–1516.
104 P. H. M. Budzelaar, A. B. van Oort and A. G. Orpen, *Eur. J. Inorg. Chem.*, 1998, 1485–1494.
105 C. T. Burns, P. J. Shapiro, P. H. M. Budzelaar, R. Willett and A. Vij, *Organometallics*, 2000, **19**, 3361–3367.
106 R. Benn and A. Rufinska, *Angew. Chem. Int. Ed. Engl.*, 1986, **25**, 861–881.
107 Y. Yang, H. Li, C. Wang and H. W. Roesky, *Inorg. Chem.*, 2012, **51**, 2204–2211.
108 C. Cui, H. W. Roesky, H. J. Hao, H. G. Schmidt and M. Noltemeyer, *Angew. Chem. Int. Ed.*, 2000, **39**, 1815–1817.
109 S. G. Minasian, J. M. Keith, E. R. Batista, K. S. Boland, J. A. Bradley, S. R. Daly, S. A. Kozimor, W. W. Lukens, R. L. Martin, D. Nordlund, G. T. Seidler, D. K. Shuh, D. Sokaras, T. Tyliszczak, G. L. Wagner, T.-C. Weng and P. Yang, *J. Am. Chem. Soc.*, 2013, **135**, 1864–1871.
110 H. S. La Pierre, S. G. Minasian, M. Abubekerov, S. A. Kozimor, D. K. Shuh, T. Tyliszczak, J. Arnold, R. G. Bergman and F. D. Toste, *Inorg. Chem.*, 2013, **52**, 11650–11660.
111 T. L. Gianetti, G. Nocton and S. G. Minasian, *J. Am. Chem. Soc.*, 2013, **135**, 3224–3236.
112 K. R. Meihaus, S. G. Minasian and W. W. Lukens Jr, *J. Am. Chem. Soc.*, 2014, **136**, 6056–6068.
113 T. Warwick, N. Andresen and J. Comins, *AIP Conf. Proc.*, 2004, **705**, 458–461.
114 A. P. Hitchcock. aXis2000, V. 15-Jan-15; McMaster University: Hamilton, Ontario,

Canada, 2008; http://unicorn.mcmaster.ca/axis/ aXis2000 (accessed May 12, 2014).
115 T. C. Weng, G. S. Waldo and J. E. Penner-Hahn, *J. Synchrotron. Radiat.*, 2005, **12**, 506–510.
116 G. N. George, *EDG_FIT*. Stanford, CA; 2000.
117 P. Hohenberg and W. Kohn, *Phys. Rev.*, 1964, **136**, B864–B871.
118 L. J. Sham and W. Kohn, *Phys. Rev.*, 1965, **140**, A1133–A1138.
119 P. E. Blochl, *Phys. Rev. B*, 1994, **50**, 17953–17979.
120 G. Kresse and J. Furthmuller, *Phys. Rev. B*, 1996, **54**, 11169–11186.
121 J. P. Perdew, K. Burke and M. Ernzerhof, *Phys. Rev. Lett.*, 1996, **77**, 3865–3868.
122 S. Grimme, *J. Comput. Chem.*, 2006, **27**, 1787–1799.
123 A. H. England, A. M. Duffin, C. P. Schwartz, J. S. Uejio, D. Prendergast and R. J. Saykally, *Chem. Phys. Lett.*, 2011, **514**, 187–195.
124 C. D. Pemmaraju, R. Copping, S. Wang, M. Janousch, S. J. Teat, T. Tyliszcak, A. Canning, D. K. Shuh and D. Prendergast, *Inorg. Chem.*, 2014, **53**, 11415–11425.
125 P. Giannozzi, S. Baroni, N. Bonini, M. Calandra, R. Car, C. Cavazzoni, D. Ceresoli, G. L. Chiarotti, M. Cococcioni, I. Dabo, A. Dal Corso, S. de Gironcoli, S. Fabris, G. Fratesi, R. Gebauer, U. Gerstmann, C. Gougoussis, A. Kokalj, M. Lazzeri, L. Martin-Samos, N. Marzari, F. Mauri, R. Mazzarello, S. Paolini, A. Pasquarello, L. Paulatto, C. Sbraccia, S. Scandolo, G. Sclauzero, A. P. Seitsonen, A. Smogunov, P. Umari and R. M. Wentzcovitch, *J. Phys.: Condens. Matter*, 2009, **21**, 395502.
126 D. Vanderbilt, *Phys. Rev. B*, 1990, **41**, 7892–7895.
127 D. Prendergast and S. G. Louie, *Phys. Rev. B*, 2009, **80**, 235126.
128 T. Körzdörfer, S. Kümmel, N. Marom and L. Kronik, *Phys. Rev. B*, 2009, **79**, 201205.
129 K. Momma and F. Izumi, *J. Appl. Crystallogr.*, 2011, **44**, 1272–1276.

Chapter 2

Chemical and morphological inhomogeneity of aluminum metal and oxides from soft X-ray spectromicroscopy

Overview

Due to the favorable energetics of aluminum combustion, aluminum metal nanomaterials are of interests as fuels; however, aluminum metal is only known to exist with passivating aluminum oxides layers. Chapter 1 detailed the development of Al K-edge X-ray absorption spectroscopy to understand the electronic structure of molecular aluminum complexes in terms of their molecular orbitals. The following chapter translates these tools into a band structure and density of states framework for understanding simple aluminum materials. This allowed for the assignment of spectroscopic signatures as well as determination of chemical speciation in multicomponent samples. This work has been recently published: A. B. Altman, C. D. Pemmaraju, S. Alayoglu, J. Arnold, C. H. Booth, A. Braun, C. E. Bunker, A. Herve, S. G. Minasian, D. Prendergast, D. K. Shuh and T. Tyliszczak "Chemical and Morphological Inhomogeneity of Aluminum Metal and Oxides from Soft X-ray Spectromicroscopy" *Inorg. Chem.* **2017**, *56*, 5710-5719.

Introduction

Efforts to utilize aluminum and other oxophilic metals require a precise grasp of surface structure and composition, as well as passivation techniques to control surface reactivity. Aluminum materials do not exhibit ideal, bulk-like surface terminations, which becomes an increasingly dominant characteristic of their chemistry as the surface-area to volume ratio increases. In the case of aluminum, the metal typically has a ~5 nm passivating layer of Al_2O_3,[1] such that the weight % of O in nanoparticles increases as particle size decreases. Al_2O_3 is commonly found in a number of different amorphous (*am*) and crystalline phases (α and γ, among others). However, relatively little is known about how the coexistence of multiple crystalline structures at an interface can result in heterogeneous oxide systems with unusual porosity, electronic structure, thermodynamic stability, and reactivity. Hence, unraveling the rates and mechanisms of Al metal reactivity with O_2 in fine powders, nanoparticles, thin films, and molecular clusters has been the subject of considerable experimental[2-7] and theoretical effort.[8-13] Understanding how changes in the phase of Al_2O_3 can impact reactivity has important consequences for scientific and technological applications for aluminum in ceramics, catalysis, coatings, separations,[14-20] and energetic materials.[21-25] To optimize the synthesis of well-defined nanoparticles and control their reactivities, characterization tools are needed that can probe the structure of heterogeneous materials over multiple length scales and under real-world conditions.

X-ray absorption spectroscopy using a scanning transmission X-ray microscope (STXM-XAS) has emerged as powerful probes of nano- and microscale physical structure and chemical bonding for aluminum materials.[26,27] It also has unique advantages and limitations when compared with the electron-based analogues: scanning transmission electron microscopy (STEM) and electron energy-loss spectroscopy (STEM-EELS).[28] For example, modern STEM capabilities regularly achieve 0.1 nm spatial resolution and monochromated EELS can provide as fine as 0.2 eV energy resolution. STXM can accommodate thicker samples (1 to 20 μm depending on the X-ray probe energy, relative to 0.5 μm for STEM when conducted with a fixed energy electron beam), but the spatial resolution is limited to about 25 nm by the focusing ability of the X-ray optic. Modern STXM instruments easily achieve 0.1 eV energy resolution under normal conditions (resolving power $E/\Delta E > 7500$), and XAS collected in the transmission mode can be obtained from the core-levels of many elements in the Periodic Table, including the light atom K-edges for B, C, N, O, F, Na, Mg, Al, and Si. Previous studies have shown that the

spectroscopic accuracy of STXM-XAS[29-32] provides bulk-like electronic structure information that can be interpreted quantitatively within a band structure or molecular orbital model.[33-37] Additionally, X-ray based microscopes are ideally-suited for sensitive inorganic materials because compositional changes or other damaging effects that can occur on exposure to vacuum or to an electron beam are more easily controlled.[38,39]

In this study, images from a STXM were used to evaluate the chemical speciation and morphology for several reference materials as well as aluminum nanoparticles prepared under different synthetic conditions. The reference materials included a 100 nm aluminum metal foil, α-Al_2O_3, and γ-Al_2O_3. Aluminum nanoparticles (Al NPs) prepared with three different synthetic methodologies were also explored: core-shell Al NPs with 54 nm average diameters, prepared with a protective organic coating of oleic acid (Al–OA NPs);[40] bare Al NPs with 100 nm average diameters and no protective coating, prepared by the electrical explosion of wires (similar to ALEX®);[39,41] bare Al NPs with 18 nm average diameters and no protective coating, prepared by pulsed laser ablation of Al targets in an organic solvent.[42,43] These analytes were specifically chosen because they provided a range of particle sizes, compositions, surface chemistries, and reactivities.[44-47] For example, previous studies showed that protecting agents including organic ligands[40,48-54] and polymer[55-57] or metal coatings[44,58,59] enhanced reactivity properties and provided chemical control over structural attributes like particle size and monodispersity. The STXM-XAS results were consistent with earlier spectromicroscopy studies,[26,55,60] and also revealed new differences in the surface and micron-scale speciation of Al nanoparticles.

Results and Discussion

Scanning Transmission X-ray Microscopy. The 100 nm Al foil and 18 and 100 nm Al NPs were obtained from commercial sources and used as received (see Experimental Details). The protected, core-shell Al–OA NPs were prepared according to the literature procedure, and a 54 nm average size was determined by transmission electron microscopy (TEM).[40] Powder X-ray diffraction (PXRD) patterns were obtained from all the samples to evaluate the purity of analytes used in subsequent STXM measurements. In each case, the PXRD patterns were consistent with the presence of predominantly face-centered cubic aluminum metal. For the 100 nm Al NPs, the PXRD measurements also provided evidence for a minor component of hydrated alumina, α-Al_2O_3•$(H_2O)_3$. No evidence for α-Al_2O_3 was observed in the PXRD patterns from the 18 nm Al NPs and 54 nm Al–OA NPs. However, weak reflections were observed that could not be definitively assigned, and may have been evidence of small amounts of Al_2O_3 present in other polymorphs (e.g., β-, θ-, κ-Al_2O_3).

The STXM at the Molecular Environmental Science beamline 11.0.2 of the ALS was used to collect images, elemental maps, and O and Al K-edge XAS spectra from a 100 nm Al foil and the three different types of Al NPs described above.[61-63] To minimize degradation of the air- and water-sensitive materials, samples were encapsulated between Si_3N_4 supports in an argon-filled glovebox. In addition, the STXM was filled with a partial atmosphere of helium during acquisition. The STXM was used to collect single-energy images and elemental contrast maps by raster-scanning the sample and collecting transmitted monochromatic light as a function of sample position. Figure 2.1 shows representative normal contrast images and elemental maps from micron-scale aggregates of nanometer-sized particles. Lighter regions in the elemental maps corresponded to greater concentration of the absorbing atom, and were obtained by subtraction of two images: one taken at an energy just below the edge and another taken at the absorption maximum (see “X-ray Absorption Spectroscopy” below). For example, elemental

mapping at the Al K-edge was used to identify particles containing metallic aluminum by subtracting an image obtained at 1550 eV from another at 1560 eV. Regions containing Al_2O_3 were identified at the Al K-edge with energies of 1555 and 1571 eV and at the O K-edge with energies of 530 and 540 eV.

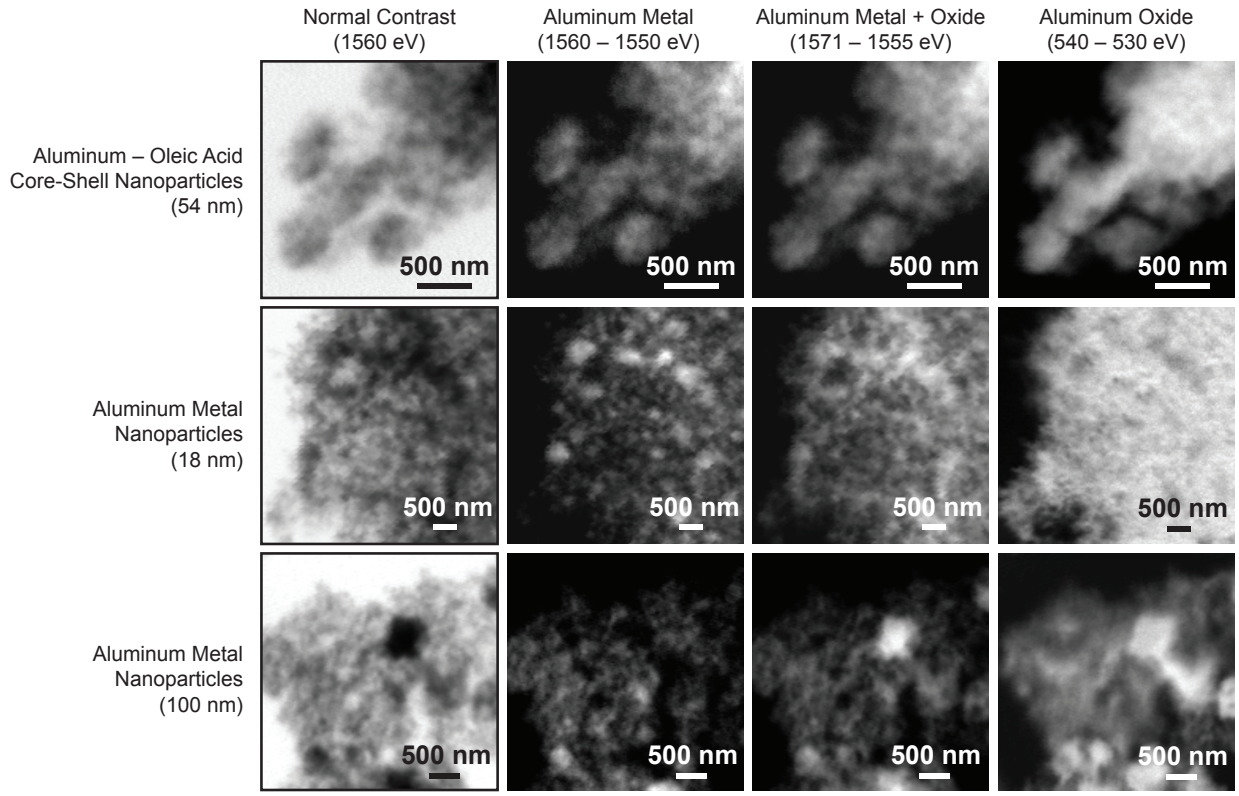

Figure 2.1. Representative contrast images and elemental difference maps obtained from aggregates of aluminum nanoparticles from which XAS were obtained. Difference maps were produced by obtaining images at the two energies indicated at the top of each column. Subtraction of a background image taken at an energy just below the absorption edge from another image taken at an energy on the absorption maximum generated the difference map, where lighter regions indicate greater concentration of the absorbing atom.

The images in Figure 2.1 show that all of the NPs had small diameters on the nanometer scale. In powdered form, all the materials formed tight micron-scale aggregates, as had been observed previously for both bare NPs and NPs protected by inorganic and organic surface layers.[55,60,64] Although many details of the nanoscale structure exceeded the spatial-resolution capability of STXM (40 nm under the experimental conditions used), on a large scale the Al–OA NPs were monodispersed and had a uniform distribution of metallic Al and Al_2O_3. In contrast, the STXM images of the 18 and 100 nm Al NPs revealed inhomogeneities in the distribution of metallic aluminum and Al_2O_3, and showed that particle sizes ranged from the nano to the micrometer scale. These observations agreed well with earlier scanning electron microscopy (SEM) and TEM measurements on ALEX® (an ultra-fine aluminum powder produced by the electrical explosion of wires), which showed that while most particle diameters were on the order of 100 nm, particles as small as 20 nm and up to 500 nm in diameter were also observed.[39]

The STXM images shown in Figure 2.1 did not provide a direct measure of the thickness

of the passivating shells of aluminum oxides. However, relative amounts of metallic aluminum and aluminum oxide in the nanomaterials were evaluated from the images by considering the O and Al K-edge spectroscopic results (*vide infra*) and conducting Singular Value Decomposition (SVD) analysis.[65] The optical density of a target area in a given image was governed by OD = $\mu \times \rho \times t$, where μ was the mass absorption coefficient, ρ was the density, and t was the sample thickness or path length. In this study, the intensity of the Al K-edge spectrum (OD) at 1560 eV was proportional to the concentration ($\rho \times t$) of metallic Al in the target area of a given particle. Similarly, the intensity of the O K-edge spectrum (OD) at 540 eV was proportional to the surface concentration of Al_2O_3 in the same target area. Using these concentrations, values for the weight percent of Al and Al_2O_3 were determined and are given in Table 2.1. To provide an accurate measurement, analyses encompassed a number of individual particles and were conducted on large target areas greater than 10 μm^2 and 10,000 total pixels. The chemical composition of surface species was identified from the O and Al K-edge XAS results (*vide infra*). It is worth noting that a limitation of the SVD approach arose from the assumption that surfaces were comprised of a single phase of Al_2O_3, when a more complex mixture of multiple oxide phases, hydroxides, and hydrated surface species could have been present.

Table 2.1. Characteristics of Al metal and nanoparticle materials determined from STXM–XAS. For nanoparticle-based samples, estimation of the oxide layer thickness (t_{oxide}) was based on the relative weight percents of each constituent, and assumed an idealized spherical morphology with a homogenous layer of γ-Al_2O_3 (ρ = 3.7 g cm^{-3}). For the 100 nm Al foil, estimation of t_{oxide} was based on a homogenous layer of *am*-Al_2O_3 (ρ = 2.3 g cm^{-3}).[a]

				Weight % of Constituents			
Cmpd	diameter (nm)	passivation	Source	OA	Al_2O_3	metallic Al	t_{oxide} (nm)
Al foil	100	air	Luxel	–	12 ± 1	88 ± 8	3.9 ± 0.4
Al NPs	18	air	US Nano	–	53 ± 5	47 ± 4	1.7 ± 0.2
Al NPs	100	air	US Nano	–	34 ± 3	66 ± 6	5.2 ± 0.5
Al–OA NPs	54	oleic acid	this work	13 ± 1	29 ± 2	58 ± 5	2.3 ± 0.4

[a] Values for the density of *am*-Al_2O_3 vary widely.[66] Using ρ = 3.6 g cm^{-3} for *am*-Al_2O_3 provides r_{oxide} = 2.5 ± 0.3 nm for the 100 nm Al foil.

For the Al foil described above, this analysis showed that the foil had surface concentrations of 3.6 ± 0.3 μg cm^{-2} oxygen and 56 ± 4.0 μg cm^{-2} aluminum. If all the oxygen was associated with a layer of amorphous alumina (*am*-Al_2O_3, ρ = 2.3 g/cm^3),[38] then these values correspond to 88 ± 8 wt. % metallic aluminum and 12 ± 1 wt. % *am*-Al_2O_3. The thickness of the foil (104 ± 11 nm) was calculated by dividing the surface concentration by density of aluminum metal. Likewise, the thicknesses of Al_2O_3 layers on the top and bottom of the Al foil were calculated at 3.9 ± 0.4 nm each depending on the value for the density of *am*-Al_2O_3 used. These values were similar to specifications for the Al foil quoted by the manufacturer,[67] which included thicknesses of 100 and 5 nm and compositions of roughly 86 and 14 wt. % for Al metal and *am*-Al_2O_3, respectively.

Relative amounts of Al metal and oxide for the conventionally-synthesized nanoparticles were determined using SVD analysis in a similar fashion (Table 2.1). The 18 nm Al NPs had 53 ± 5 wt. % Al_2O_3 and 47 ± 4 wt. % metallic Al, and the 100 nm Al NPs had 34 ± 3 wt. % Al_2O_3

and 66 ± 6 wt. % metallic Al. As described in the introduction, these changes in composition were anticipated given the increased fraction of metallic Al in larger particles. The STXM derived values suggested that there was somewhat less metallic Al in the 100 nm nanoparticles used in this study (66 ± 6 wt. %) than was determined for a different sample of 100 nm ALEX® NPs using a volumetric analysis (86% metallic Al) and using energy dispersive spectroscopy (EDS) from TEM (90 ± 5 wt. % total Al and 10 ± 2 wt. % O, which corresponded to 79 ± 5 wt. % metallic Al and 21 ± 4 wt. % Al_2O_3).[41,68] As described above for the Al foil, these relative amounts of Al and Al_2O_3 were also used to calculate thicknesses for the Al_2O_3 passivation layer by assuming an ideal spherical morphology and monodisperse 18 and 100 nm particle diameters (Table 2.1). This analysis showed that the conventionally-synthesized 18 nm and 100 nm Al NPs had 1.7 ± 0.2 and 5.2 ± 0.5 nm thick Al_2O_3 layers, respectively.

For the Al–OA core-shell nanoparticles, proportions of 58 ± 5, 29 ± 2, 13 ± 1 wt. % were calculated for the metallic core, Al_2O_3, and carbonaceous organic layer, respectively. For comparison, previous ICP-MS and TGA studies suggested that 40% of the sample mass was metallic aluminum, 25% was Al_2O_3, and 35% was organic.[40] In both cases, the amount of oxygen relative to carbon was larger than anticipated for oleic acid alone, indicating that oleic acid passivation did not completely inhibit growth of an aluminum oxide layer. This observation was consistent with earlier studies, which showed that passivation resulted in decomposition of the oleic acid and formation of an organic outer layer on the surface on an intermediate oxide layer.[40] A thickness of 2.3 ± 0.4 nm was estimated for the Al_2O_3 passivation layer in the Al–OA NPs, which also agreed with earlier work showing that organic or inorganic protective coatings limited growth of the Al_2O_3 layer to about 2 nm.[44,55,69]

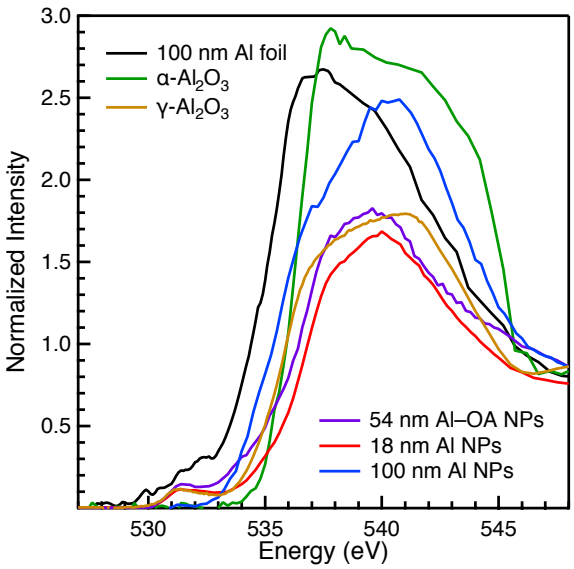

Figure 2.2. O K-edge XAS data for 54 nm Al–OA nanoparticles (purple), 18 nm Al NPs (red), 100 nm Al NPs (blue), and reference materials including a 100 nm Al metal foil (black), α-Al_2O_3 (green) and γ-Al_2O_3 (brown).

X-ray Absorption Spectroscopy. Figure 2.2 shows the background-subtracted and normalized oxygen K-edge XAS measured from the bare 18 and 100 nm Al NPs, core-shell Al–OA NPs, and reference materials α-Al_2O_3, γ-Al_2O_3, and a 100 nm Al foil. As previous studies

showed,[11,30,38] differences in the O K-edge XAS reflected changes in Al–O bonding found for different phases of aluminum oxides and hydroxides. The O K-edge spectra shown in Figure 2.2 were similar in many regards; however, some important differences were readily apparent. For example, the spectrum for γ-Al_2O_3 exhibited a small shoulder near 531 – 532 eV that was not observed for α-Al_2O_3. Previous work by Århammar and coworkers suggested that these small features were characteristic of O–O interactions present in some phases of Al_2O_3 but not in crystalline α-Al_2O_3.[38] The spectra from the 18 and 100 nm Al NPs and Al–OA NPs each had some of the spectroscopic signatures observed from γ-Al_2O_3. None of the nanoparticle spectra resembled the O K-edge of the 100 nm Al foil (reflecting *am*-Al_2O_3), which was shifted such that the first inflection point was approximately 1 eV lower in energy than was observed for the other materials.

Al K-edge XAS was used to further elaborate on the compositional assignments determined using O K-edge XAS. Figure 2.3 shows representative background subtracted and normalized Al K-edge spectra obtained from the bare 18 and 100 nm Al NPs, core-shell Al–OA NPs, and reference materials α-Al_2O_3, γ-Al_2O_3, and the 100 nm Al foil. Energies and assignments for the spectral features are summarized in Table 2.2. Because previous attempts to model and interpret Al K-edge XAS data for the metal and oxide references had been limited,[31,70,71] this discussion will begin by establishing the bonding descriptions needed to justify the spectral assignments for the nanoparticle materials given in Table 2.2.

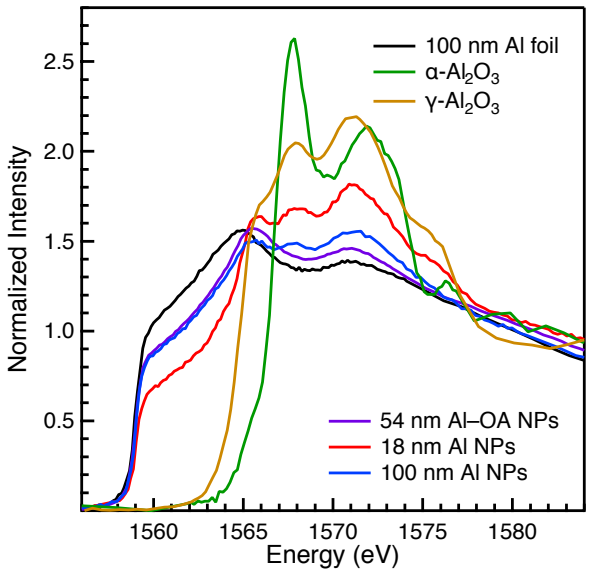

Figure 2.3 Al K-edge XAS for 54 nm Al–OA nanoparticles (purple), 18 nm Al NPs (red), 100 nm Al NPs (blue), and reference materials including a 100 nm Al metal foil (black), α-Al_2O_3 (green), and γ- Al_2O_3 (brown).

Table 2.2. Al K-edge feature energies and assignments.

Compound	Energy (eV)	Assignment
α-Al_2O_3	1564.9[a]	1s → 2s-σ* (a_{1g})
	1567.8	1s → 3p-σ/π* (t_{1u})
	1571.9	1s → 3d-σ* (t_{2g})
γ-Al_2O_3	1565.4	1s → 3p-σ/π* (t_2)
	1568.0	1s → 3p-σ/π* (t_{1u})
	1571.2	1s → 3d-σ* (t_{2g})
100 nm Al foil	1559.0	1s → 3p-π[b]
	1564.9	1s → 3p-σ*
	1570.8	1s → 3d-σ*
18 nm Al NPs	1559.0	1s → 3p-π[b]
	1565.9	1s → 3p-σ/π* (t_2)
	1568.0	1s → 3p-σ/π** (t_{1u})
	1571.1	1s → 3d-σ* (t_{2g})
100 nm Al NPs	1559.0	1s → 3p-π[b]
	1565.6	1s → 3p-σ/π* (t_2)
	1567.8	1s → 3p-σ/π* (t_{1u})
	1571.1	1s → 3d-σ* (t_{2g})
54 nm Al–OA NPs	1559.0	1s → 3p-π[b]
	1565.6	1s → 3p-σ/π* (t_2)
	1570.9	1s → 3d-σ*

[a] This transition is weak and dipole-forbidden, but becomes recognizable as a result of some distortion from idealized O_h symmetry which may facilitate some Al 3s and 3p mixing.

Bulk Aluminum Metal. Figure 2.4 shows the experimental Al K-edge XAS of a 100 nm Al foil and simulations provided by both FEFF 10.0.1[72,73] and XCH DFT calculations. Both theoretical approaches provided good agreement with the experimental data in both the near-edge and extended energy regions. The onset of the Al K-edge for Al metal, defined by the first inflection point, was fixed at 1559.0 eV and was the calibration point for the other Al K-edge spectra described below. At higher energies, the edge region was characterized by two very broad features at 1564.9 and 1570.8 eV. Although Al K-edge spectra of Al metal have been reported,[74-81] to the best of our knowledge no detailed interpretation of the spectral profile has been provided. The discussion below begins by constructing the band structure model for Al metal that was used to understand the Al K-edge XAS features.

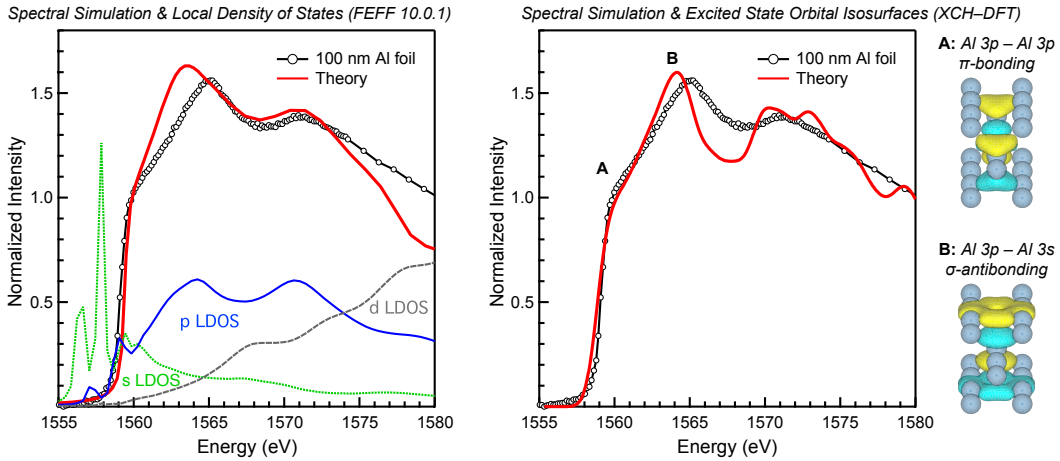

Figure 2.4. Al K-edge XAS of Al metal (black circles) compared with simulations from FEFF (left) and XCH-DFT (right) calculations. In the left plot, the total simulation (red) is included with the local density of states (LDOS) derived from the FEFF for final states associated with the Al s, p, or d orbitals (green, blue, and gray). In the right plot, the correspondence between transitions and isosurfaces is indicated by the letters A and B. Note that the FEFF calculation is shifted down by approximately 5 eV to better compare to the Al K edge experimental data, which is a typical absolute energy disagreement for FEFF. Similarly, the XCH-DFT simulation was shifted by +1560.65 eV.

From a chemistry perspective, molecular orbital theory can provide a useful starting point for understanding metallic bonding.[82-84] Figure 2.5 illustrates this approach for the construction of molecular orbitals in aluminum metal, beginning with the hypothetical aluminum molecule Al_2. To a first approximation, interaction of the two 3s atomic orbitals results in formation of two molecular orbitals of σ-symmetry, which are split in energy as the bonding and antibonding combinations. Similarly, the six 3p orbitals form bonding and antibonding orbitals with both σ- and π-symmetries. Furthermore, because the 3s and 3p σ-bonding orbitals have the same symmetry and similar energies (11.3 and 5.9 eV, respectively),[84] they can interact via s-p mixing to form new orbitals with different energies. Castleman *et al*. previously used vacuum ultraviolet photoelectron imaging to highlight the importance of s-p hybridization in small aluminum clusters formed in the gas phase.[85] Consequently, Al_2 has a ground-state electronic configuration of $(1\sigma_g^+)^2(1\sigma_u^+)^2(1\pi_u)^2$ where the partially occupied $1\pi_u$ orbitals are bonding, and the empty $2\sigma_g^+$ orbitals are best described as non-bonding resulting from s-p mixing. The orbitals described for Al_2 are split again when an infinite array of Al atoms are brought together in the metal, resulting in a band of tightly packed energy levels corresponding to both bonding and antibonding states.

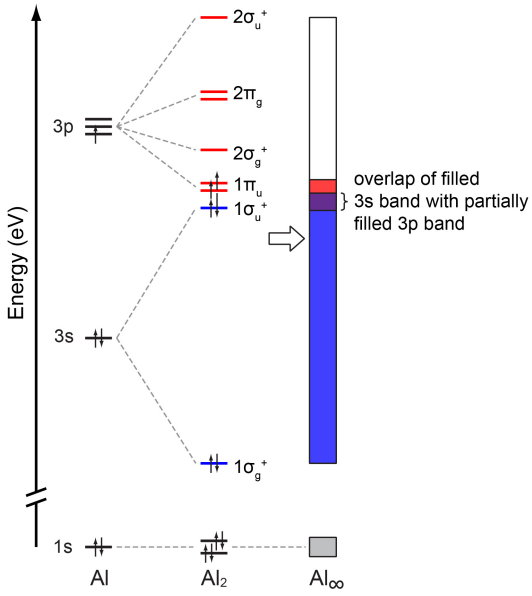

Figure 2.5. Formation of energy bands in aluminum metal. Orbitals for an isolated Al atom (left) form σ- and π-type interactions in a diatomic molecule (middle) which are split into bonding and antibonding counterparts. Bringing together a large number of atoms in an extended lattice results in a larger number of closely spaced energy levels.

This qualitative picture is consistent with the quantitative Al K-edge XAS simulations obtained using FEFF 10.0.1 and XCH-DFT, shown in Figure 2.4. As expected, the local density of states provided by the FEFF calculation showed that the occupied bands have predominantly 3s character, while at higher energies the unoccupied bands have primarily Al 3p character. In addition, XCH-DFT calculations were used to generate isosurface plots of the final state electronic orbitals that corresponded to (A) the most dominant transitions near the edge onset, and (B) transitions that were close to the energy of the first main feature at 1564.9 eV (Figure 2.4). Consistent with the qualitative interpretation provided above, the orbital isosurfaces showed that transitions near the edge onset at 1559 eV involved low–lying empty states with significant π-bonding character between adjacent atoms in the unit cell (Al 1s → π^b). The calculations also showed an additional feature at 1563.6 eV (FEFF) and 1564.2 eV (XCH-DFT), which corresponded to the broad peak at 1564.9 eV in the experimental spectrum. The peak was reminiscent of a shape resonance: a broad feature associated with short-lived final states, given the increasing probability of decay to the continuum at energies above the Al 1s ionization potential.[86] The orbital isosurfaces in Figure 2.4 confirmed this interpretation and showed that the states associated with the feature at 1564.9 eV were best described as σ-antibonding between one Al 3p orbital and additional Al 3s orbitals in the plane above and below. Finally, the feature at 1570.8 eV in the experimental and simulated spectra was not easily assigned using the simple band structure provided above; however, the LDOS provided by the FEFF calculations indicated that transitions to states with some Al 3p and Al 3d character may have been present.

Aluminum Oxides: The background-subtracted and normalized Al K-edge XAS of α- and γ-Al_2O_3 are shown in Figure 2.3. The edge onset for each of the oxides was several eV higher in energy relative to the Al foil. These shifts to higher energy for trivalent oxides resulted from an increase in effective nuclear charge and concomitant stabilization of the Al 1s core levels. Previous Al K-edge analyses of α-Al_2O_3 and other aluminum oxides and minerals have provided

frameworks for assigning transitions in the Al K-edge XAS by constructing models for Al–O bonding in both tetrahedral or octahedral coordination environments.[27,87-91] A similar approach was applied here to develop interpretations of the Al K-edge spectra of α- and γ-Al_2O_3 that could be related to the nanoparticle systems.

The α-Al_2O_3 spectrum had a weak shoulder at 1564.9 eV and two main features at 1567.8 and 1571.9 eV, and closely resembled previously published spectra.[27,87-91] In their detailed examination of aluminosilicate minerals, Li and coworkers developed assignments by comparing Al K-edge and Si K-edge spectra and using MO calculations of the AlO_6^{9-} cluster. Using their assignments for α-Al_2O_3, the very weak and low energy shoulder at 1564.9 eV was assigned to dipole-forbidden transitions from the Al 1s into Al 3s and O 2p antibonding orbitals of a_{1g} symmetry. The first main feature at 1567.8 eV was assigned to transitions from the Al 1s orbitals into Al 3p and O 2p antibonding orbitals of t_{1u} symmetry. The second main feature at 1571.9 eV was assigned to transitions from the Al 1s to final states derived from the Al 3d orbitals of t_{2g} symmetry.

The γ-phase of Al_2O_3 has a spinel-type structure consisting of both octahedral and tetrahedral Al coordination sites; hence, the Al K-edge spectrum of γ-Al_2O_3 was regarded as a superposition of Al K-edge spectra involving the two different symmetries. For example, the two main features at 1568.0 and 1571.2 eV reflected the octahedral coordination environment for Al and were assigned to Al 1s → t_{1u} and Al 1s → t_{2g} transitions as described above for α-Al_2O_3. Using assignments developed previously for γ-Al_2O_3 and aluminosilicate minerals with strictly tetrahedral Al coordination sites,[74,90] the low-energy shoulder at 1565.4 eV in the Al K-edge XAS of γ-Al_2O_3 was assigned to transitions from Al 1s orbitals into Al 3p and O 2p antibonding orbitals of t_2 symmetry. The 2.6 eV increase in energy for Al 1s → t_{1u} transitions relative to the Al 1s → t_2 transitions was attributed to an increase in Al–O overlap expected for six-coordinate octahedral environments.[92] Finally, the additional high-energy shoulder observed at approximately 1575 eV was attributed to a transition from the Al 1s to final states derived from the Al 3d orbitals of e symmetry.

Aluminum Nanoparticles: The spectra from the unsupported metallic Al foil and nanoparticles each exhibited an edge feature at 1559 eV, which indicated that metallic aluminum was a significant component of the nanoparticle materials. However, the Al K-edge spectra also exhibited rich spectral detail reflecting differences in the surface chemistry. For example, each of the nanoparticle materials had a feature between 1565.6 – 1565.9 eV that was not observed in the spectrum from the Al foil. In addition, α-Al_2O_3, γ-Al_2O_3 and both the 18 and 100 nm Al NPs had features at near 1568 eV that were not observed in the spectrum from either the Al foil or the Al–OA NPs. These differences were associated changes in the nature of the oxide layer, and were rationalized by considering the assignments developed above.

The spectral profiles for the conventionally-synthesized 18 and 100 nm Al NPs and the protected Al–OA NPs were similar in that clearly-resolved features with similar intensities and energies were observed at 1565.9, 1565.6, and 1565.6 eV, respectively. These features were also equivalent in energy to those assigned as Al 1s → t_2 transitions observed in the Al K-edge XAS of γ-Al_2O_3 (1565.4 eV). The 18 and 100 nm Al NPs were unique in that they also had features in the Al K-edge XAS at intermediate energies of 1568.0 and 1567.8 eV, and also at higher energies of 1571.1 eV for both, which were recognized as distinct from those observed from the Al foil. These intermediate features were very close to the energy observed for the Al 1s → t_{1u} transitions in the Al K-edge spectrum of both α-Al_2O_3 (1567.8 eV) and γ-Al_2O_3 (1568.0 eV). Likewise, the higher energy features were similar to the Al 1s → t_{2g} transitions observed for γ-

Al_2O_3 (1571.2 eV). Taken together, these observations showed that the oxidation of 18 and 100 nm Al NPs resulted in formation of an oxide layer containing both tetrahedral and octahedral Al coordination sides, which was similar to the γ-phase of Al_2O_3. Oxidation of the Al–OA NPs also resulted in formation of an Al_2O_3 layer containing tetrahedral Al coordination sites; however, no signatures of octahedral Al coordination sites were detected.

Conclusions

The results provided in this study showed that soft X-ray spectromicroscopy could provide unique insight into the complex interfacial chemistry of electropositive, oxophilic metals such as aluminum. Because exposure to vacuum or an electron beam could induce compositional changes in some nanoscale particles and surfaces, spectromicroscopy measurements were conducted at ambient pressure with soft X-rays to ensure that quantitative information was obtained.[38,39] The normal contrast images and respective elemental maps showed that the thickness of the oxide layer was between 2 and 5 nm for all the aluminum materials studied. The images also showed that the oxide was evenly distributed in oleic-acid protected NPs; however, there was more oxide inhomogeneity in bare, unprotected 18 and 100 nm Al NPs. Features in the Al K-edge XAS of the aluminum nanoparticles were also compared with spectra obtained from reference materials including α-Al_2O_3, γ-Al_2O_3, and a 100 nm aluminum metal film. This comparison revealed that the oleic acid protected nanoparticles had an oxide layer with primarily tetrahedral Al coordination sites, while oxidation of the unprotected 18 and 100 nm Al NPs resulted in formation of both octahedral and tetrahedral coordination sites (similar to those found in γ-Al_2O_3). These observations were consistent with previously published results, and also provided new quantitative insight that was not obtained from analysis of PXRD patterns and TEM images alone. Combined, these results supported the viewpoint that advanced synthetic strategies including organic passivation do not eliminate surface oxidation of aluminum metal, but can be used to tune the chemistry of the oxide layer and control its reactivity.[40]

Experimental Details

General Synthetic Details. All reactions were performed either using standard Schlenk line techniques or in a MBraun inert atmosphere glovebox under a purified nitrogen atmosphere (<0.1 ppm O_2/H_2O). The aluminum foil filter (100 nm thickness) and aluminum nanopowders was purchased from Luxel Corporation and US Research Nanomaterials, Inc, respectively, and used as received. Oleic acid aluminum core-shell nanoparticles were synthesized according to the literature procedure and dried before use.[40] α and γ-Al_2O_3 were purchased from Aldrich and Strem and dried at 100 °C and 1 x 10^{-3} torr for 24 h before use. Sample preparation and methodology for handling air-sensitive analytes was similar to that described previously.[29,31,93] Samples were prepared in an argon-filled glovebox by grinding crystals of the analyte into a fine powder with a mortar and pestle, and brushing the powder onto a Si_3N_4 membrane (100 nm, Silson) with a fiber. This method arranged a large number of micron-scale crystals that were suitable for Al K-edge measurements in a relatively compact area. A second membrane was placed over the sample, and the edges were sealed together using Hardman Double/Bubble® 5 minute epoxy.

Beamline Characteristics. STXM methodology was similar to that discussed previously.[88-91] Single-energy images and Al K-edge XANES spectra were acquired using the STXM instrument at the Molecular Environmental Science (MES) beamline 11.0.2 at the Advanced Light Source (ALS), which was operated in topoff mode at 500 mA, in a ~0.5 atm He-

filled chamber.[61-63] The beamline used photons from an elliptically polarizing undulator that delivered photons in the 100 to 2000 eV energy range to a variable-included-angle plane-grating monochromator. For Al K-edge measurements, the photon energy of the high energy diffraction grating (1100 lines/mm) was calibrated to the Al K-edge from the 100 nm aluminum foil filter sample (inflection point = 1559.0 eV). Both of the 4-jaw exit slit widths were set to 30 μm. The maximum energy resolution $E/\Delta E$ was previously determined at better than 7500, which was consistent with the observed standard deviation for spectral transitions of ± 0.3 eV determined from comparison of spectral features over multiple samples and beam runs. For these measurements, the X-ray beam was focused with a 40 nm zone plate onto the sample, and the transmitted light was detected with a photomultiplier tube. Images at a single energy were obtained by raster-scanning the sample and collecting transmitted monochromatic light as a function of sample position. Spectra at particular regions of interest on the sample image were extracted from the "stack", which is a collection of images recorded at multiple, closely spaced photon energies across the absorption edge. Dwell times used to acquire an image at a single photon energy were 2 ms per pixel. To quantify the absorbance signal, the measured transmitted intensity (I) was converted to optical density using Beer−Lambert's law: $OD = \ln(I/I_0) = \mu\rho d$, where I_0 is the incident photon flux intensity, d is the sample thickness, and μ and ρ are the mass absorption coefficient and density of the sample material, respectively. Incident beam intensity was measured through the sample-free region of the Si_3N_4 windows. Regions of particles with an absorption of >1.5 OD were omitted to ensure the spectra were in the linear regime of the Beer−Lambert law. The data were background subtracted using the *MBACK* algorithm in *MATLAB*,[94] and peak positions were determined from derivative plots generated using the program IGOR 6.0.

FEFF Calculations. FEFF 10.0.1[72,73] calculations utilized a Hedin-Lundqvist potential and converged using a self-consistent field approximation within a 6.0 Å cluster of 79 atoms and a full-multiple scattering expansion using a cluster of 55 atoms within a radius 6.6 Å. All other options were chosen to be default.

Al K-edge Spectral Simulations. XAS spectra at the Al K-edge were calculated using the excited electron and core-hole approach (XCH).[94] The XCH approach was described previously in detail.[94-96] In this method, the lowest energy X-ray excited state of the system was modeled within an occupation-constrained DFT framework employing a periodic supercell formalism wherein the core-excited atom was described through a core-hole pseudopotential and the screening due to the excited electron was taken into account self-consistently. Higher–lying X-ray excited state energies were approximated through eigenvalue differences obtained from the Kohn-Sham (KS) spectrum of the lowest energy core-excited state. X-ray transition matrix elements were calculated using Fermi's golden rule and typically for light-element K-edges, within a dipole approximation. The XCH method was utilized as implemented in a development version of the Quantum-Espresso package[97] which provided a plane-wave pseudopotential DFT framework for electronic structure calculations. Ultra-soft pseudopotentials[98] with the following valence electronic configurations were employed: Al($3s^2 3p^1$), O($2s^2 2p^4$). These were used together with a plane-wave energy cut-off of 25 Ry. To describe 1s core-excited Al in XANES simulations, a core-hole pseudopotential with the electronic configuration $1s^1 2s^2 2p^6 3s^2 3p^2$ was generated. A 3 x 3 x 3 supercell consisting of 108 atoms was used. The Brillouin zone was sampled through a 3 x 3 x 3 Γ-centered k-point grid during the Kohn-Sham self-consistent field calculation, but the band structure was interpolated over a uniform Γ-centered 5 × 5 × 5 k-point grid using the Shirley interpolation scheme[99] in order to generate XANES spectra. Within the

XCH approach, the relative energy alignment of XAS corresponding to core-excitations on atoms in different chemical environments was carried out through total energy differences.[95] However, since the method was based on core-hole pseudopotentials and does not explicitly include the energy of core electrons, calibration of the absolute energy position of the calculated spectra with respect to experiment involves a rigid energy shift Δ, which was determined to be 1560.65 eV at the Al K-edge based on the inflection point of the onset of absorption. Orbital isosurfaces were visualized using VESTA-3.[100]

References

1 H. Fujii, H. Nakae, and K. Okada, *Acta Metall.* 1993, **41**, 2963-2971.

2 M. A. Trunov, M. Schoenitz, X. Y. Zhu, and E. L. Dreizin, *Combust. Flame* 2005, **140**, 310-318.

3 Z. Luo, C. J. Grover, A. C. Reber, S. N. Khanna, and A. W. Castleman, Jr. *J. Am. Chem. Soc.* 2013, **135**, 4307-4313.

4 M. Neumaier, M. Olzmann, B. Kiran, K. H. Bowen, B. Eichhorn, S. T. Stokes, A. Buonaugurio, R. Burgert, and H. Schnoeckel, *J. Am. Chem. Soc.* 2014, **136,** 3607-3616.

5 J. C. Smith, A. C. Reber, S. N. Khanna, and A. W. Castleman, *J. Phys. Chem. A* 2014, **118**, 8485-8492.

6 P. M. Guerieri, S. DeCarlo, B. Eichhorn, T. Connell, R. A. Yetter, X. Tang, Z. Hicks, K. H. Bowen, and M. R. Zachariah, *J. Phys. Chem. A* 2015, **119**, 11084-11093.

7 Z. Luo, A. C. Reber, M. Jia, W. H. Blades, S. N. Khanna, and A. W. Castleman, Jr. *Chem. Sci.* 2016, **7**, 3067-3074.

8 W. Y. Ching, L. Ouyang, P. Rulis, and H. Yao, *Phys. Rev. B* 2008, **78**, 014106.

9 M. F. Peintinger, M. J. Kratz, and T. Bredow, *J. Mater. Chem. A* 2014, **2**, 13143-13158.

10 S. Aryal, P. Rulis, L. Ouyang, W. Y. Ching, *Phys. Rev. B* 2011, **84**, 174123.

11 H. Wu, D. Lu, K. Zhu, G. Xu, and H. Wang, *Physica B Condens. Matter* 2013, **413**, 105-108.

12 E. O. Filatova, and A. S. Konashuk, *J. Phys. Chem. C* 2015, **119**, 20755-20761.

13 E. O. Filatova, A. S. Konashuk, F. Schaefers, V. V. Afanas'ev, V. V. *J. Phys. Chem. C* 2016, **120**, 8979-8985.

14 Z. R. Zhang, R. W. Hicks, T. R. Pauly, and T. J. Pinnavaia, *J. Am. Chem. Soc.* 2002, **124**, 1592-1593.

15 R. W. Hicks, and T. J. Pinnavaia, *Chem. Mater.* 2003, **15**, 78-82.

16 M. Trueba, and S. P. Trasatti, *Eur. J. Inorg. Chem.* 2005, 3393-3403.

17 Z. Y. Yuan, T. Z. Ren, A. Azioune, J. J. Pireaux, and B. L. Su, B. L. *Chem. Mater.* 2006, **18**, 1753-1767.

18 G. Busca, *Chem. Rev.* 2007, **107**, 5366-5410.

19 C. Marquez-Alvarez, N. Zilkova, J. Perez-Pariente, and J. Cejka, *Cat. Rev. - Sci. Eng.* 2008, **50**, 222-286.

20 Q. Yuan, A. X. Yin, C. Luo, L. D. Sun, Y. W. Zhang, W. T. Duan, H. C. Liu, and C. H. Yan, *J. Am. Chem. Soc.* 2008, **130**, 3465-3472.

21 Z. W. Wang, X. Z. Yi, G. Z. Li, D. R. Guan, and A. J. Lou, *Chem. Phys.* 2001, **274**, 57-69.

22 Q. S. M. Kwok, R. C. Fouchard, A. M. Turcotte, P. D. Lightfoot, R. Bowes, and D. E. G. Jones, *Propell. Explos. Pyrot.* 2002, **27**, 229-240.

23 Y. S. Kwon, A. A. Gromov, A. P. Ilyin, and G. H. Rim, *Appl. Surf. Sci.* 2003, **211**, 57-67.

24 S. W. Chung, E. A. Guliants, C. E. Bunker, P. A. Jelliss, and S. W. Buckner, *J. Phys. Chem. Solids* 2011, **72**, 719-724.

25 F. Noor, H. Zhang, T. Korakianitis, and D. Wen, *Phys. Chem. Chem. Phys.* 2013, **15**, 20176-20188.

26 T. H. Yoon, S. B. Johnson, K. Benzerara, C. S. Doyle, T. Tyliszczak, D. K. Shuh, and G. E. Brown, *Langmuir* 2004, **20**, 10361-10366.

27 H. E. van der Bij, D. Cicmil, J. Wang, F. Meirer, F. M. F. de Groot, and B. M. Weckhuysen, *J. Am. Chem. Soc.* 2014, **136**, 17774-17787.

28 F. M. F. de Groot, E. de Smit, M. M. van Schooneveld, L. R. Aramburo, and B. M. Weckhuysen, *Chemphyschem* 2010, **11**, 951-962.
29 S. G. Minasian, J. M. Keith, E. R. Batista, K. S. Boland, J. A. Bradley, S. R. Daly, D. Sokaras, S. A. Kozimor, W. W. Lukens, R. L. Martin, D. Nordlund, G. T. Seidler, D. K. Shuh, T. Tyliszczak, G. L. Wagner, T. C. Weng, and P. Yang, *J. Am. Chem. Soc.* 2013, **135**, 1864-1871.
30 X. -D. Wen, M. W. Loeble, E. R. Batista, E. Bauer, K. S. Boland, A. K. Burrell, S. D. Conradson, S. R. Daly, S. A. Kozimor, S. G. Minasian, R. L. Martin, T. M. McCleskey, B. L. Scott, D. K. Shuh, and T. Tyliszczak, *J. Electron. Spectrosc. Relat. Phenom.* 2014, **194**, 81-87.
31 A. B. Altman, C. D. Pemmaraju, C. Camp, J. Arnold, S. G. Minasian, D. Prendergast, D. K. Shuh, and T. Tyliszczak, T. *J. Am. Chem. Soc.* 2015, **137**, 10304-10316.
32 A. B. Altman, J. I. Pacold, J. Wang, W. W. Lukens, and S. G. Minasian, *Dalton Trans.* 2016, **45**, 9948-9961.
33 S. E. Shadle, B. Hedman, K. O. Hodgson, and E. I. Solomon, *Inorg. Chem.* 1994, **33**, 4235-4244.
34 S. E. Shadle, B. Hedman, K. O. Hodgson, and E. I Solomon, *J. Am. Chem. Soc.* 1995, **117,** 2259-2272.
35 T. Glaser, B. Hedman, K. O. Hodgson, and E. I. Solomon, *Acc. Chem. Res.* 2000, **33**, 859-868.
36 S. D. George, P. Brant, and E. I. Solomon, *J. Am. Chem. Soc.* 2005, **127**, 667-674.
37 E. I. Solomon, B. Hedman, K. O. Hodgson, A. Dey, R. R. Szilagyi, *Coord. Chem. Rev.* 2005, **249**, 97-129.
38 C. Arhammar, A. Pietzsch, N. Bock, E. Holmstroem, C. M. Araujo, J. Grasjo, S. Zhao, S. Green, T. Peery, F. Hennies, S. Amerioun, A. Foehlisch, J. Schlappa, T. Schmitt, V. N. Strocov, G. A. Niklasson, D. C. Wallace, J. -E. Rubensson, B. Johansson, and R. Ahuja, *PNAS* 2011, **108**, 6355-6360.
39 M. M. Mench, K. K. Kuo, C. L. Yeh, Y. C. Lu, *Combust. Sci. Technol.* 1998, **135**, 269-292.
40 K. A. Fernando, M. J. Smith, B. A. Harruff, W. K. Lewis, E. A. Guliants, and C. E. Bunker, *J. Phys. Chem. C* 2009, **113**, 500-503.
41 A. A. Gromov, U. Forter-Barth, and U. Teipel, *Powder Technol.* 2006, **164**, 111-115.
42 S. Eliezer, N. Eliaz, E. Grossman, D. Fisher, I. Gouzman, Z. Henis, S. Pecker, Y. Horovitz, M. Fraenkel, S. Maman, and Y. Lereah, *Phys. Rev. B* 2004, **69**, 144119.
43 A. Baladi, and R. S. Mamoory, *Appl. Surf. Sci.* 2010, **256**, 7559-7564.
44 T. J. Foley, C. E. Johnson, and K. T. Higa, *Chem. Mater.* 2005, **17**, 4086-4091.
45 W. K. Lewis, A. T. Rosenberger, J. R. Gord, C. A. Crouse, B. A. Harruff, K. A. S.Fernando, M. J. Smith, D. K. Phelps, J. E. Spowart, E. A. Guliants, and C. E. Bunker, *J. Phys. Chem. C* 2010, **114**, 6377-6380.
46 S. Roy, N. Jiang, H. U. Stauffer, J. B. Schmidt, W. D. Kulatilaka, T. R. Meyer, C. E. Bunker, and J. R. Gord, *J. Appl. Phys.* 2013, **113**, 184310.
47 W. K. Lewis, C. G. Rumchik, M. J. Smith, K. A. S. Fernando, C. A. Crouse, J. E. Spowart, E. A. Guliants, and C. E. Bunker, C. E. *J. Appl. Phys.* 2013, **113**, 044907.
48 A. P. Lyashko, A. P. Ilin, and G. G. Savelev, *Russ. J. Appl. Chem.* 1993, **66**, 999-1001.
49 R. J. Jouet, A. D. Warren, D. M. Rosenberg, V. J. Bellitto, K. Park, and M. R. Zachariah, *Chem. Mater.* 2005, **17**, 2987-2996.

50 S. W. Chung, E. A. Guliants, C. E. Bunker, D. W. Hammerstroem, Y. Deng, M. A. Burgers, P. A. Jelliss, and S. W. Buckner, *Langmuir* 2009, **25**, 8883-8887.
51 H. Li, M. J. Meziani, F. Lu, C. E. Bunker, E. A. Guliants, and Y. -P. Sun, *J. Phys. Chem. C* 2009, **113**, 20539-20542.
52 M. J. Meziani, C. E. Bunker, F. Lu, H. Li, W. Wang, E. A. Guliants, R. A. Quinn, and Y. -P. Sun, *ACS Appl. Mater. Interfaces* 2009, **1**, 703-709.
53 H. Li, M. J. Meziani, A. Kitaygorodskiy, F. Lu, C. E. Bunker, K. A. S. Fernando, E. A. Guliants, and Y. -P. Sun, Y *J. Phys. Chem. C* 2010, **114**, 3318-3322.
54 D. W. Hammerstroem, M. A. Burgers, S. W. Chung, E. A. Guliants, C. E. Bunker, K. M. Wentz, S. E. Hayes, S. W. Buckner, and P. A. Jelliss, *Inorg. Chem.* 2011, **50**, 5054-5059.
55 Y. A. Atmane, L. Sicard, A. Lamouri, J. Pinson, M. Sicard, C. Masson, S. Nowak, P. Decorse, J. -Y. Piquemal, A. Galtayries, and C. Mangeney, *J. Phys. Chem. C* 2013, **117**, 26000-26006.
56 H. A. Miller, B. S. Kusel, S. T. Danielson, J. W. Neat, E. K. Avjian, S. N. Pierson, S. Budy, D. W. Ball, S. T. Iacono, and S. C. Kettwich, S. C. *J. Mater. Chem. A* 2013, **1**, 7050-7058.
57 B. J. Thomas, C. E. Bunker, E. A. Guliants, S. E. Hayes, A. Kheyfets, K. M. Wentz, S. W. Buckner, and P. A. Jelliss, *J. Nanopart. Res.* 2013, **15**, 1729.
58 D. A. Yagodnikov, and A. V. Voronetskii, *Combust. Explos. Shock Waves* 1997, **33**, 49-55.
59 E. Shafirovich, A. Mukasyan, L. Thiers, A. Varma, B. Legrand, C. Chauveau, and I. Gokalp, *Combust. Sci. Technol.* 2002, **174**, 125-140.
60 Y. -S. Kwon, A. A. Gromov, and J. I. Strokova, *Appl. Surf. Sci.* 2007, **253**, 5558-5564.
61 A. L. D. Kilcoyne, T. Tyliszczak, W. F. Steele, S. Fakra, P. Hitchcock, K. Franck, E. Anderson, B. Harteneck, E. G. Rightor, G. E. Mitchell, A. P. Hitchcock, L. Yang, T. Warwick, and H. Ade *J. Synchrotron Rad.* 2003, **10**, 125-136.
62 T. Tyliszczak, T. Warwick, A. L. D. Kilcoyne, S. Fakra, D. K. Shuh, T. H. Yoon, G. E. Brown, S. Andrews, V. Chembrolu, J. Strachan, and Y. Acremann, In *Synchrotron Radiation Instrumentation 2003, AIP Conference Proceedings* 2004; Vol. 705, p 1356-1359.
63 H. Bluhm, K. Andersson, T. Araki, K. Benzerara, G. E. Brown, J. J. Dynes, S. Ghosal, M. K. Gilles, H. C. Hansen, J. C. Hemminger, A. P. Hitchcock, G. Ketteler, A. L. D. Kilcoyne, E. Kneedler, J. R. Lawrence, G. G. Leppard, J. Majzlan, B. S. Mun, S. C. B. Myneni, A. Nilsson, H. Ogasawara, D. F. Ogletree, K. Pecher, M. Salmeron, D. K. Shuh, B. Tonner, T. Tyliszczak, T. Warwick, and T. H. Yoon, *J. Electron. Spectrosc. Relat. Phenom.* 2006, **150**, 86-104.
64 J. A. Haber, and W. E. Buhro, *J. Am. Chem. Soc.* 1998, **120**, 10847-10855.
65 I. N. Koprinarov, A. P. Hitchcock, C. T. McCrory, R. F. Childs, *J. Phys. Chem. B* 2002, **106**, 5358-5364.
66 K. Koski, J. Holsa, P. Juliet, *Thin Solid Films* 1999, **339**, 240-248.
67 F. R. Powell, P. W. Vedder, J. F Lindblom, and S. F. Powell, *Opt. Eng.* 1990, **29**, 614-624.
68 T. D. Fedotova, O. G. Glotov, V. E. Zarko, *Propell. Explos. Pyrot.* 2000, **25**, 325-332.
69 P. A. Jelliss, S. W. Buckner, S. W. Chung, A. Patel, E. A. Guliants, and C. E. Bunker, *Solid State Sci.* 2013, **23**, 8-12.

70 C. P. Balde, A. E. Mijovilovich, D. C. Koningsberger, A. M. J. van der Eerden, A. D. Smith, K. P. de Jong, and J. H. Bitter, *J. Phys. Chem. C* 2007, **111**, 11721-11725.
71 A. Leon, A. Balerna, G. Cinque, C. Frommen, and M. Fichtner, *J. Phys. Chem. C* 2007, **111**, 3795-3798.
72 J. J. Rehr, J. J. Kas, M. P. Prange, A. P. Sorini, Y. Takimoto, and F. Vila, F. A. *C R Phys.* 2009, **10**, 548-559.
73 J. J. Rehr, J. J. Kas, F. D. Vila, M. P. Prange, and K. Jorissen, *Phys. Chem. Chem. Phys.* 2010, **12**, 5503-5513.
74 T. Yamamoto, T. Kudo, T. Yamamoto, and J. Kawai, *Microporous Mesoporous Mater.* 2013, **182**, 239-243.
75 A. Benuzzi-Mounaix, F. Dorchies, V. Recoules, V. Festa, O. Peyrusse, A. Levy, A. Ravasio, T. Hall, M. Koenig, N. Amadou, E. Brambrink, and S. Mazevet, *Phys. Rev. Lett.* 2011, **107**, 165006.
76 O. Peyrusse, *High Energ. Dens. Phys.* 2010, **6**, 357-364.
77 K. Nakanishi, and T. Ohta, *J. Phys. Condens. Matter* 2009, **21**, 104214.
78 S. Mazevet, and G. Zerah, *Phys. Rev. Lett.* 2008, **101**, 155001.
79 F. Dorchies, M. Harmand, D. Descamps, C. Fourment, S. Hulin, S. Petit, O. Peyrusse, and J. J. Santos, *Appl. Phys. Lett.* 2008, **93**, 121113.
80 J. Wong, G. N. George, I. J. Pickering, Z. U. Rek, M. Rowen, T. Tanaka, G. H. Via, B. Devries, D. E. W. Vaughan, and G. E. Brown, *Solid State Commun.* 1994, **92**, 559-562.
81 A. Fontaine, P. Lagarde, D. Raoux, and J. M. Esteva, *J. Phys. F: Metal Phys.* 1979, **9**, 2143-2153.
82 T. A. Albright, J. K. Burdett, and M. Whangbo, *Orbital Interactions in Chemistry*, John Wiley and Sons, New York, 1985.
83 R. Hoffmann, *Solids and Surfaces: A Chemist's View of Bonding in Extended Structures*, Wiley-VCH, New York, 1988.
84 R. L. DeKock, H. B. Gray, *Chemical Structure and Bonding*, University Science Books, Sausalito, 1989.
85 J. J. Melko, A. W. Castleman, Jr., *Phys. Chem. Chem. Phys.* 2013, **15**, 3173-3178.
86 J. Stöhr, *NEXAFS Spectroscopy*, Springer-Verlag, New York, 2003.
87 L. R. Aramburo, Y. Liu, T. Tyliszczak, F. M. F. de Groot, J. C. Andrews, B. M. Weckhuysen, *Chemphyschem* 2013, **14**, 496-499.
88 P. Ildefonse, D. Cabaret, P. Sainctavit, G. Calas, A. M. Flank, and P. Lagarde, *Phys. Chem. Miner.* 1998, **25**, 112-121.
89 D. Cabaret, P. Sainctavit, P. Ildefonse, and A. M. Flank, *J. Phys. Condens. Matter* 1996, **8**, 3691-3704.
90 D. E. Li, G. M. Bancroft, M. E. Fleet, X. H. Feng, and Y. M. Pan, *Am. Mineral.* 1995, **80**, 432-440.
91 D. A. McKeown, *Phys. Chem. Miner.* 1989, **16**, 678-683.
92 B. N. Figgis, and M. A. Hitchman, *Ligand Field Theory and Its Applications*, Wiley-VCH, New York, 2000.
93 S. G. Minasian, J. M. Keith, E. R. Batista, K. S. Boland, S. A. Kozimor, R. L. Martin, D. K. Shuh, T. Tyliszczak, and L. J. Vernon, *J. Am. Chem. Soc.* 2013, **135**, 14731-14740.
94 D. Prendergast, and G. Galli, *Phys. Rev. Lett.* 2006, **96**, 215502.
95 A. H. England, A. M. Duffin, C. P. Schwartz, J. S. Uejio, D. Prendergast, and R. J. Saykally, *Chem. Phys. Lett.* 2011, **514**, 187-195.

96 C. D. Pemmaraju, R. Copping, S. Wang, M. Janousch, S. J. Teat, T. Tyliszcak, A. Canning, and D. K. Shuh, *Inorg. Chem.* 2014, **53**, 11415-11425.
97 P. Giannozzi, S. Baroni, N. Bonini, M. Calandra, R. Car, C. Cavazzoni, D. Ceresoli, G. L. Chiarotti, M. Cococcioni, I. Dabo, A. Dal Corso, S. de Gironcoli, S. Fabris, G. Fratesi, R. Gebauer, U. Gerstmann, C. Gougoussis, A. Kokalj, M. Lazzeri, L. Martin-Samos, N. Marzari, F. Mauri, R. Mazzarello, S. Paolini, A. Pasquarello, L. Paulatto, C. Sbraccia, S. Scandolo, G. Sclauzero, A. P. Seitsonen, A. Smogunov, P. Umari, and R. M. Wentzcovitch, *J. Phys. Condens. Matter*, 2009, **21**, 395502.
98 D. Vanderbilt, *Phys. Rev. B* 1990, **41**, 7892-7895.
99 D. Prendergast, S. G. Louie, *Phys. Rev. B* 2009, **80**, 235126.
100 K. Momma, and F. Izumi, *J. Appl. Crystallogr.* 2011, **44**, 1272-1276.

Chapter 3

X-ray spectroscopic and theoretical investigations of the role of the f-orbitals in mixing Al 3p character into the d-orbital conduction bands for lanthanide and actinide dialuminides

Overview

The properties of f-elements are known to be greatly modified upon alloying with aluminum. While these changes have vital implications for the safe handling of these materials for nuclear energy applications, the underlying causes remain obscured by the complicated behavior of the correlated f-electrons. The following chapter describes how the tools developed in Chapter 1 and Chapter 2 were used to collect, model and analyze X-ray absorption spectra of lanthanide (Ln) and actinide (An) dialuminides. Theory and spectroscopy suggested that there is significantly more covalency between the Al 3p orbitals and the Ln 5d in alloys containing divalent lanthanides compared with trivalent lanthanides, while the mixing between the Al 3p orbitals and An 6d orbitals falls in between. This work has recently been submitted for publication: A. B. Altman, C. D. Pemmaraju, S. Alayoglu, J. Arnold, E. D. Bauer, C. H. Booth, Z. Fisk, S. G. Minasian, J. I. Pacold, D. Prendergast, D. K. Shuh, T. Tyliszczak and J. Wang "Alternate roles of the f-orbitals in mixing Al 3p character into the d-orbital conduction bands for lanthanide and actinide dialuminides" *Submitted*. **2017.**

Introduction

Considerable progress has been made over the last several decades towards unraveling the complex electronic properties of correlated electron systems based on actinide elements. Many of these studies challenged the traditional viewpoint that actinide-based electrons are housed in core-like 5f orbitals such that magnetic properties arise solely from the spin and orbital angular momenta of the unpaired electrons.[1-8] For more than 60 years, lanthanide and actinide dialuminides ($LnAl_2$ and $AnAl_2$) have been employed as prototypical correlated electron systems because they all have the same cubic, Cu_2Mg structure. Although the $LnAl_2$ are generally ferromagnets (FM),[9] there are important exceptions. $CeAl_2$ is an antiferromagnet (AFM) with a complex magnetic structure derived from details of 4f band filling,[10] and shows quantum critical behavior resulting from 4f orbital hybridization with the 5d conduction band.[11,12] $EuAl_2$ and $YbAl_2$ are more overtly multiconfigurational;[13-15] for example, Yb in $YbAl_2$ is best described by an interaction of both Yb^{3+} ($4f^{13}$) and Yb^{2+} ($4f^{14}$) configurations.[16-18] Building on this simple intermediate valence scenario, optical conductivity[19,20] and magnetic susceptibility measurements[17,21-23] showed that coupling of the localized 4f electrons to the more delocalized 5d states impact the mechanisms of electrical conduction and quenching of magnetic moments. These observations supported a model in which close proximity of 4f bands to the Fermi energy perturbs the 5d conduction band, resulting in unusual Kondo and heavy fermion effects.[24-27] Of the known $AnAl_2$ analogs,[28] UAl_2 is a spin-fluctuation compound with a temperature scale of 15 K,[29] $NpAl_2$ is a FM below 56 K,[30] and $PuAl_2$ has complicated low temperature properties including an AFM transition at about 3.5 K.[31] In fact, over the short UAl_2, $NpAl_2$, and $PuAl_2$ portion of the series, these materials are excellent examples of the failure of the Hill criterion for describing magnetic ground states[32,33] since they have similar An–An distances (3.365 Å to 3.391 Å), yet very different magnetic ground states. The interplay between 5f and 6d orbitals and its impact on magnetism is still difficult to probe experimentally, and theoretical treatments for extended solids require demanding approaches to include relativistic and many-body effects while also accounting for partial electron delocalization and multiconfigurational ground states.[34]

Aluminum K-edge X-ray absorption spectroscopy (XAS) probes dipole-allowed transitions from the core Al 1s to final states with Al 3p character, and can be used to probe the

electronic structure of $LnAl_2$ and $AnAl_2$ and provide electronic structure insights that would be difficult or impossible to obtain using other techniques. Al K-edge XAS uses soft X-rays in the 1555 – 1570 eV range where edge features are easily resolved; spectral resolution is typically 0.2 eV for soft versus 1.0 eV or more for many hard X-ray measurements. This increased energy resolution provides rich spectral detail and an opportunity to move beyond valence formulations and to form interpretations within a band structure model. However, because the intermediate energy regime that includes the Al K-edge was historically difficult to access at many synchrotron facilities and beamlines, previous Al K-edge experiments were limited to studies of aluminum metal,[35,36] naturally-occurring oxides and minerals,[37] and a handful of synthetic materials.[38,39]

Our recent work on metallic aluminum[36,40] and molecular aluminum compounds[40] showed that accurate Al K-edge spectra could be measured in transmission mode using a scanning transmission X-ray microscope (STXM) and interpreted with the aid of hybrid density functional theory (DFT) calculations. This work describes our recent efforts to probe f and d states near the Fermi level of $LnAl_2$ and $AnAl_2$ alloys (Ln = Ce, Sm, Eu, Yb, Lu; An = U, Pu) using DFT calculations and Al K-edge XAS. The Al K-edge measurements and DFT calculations showed that interactions between the Al 3p and Ln 5d or An 6d states result in formation of new low energy bonding states in the conduction band. We propose an intuitive model to account for an indirect role for the 4f and 5f electrons in facilitating mixing of Al 3p character into the 5d and 6d conduction bands. An application of this model to rationalize well-known differences in magnetism for dialuminides is also discussed.

Results and Discussion

Figure 3.1 shows background subtracted and normalized Al K-edge XAS obtained in transmission mode using a scanning transmission X-ray microscope (STXM) for each of the dialuminides and for a 100 nm Al foil reference. Under the experimental conditions, the energy resolution was estimated at 0.2 eV (see Experimental Details). The spectra for each of the dialuminides and the aluminum reference foil were similar in that the onset of absorption intensity (first inflection point) occurred between 1558 and 1559 eV. Within this low-energy regime, the edge onset for the dialuminides was an additional 0.4 – 0.8 eV lower in energy than observed for the Al metal sample and well-resolved features were observed for $EuAl_2$, $YbAl_2$, and $LuAl_2$. To the best of our knowledge, the energy of the edge onsets for the dialuminides were lower than that observed for any other Al molecule or material. Moving to higher energies, one broad resonance was observed for all the dialuminides with energies that span a wide 1.5 eV energy range. Table 3.1 shows that the peak maxima occurred near the bottom of the energy range at 1564.8 and 1564.7 for $CeAl_2$ and $SmAl_2$, respectively, while the peak maxima for $YbAl_2$ and $PuAl_2$ were found at higher energies of 1565.9 and 1565.8 eV, respectively.

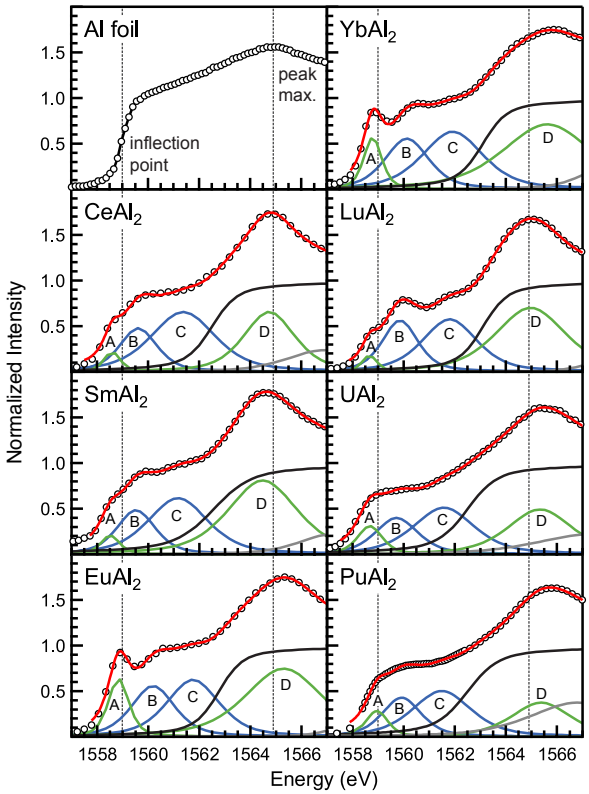

Figure 3.1. Al K-edge XAS (black circles) for MAl_2 (Ln = Ce, Sm, Eu, Yb, Lu, U, Pu) and Al metal, and pseudo-Voigt functions (green, blue, and gray) and step functions (black) used to generate the curve-fits (red). Vertical dashed black lines are positioned at the first inflection point (1559 eV) and first peak maximum (1564.9 eV) for Al metal to highlight changes in both the intensity of low-energy features and the energy of high energy transitions. The spectra of $YbAl_2$ and $LuAl_2$ were consistent with previously reported characterization using Bremsstrahlung isochromat spectroscopy (BIS) results.[41]

To accurately determine the energy and intensity of features observed in the Al K-edge XAS, the spectra were modeled using a combination of pseudo-Voigt line shapes, which were composed of a 1:1 ratio of Lorentzian to Gaussian functions, and a step function which was composed of a 1:1 ratio of error and arctangent functions (Table 3.1). To guide spectral interpretations, the Al K-edge XAS of $LuAl_2$ and $YbAl_2$ were calculated using an eXcited-electron Core Hole (XCH)-DFT approach because they were both reasonably well described by closed shell $4f^{14}$ electronic configurations (Figure 3.2). By freezing the 4f-occupancy to the $4f^{14}$ configuration, we avoided complications due to strong electron-electron correlations and considered the cases of closed-shell $YbAl_2$ and $LuAl_2$. Simulations were performed on a 2 x 2 x 2 supercell, and the calculated spectra were shifted along the energy axis by a constant to match the energies of the most intense feature around 1565 eV (see Experimental Details). Although the XCH-DFT calculation did not account for spin-orbit coupling or multiple-electron excited state configurations that are important in lanthanide spectroscopy, the calculated and experimental spectra showed excellent agreement with respect to both the relative energy and intensity of primary Al K-edge features. For example, both techniques showed a 2-3 fold decrease in intensity for the low energy feature in the Al K-edge spectrum of $YbAl_2$ (XAS: 0.6(1); XCH-DFT: 4.9×10^{-6}) on moving to $LuAl_2$ (XAS: 0.2(1); XCH-DFT: 1.7×10^{-6}).

Table 3.1. Energies and intensities of pseudo-Voigt functions used in the spectral deconvolutions.

	Energies (eV); Intensities (area)			
	A	B	C	D[a]
$CeAl_2$	1558.6; 0.2	1559.7; 1.1	1561.4; 2.5	1564.8
$SmAl_2$	1558.5; 0.2	1559.5; 1.1	1561.2; 2.2	1564.7
$EuAl_2$	1558.8; 0.8	1560.2; 1.5	1561.7; 1.7	1565.3
$YbAl_2$	1558.8; 0.6	1560.1; 1.5	1561.9; 2.4	1565.9
$LuAl_2$	1558.7; 0.2	1559.9; 1.2	1561.8; 2.0	1565.1
UAl_2	1558.7; 0.5	1559.7; 1.0	1561.6; 1.9	1565.5
$PuAl_2$	1559.0; 0.4	1559.9; 1.0	1561.5; 1.8	1565.8

[a] The position and intensity of this feature varied greatly with different curve-fitting models. Energy values were determined from a plot of the 1st derivative of the experimental spectrum.

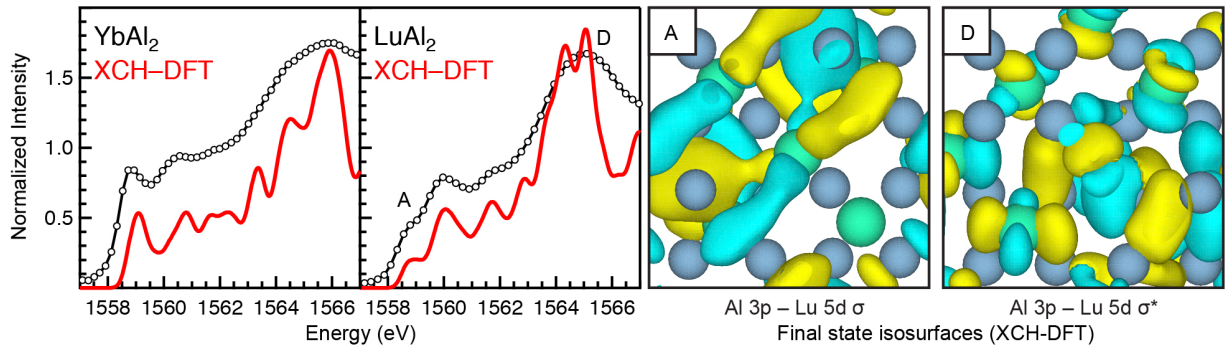

Figure 3.2. Left, experimental and XCH–DFT simulated Al K-edge spectra for $YbAl_2$ and $LuAl_2$. Right, two orbital isosurfaces for $LuAl_2$ (A and D) that represent transitions near the features labeled "A" and "D" in the computed spectrum for $LuAl_2$.

For additional detail, isosurface plots were generated to visualize the electronic final states associated with individual Al K-edge transitions in $LuAl_2$ (Figure 3.2). The band structure resulted in a large number of transitions for each unique value of k in the Brillouin zone, and interpretations were derived by isolating contributions to the band structure from the Γ point (0,0,0). Figure 3.2 shows two isosurfaces for $LuAl_2$ that were selected from transitions associated with the first low energy feature near 1558.7 eV and the broad feature at high energy near 1565.1 eV. The calculations supported an intuitive band structure model where low energy unoccupied states have bonding character and high energy states have antibonding character. Within the

bounds of this model, the first low energy features near 1558.7 eV were assigned to transitions involving directional, σ-type Al 3p – Ln 5d orbital bonding. At higher energy, the broad features observed at 1565.1 eV for $LuAl_2$ and at 1565.9 eV for $YbAl_2$ involved states derived from Al 3p and Ln 5d σ-antibonding. Isosurfaces associated with the features near 1560 eV (B and C in Figure 3.1) were comprised of a complex mixture of non-bonding or less-directional π-type interactions between 3p orbitals on adjacent Al atoms or with the 5d orbitals on the Yb and Lu atoms. For the remaining dialuminides, previous experience with several transition metal, lanthanide, and actinide compounds suggested that aspects of the simple electronic structure model described above for $YbAl_2$ and $LuAl_2$[42-44] could be extrapolated to assign analogous features for $CeAl_2$, $SmAl_2$, $EuAl_2$, UAl_2, and $PuAl_2$.

The XCH-DFT calculations also determined the theoretical density of states (DOS) in the presence of a core hole. Figure 3.3 shows that the occupied 4f states are just below E_F for $YbAl_2$, and 6 eV below E_F for $LuAl_2$. These excited state DOS results agreed with earlier optical conductivity measurements and ground state theoretical studies on $YbAl_2$ and $LuAl_2$ by Lee and coworkers, which provided evidence for 5d and 4p states above E_F with little 4f character.[20] For example, the Al 3p partial DOS for $YbAl_2$ indicated that the majority of the density up to 1 eV above E_F is associated with both Al 3p and Yb 5d states. A significant amount of Al 3p and Yb 5d density is also observed 7.5 eV above E_F. Like $YbAl_2$, the PDOS for $LuAl_2$ also exhibits considerable density in a high energy region 7 eV above E_F. However, the expansion in Figure 3.3 shows that there is considerably less Al 3p density 1 eV above E_F for $LuAl_2$ relative to $YbAl_2$.

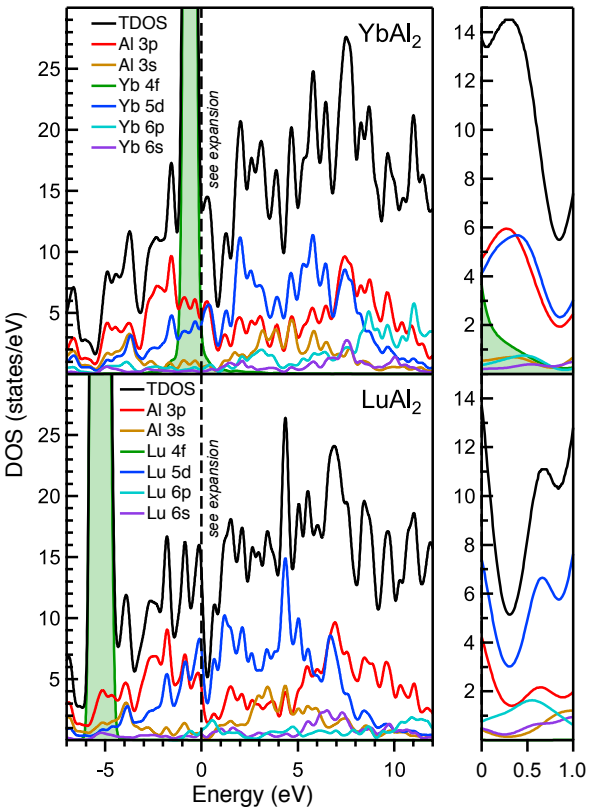

Figure 3.3. The calculated DOS for $YbAl_2$ and $LuAl_2$. Expansions of the 1 eV region above E_F are shown on the right to highlight the increase in Al 3p and Ln 5d character for $YbAl_2$ relative to $LuAl_2$.

Taken together, the experimental and theory results supported a consistent picture of electronic structure in $LnAl_2$ and $AnAl_2$ alloys that was used to quantify changes in the amount of Al 3p mixing with the Ln 5d and An 6d orbitals. As described above, the Al K-edge XAS and XCH-DFT simulations showed that intensities associated with low energy transitions change significantly (A in Figure 3.1), such that bonding interactions involving the Al 3p and Ln 5d or An 6d orbitals are greatest for $YbAl_2$ and $EuAl_2$, smallest for $CeAl_2$, $SmAl_2$, and $LuAl_2$, and intermediate for UAl_2 and $PuAl_2$. These changes also correlate with the destabilization of the Al 3p and Ln 5d or An 6d antibonding states, estimated from the position of the high-energy σ* resonances (D in Figure 3.1), which are roughly 0.5 to 1.0 eV higher in energy for $EuAl_2$, $YbAl_2$, UAl_2 and $PuAl_2$ relative to the other dialuminides (Table 3.1). The experimental and XCH-DFT calculated Al K-edge transition intensities and energies also agreed well with the increase in density of Al 3p and Yb 5d states at 1 eV above E_F for $YbAl_2$, and with the position of a maximum in the Al 3p and Yb 5d DOS at 7.5 eV for $YbAl_2$ compared with 7.0 eV for $LuAl_2$ (Figure 3.3).

The relationship between the Al K-edge XAS results and ground state electronic structure can be understood using a multi-electron configuration interaction (CI) model, which describes interactions between the Al 3p, Ln 5d or An 6d, and Ln 4f or An 5f orbitals in the ground state using the following expression:

$$\psi^* = N\left[a\left|f^n d^0 p^1\right\rangle + b\left|f^{n+1} d^0 p^0\right\rangle + c\left|f^n d^1 p^0\right\rangle + d\left|f^{n-1} d^1 p^1\right\rangle\right] \quad (3.1)$$

where N is the normalization constant and a, b, c, and d are mixing coefficients. The first configuration reflects no electron delocalization, such that n gives the f orbital occupancy for a Ln^{3+} or An^{4+} ion (e.g., f^{13} for Yb^{3+} and f^4 for Pu^{4+}). The second and third configurations reflect hybridization with the Al 3p states resulting in charge transfer to either the f or d orbitals. The fourth configuration accounts for f electron delocalization through mixing with the d states. If the electrons are predominantly localized, then the $f^n d^0 p^1$ configuration will have the largest contribution to the ground state electronic structure (large a in Equation 3.1), and the pre-edge region in the Al K-edge XAS will resemble Al metal. More divalent character in the ground state (large b in Equation 3.1) and enhanced mixing with the Al 3p and lanthanide 5d (large c in Equation 3.1) result in charge transfer from the Al 3p states. Concomitantly, the probability of Al 1s → 3p transitions increases and new Al K-edge features may be observed.

The relationship between the CI model and the Al K-edge XAS and theory results can be understood further by considering conclusions provided from several earlier experimental and theoretical examinations of the dialuminides. For example, calculations using the LDSA + U approach showed that – while most lanthanide dialuminides have FM ground states – $CeAl_2$ and $EuAl_2$ have AFM ground states and $YbAl_2$ is nonmagnetic.[27] Accordingly, $SmAl_2$ and $LuAl_2$ (both FMs) had weak low energy Al K-edge features, suggesting that the ground states are dominated by the configuration with localized 4f-electrons (large a in Equation 3.1). In contrast, the Al K-edge XAS of $EuAl_2$ and $YbAl_2$ exhibited intense features at low energy. These features indicated Ln 5d and Al 3p mixing resulting from increased divalent character (large b and c in Equation 3.1) and reflecting the lack of a magnetic moment for $YbAl_2$ and the AFM ground state for $EuAl_2$. $CeAl_2$ was the unique case, in that an AFM ground state had been calculated;[27] however, little evidence of Ce 5d and Al 3p mixing was obtained by Al K-edge XAS. Because the $4f^n$ states are higher in energy near the beginning of the lanthanide series, hybridization with the 5d states occurs readily in $CeAl_2$ without involving the Al 3p states (large d in Equation 3.1).

This alternate mechanism for electron delocalization explains how both $CeAl_2$ and $EuAl_2$ can have AFM ground states, while only $EuAl_2$ exhibited the enhancement in Al 3p and Ln 5d hybridization probed by Al K-edge XAS. In different terminology, $EuAl_2$ and $YbAl_2$ engage in Al 3p mixing with the $4f^{n+1}$ states, while $CeAl_2$ mixes in the $4f^{n-1}$ state by hybridizing with the 5d orbitals.

The periodic changes in Al 3p hybridization with the 5d or 6d conduction bands described above can also be rationalized by developing a simple theoretical framework based on molecular orbital theory (Figure 3.4). In first-order perturbation theory, orbital mixing (λ) for a hypothetical MAl_2 molecule (M = Ln or An) is described by

$$\lambda = S / (E^0_M - E^0_{Al}) \qquad (3.2)$$

where S is the spatial overlap between atomic orbitals and the term ($E^0_M - E^0_{Al}$) is their energy separation.[42,45] For $EuAl_2$ and $YbAl_2$, contributions from the divalent configuration (Ln^{2+}, $4f^{n+1}$) increase relative to the normal trivalent configuration (Ln^{3+}, $4f^n$). In addition to increasing the ionic radius, this decrease in charge of the lanthanide atom destabilizes the 5d states. These two effects result in both productive overlap (larger S) and a favorable energy match (small $E^0_M - E^0_{Al}$) with the high energy Al 3p states (-6.0 eV). Because the Al 3p states are not completely filled in Al metal, this mixing results in formation of new Al 3p – Ln 5d bonding states at lower energies, which are partially-filled and were sampled by Al K-edge XAS. For $CeAl_2$, $SmAl_2$, and $LuAl_2$, the increased contribution of the trivalent configuration stabilizes the 5d states and decreases ionic radii, resulting in both an energetic and spatial mismatch with the Al 3p states (large $E^0_M - E^0_{Al}$ and small S) and decreased M–Al mixing (λ).

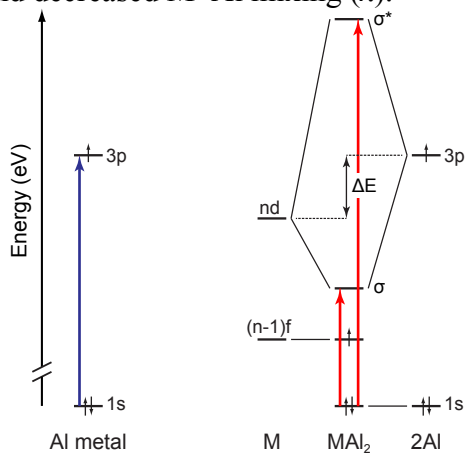

Figure 3.4. Qualitative orbital correlation diagrams depicting the formation of new σ-bonding states in dialuminides upon mixing with the Al 3p and Ln or An d orbitals. The new σ-bonding states are lower in energy than the first unoccupied states for pure Al metal. Decreases in oxidation state (Ln^{3+} to Ln^{2+}) or increases in principal quantum number n (5d to 6d) result in higher d orbital energies and enhanced mixing with the Al 3p orbitals for $EuAl_2$, $YbAl_2$, UAl_2, and $PuAl_2$ relative to $CeAl_2$, $SmAl_2$, and $LuAl_2$.

A similar model can be applied to UAl_2 and $PuAl_2$ where, to a first approximation, the ground-state electronic structure for U and Pu metals may be described by an interaction between two configurations, e.g., $5f^2$ and $5f^3$ for U^{4+} and U^{3+}, and $5f^5$ and $5f^6$ for Pu^{4+} and Pu^{3+},[46] respectively. The trends in lanthanide and actinide f → d promotion energies and ionization energies suggest that the $6d^1$ states for lanthanide and actinide ions have similar energies.[47-49] Thus, the increase in Al 3p and An 6d mixing reflected by the increased intensity of the pre-edge

region of the Al K-edge XAS may result from enhanced An–Al mixing due to an energetic match and from improved spatial overlap between the Al 3p and diffuse 6d atomic orbitals (small $E^0_M - E^0_{Al}$ and large S).

Conclusions

In summary, the combination of Al K-edge XAS and DFT results described herein provided new insights into longstanding questions about the nature of electron localization and bonding in f-electron systems, using $LnAl_2$ and $AnAl_2$ alloys as an example. Hybridization of the Al 3p and Ln 5d or An 6d orbitals results in formation of new bonding and antibonding states, both of which were probed directly by Al K-edge XAS. The results showed that changes in the energy and occupancy of the f-orbitals impact the energy of the Ln 5d and An 6d orbitals, and indirectly impact the amount of mixing with the Al 3p orbitals and the composition of the conduction band. Furthermore, trends in the amount of Al 3p and Ln 5d or An 6d mixing are influenced by changes in spatial overlap, which is strongly tied to the energetic stabilization due to orbital mixing.[42] These findings may have important implications for controlling bond energies, phase stabilities, and mechanical properties of actinide intermetallics by enhancing overlap with the diffuse 6d orbitals.

Experimental Details

Synthesis and characterization. Polycrystalline $LuAl_2$, UAl_2, and $PuAl_2$ materials were prepared by arc-melting the elements in stoichiometric amounts on a water-cooled copper hearth under an argon atmosphere with a Zr getter. $PuAl_2$ was wrapped in Ta foil, sealed in a silica tube under vacuum, and annealed at 600 °C for 3 days. X-ray diffraction measurements confirmed single-phase material for $LuAl_2$, UAl_2, and $PuAl_2$. Samples of $EuAl_2$ and $SmAl_2$ were prepared by induction melting stoichiometric amounts of the elements in sealed Ta tubes. About 0.8 g of $EuAl_2$ and 0.5 g of $SmAl_2$ were heated up to 1400 °C and 1520 °C, respectively, over about 15 minutes, then quenched rapidly (~ 200-300 °C/min.) by turning off the induction-melter. The temperature was measured using an optical pyrometer with an accuracy of +/- 50 °C. X-ray diffraction measurements revealed about 70% $EuAl_2$ and 30% $EuAl_4$ present in the as cast sample. The $EuAl_2$ as cast sample was wrapped in Ta foil, sealed in a silica tube under vacuum, and annealed at 1000 °C for 6 days to improve phase purity. The as cast $SmAl_2$ sample contained about 95% $SmAl_2$, along with 5% $SmAl_3$ and trace amounts of SmAl. No further heat treatment was performed on the $SmAl_2$ sample. Radiation damage can be significant at low temperatures for plutonium metal and intermetallics including $PuAl_2$, but previous research showed that self-annealing at room temperature repaired many defects.[50,51] To evaluate the possible effects of radiation damage in this study, measurements were reproduced on the same sample over multiple beam-runs spanning a range of approximately 10 years.

Al K-edge STXM-XAS Measurements. STXM-XAS methodology was similar to that previously described.[40,52] Samples were prepared by grinding crystals of the analyte into a fine powder with a mortar and pestle and brushing the powder onto a Si_3N_4 membrane (100 nm, Silson) or carbon support films (3-4 nm carbon, 10 nm formvar, Electron Microscopy Sciences) with a fiber, which arranged a large number of micron-sized particles in a compact area suitable for Al K-edge XAS. Radioactive samples were sealed between two membranes using Hardman Double/Bubble® 5-minute epoxy. Single energy images, elemental maps, Al K-edge and Sm and Eu $M_{5,4}$- edge spectra were acquired using STXM-XAS instruments at both the Molecular Environmental Science (MES) beamline 11.0.2 at the Advanced Light Source (ALS), which was

operated in topoff mode (500 mA), and the spectromicroscopy beamline 10ID-1 at the Canadian Light Source (CLS), which was operated in decay mode (250 to 150 mA). At both instruments, data were collected under a *ca*. 0.5 atm helium atmosphere. The beamlines used photons from elliptically polarizing undulators that delivered photons in the 130 to 2700 eV range (CLS)[53] and in the 100 to 2000 eV range (ALS)[54-56] to an entrance slit-less variable included angle plane-grating monochomator. Under normal conditions, variations in beamline energy calibration and performance between experimental periods would lead to significant differences in transition energies exceeding ± 0.3 eV. For these experiments, a primary set of single scans was collected for each sample in rapid succession during the same run, and standard deviation in transition energies of ± 0.2 eV was established. This primary set of scans was calibrated to the Al K-edge of a 1000 Å aluminum filter sample (Luxel, inflection point = 1559.0 eV). Additional spectra obtained from multiple particles and experimental runs were shifted accordingly to match the primary set, and then averaged to achieve the best possible data quality and signal to background ratio.

For all these measurements, the X-ray beam was focused with a zone plate onto the sample, and the transmitted light was detected. The spot size and spectral resolution were determined from characteristics of the 40 nm zone plate at ALS and 35 nm at CLS. Images at a single energy were obtained by raster-scanning the sample and collecting transmitted monochromatic light as a function of sample position (Figure 3.5). Spectra at particular regions of interest on the sample image were extracted from the "stack", a collection of images recorded at multiple, closely spaced photon energies across the absorption edge. Dwell times used to acquire an image at a single photon energy were 1 or 2 ms per pixel and spectra were obtained using horizontally polarized radiation. To quantify the absorbance signal, the measured transmitted intensity (I) was converted to optical density using the Beer−Lambert law: $OD = \ln(I/I_0) = \mu\rho d$, where I_0 is the incident photon flux intensity, d is the sample thickness, and μ and ρ are the mass absorption coefficients and density of the sample material, respectively. Incident beam intensity was measured through the particle-free region of the samples. Regions of particles with absorption of >1.5 OD were omitted. Because of the high density of MAl_2 alloys (4.9 to 8.3 g cm^{-3} for $CeAl_2$ and UAl_2, respectively), small sizes on the order of 0.25 to 1 μm^2 were typically required to ensure the spectra were in the linear regime of the Beer−Lambert law. Multiple spectra from different particles and beam runs were collected then averaged to improve data quality and signal to background ratio. In the case of the $PuAl_2$ sample, spectra were collected over multiple years to ensure radiation damage was not distorting the observed spectra.

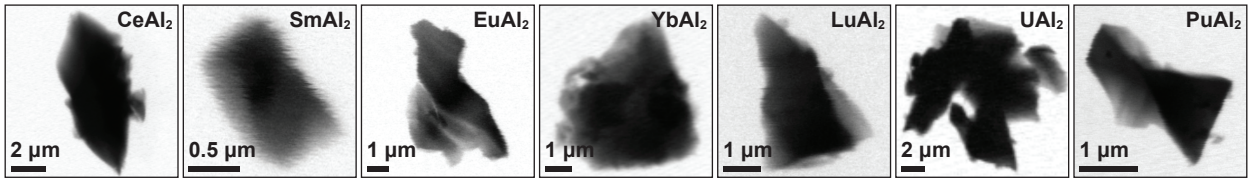

Figure 3.5. Normal contrast images obtained using STXM for crystalline particles of MAl_2 alloys. Small regions (*ca*. 0.25 to 1 μm^2) were selected for Al K-edge measurements.

Data Analysis. The Al K-edge data for $CeAl_2$, $EuAl_2$, UAl_2, and $PuAl_2$ were background subtracted and normalized using the MBACK algorithm in MATLAB.[57] For $SmAl_2$, $YbAl_2$, and $LuAl_2$, the Al K-edge spectra coincided with additional absorptions, including the Sm M_2-edge at 1547 eV, the Yb $M_{5,4}$-edges at 1519.8 and *ca.* 1576 eV, and the Lu M_5 edge at *ca.* 1600 eV. For

these datasets, a line was fit to the pre-edge region below 1556 eV for $YbAl_2$ and $LuAl_2$, and 1536 eV for $SmAl_2$, and then subtracted from the experimental data to eliminate the background of the spectrum. The data were normalized by fitting a first-order polynomial to the post-edge region of the spectrum, 1570–1588 eV for $LuAl_2$ and 1570-1700 for $SmAl_2$ and $YbAl_2$, and setting the edge jump at 1570 eV to an intensity of 1.0. In the case of $YbAl_2$, the data were normalized based on the $EuAl_2$ spectrum by scaling the data to match the intensity of the broad, intense feature near 1565 eV.

Fits for the pre-edge region of the Al K-edge data for the MAl_2 spectra were generated using the program IGOR 6.0 and a modified version of EDG_FIT.[58] The second derivatives of the spectra were used as guides for the number and position of pre-edge peaks, which were modeled using pseudo-Voigt line shapes consisting of an equal mixture of Gaussian and Lorentzian character in addition to a step function with a 1:1 ratio of arctangent and error function contributions that was used to model the rising edge. These analyses provided high-quality fits of the experimental data that were consistent between the systems as reflected by low-correlation coefficients, residual data that deviated slightly from zero, and symmetric residual peaks that matched well with the parent pseudo-Voigt functions. For each MAl_2 alloy, two pseudo-Voigt functions and a step function have been used to model the high energy peak and the post-edge. For $EuAl_2$, $YbAl_2$, and $LuAl_2$, three features were well-resolved in the low energy region below 1562 eV, and their energies and intensities were determined from the three corresponding curve-fit functions. For $CeAl_2$, $SmAl_2$, UAl_2, and $PuAl_2$, the first and second derivatives of the data and the curve-fitting analysis also indicated that three pseudo-Voigt functions were necessary to describe the region below 1562 eV. For $CeAl_2$, UAl_2 and $PuAl_2$, fully-unconstrained deconvolutions did not converge with step energy values that were consistent with the values generated by the fitting procedure for the other alloys. To obtain a consistent model, it was necessary to constrain the step function energy in these spectra to having an energy greater than or equal to 1562.5 eV. Spectral intensities and energies were determined from the position and area, respectively, of the corresponding curve-fit functions. Errors in the spectral intensities were estimated at 10% based on data reproducibility and observations from earlier STXM-XAS studies.[42,52] For all the spectra, uncertainty in the transition energies was estimated at ± 0.2 eV for back-to-back measurements made during the same experimental campaign at the light sources. Due to the close proximity to each other and to the rising edge, some functions used to model higher energy features were affected by subtle changes in the curve-fitting model and an error of ± 0.5 eV was assigned. The area under the pre-edge peaks (defined as the intensity) was calculated with the formula $\text{ph} \times \text{fwhm} \times {}^1\!/_4 \times \{ [\pi / ln(2)]^{1/2} + \pi \}$, where ph = peak height (normalized intensity), fwhm = full-width at half maximum height (eV), and the value ${}^1\!/_4 \times \{ [\pi / ln(2)]^{1/2} + \pi \} \approx 1.318$ is a constant associated with the pseudo-Voigt function.

Al K-edge Spectral Simulations. XAS spectra at the Al K-edge were simulated using the so called eXcited-electron Core-Hole XCH approach,[59] which was described in detail elsewhere.[59-61] Briefly, within the XCH approach, the lowest energy excited state of the system was modeled within an occupation-constrained DFT framework employing a periodic supercell formalism. This was done by describing the core-excited atom within the supercell through a core−hole pseudopotential and taking into account the screening due to the excited electron self-consistently. Higher lying X-ray excited-state energies were then approximated through eigenvalue differences obtained from the Kohn−Sham (KS) spectrum of the lowest energy core-excited state. X-ray transition matrix elements were calculated using Fermi's golden rule and

typically for light-element K-edges, employing the dipole approximation. The numerical implementation of the XCH method utilized in this study was based on a development version of the Quantum-Espresso package[62] that provided a plane-wave pseudopotential DFT framework for electronic structure calculations. Ultrasoft pseudopotentials[63] with the following valence electronic configurations Al: $[Ne]3s^2 3p^1$, Yb: [Xe] $6s^2 4f^{14}$, Lu: [Xe] $6s^2 5d^1 4f^{14}$, were used together with a plane-wave energy cutoff of 50 Ry. To describe 1s core-excited Al in XANES simulations, a core-hole pseudopotential with the electronic configuration $1s^1 2s^2 2p^6 3s^2 3p^2$ was generated. The DFT calculations employed the Perdew-Burke-Ernzerhof Generalized-Gradient Approximation[64] to describe exchange-correlation effects. XCH simulations of MAl_2 dialuminides employed $2 \times 2 \times 2$ supercells of the $MgCu_2$ type structure consisting of 192 atoms. Owing to the large size of supercells, the Brillouin zone was sampled through a 2 x 2 x 2 Γ-centered k-point grid during the Kohn-Sham self-consistent field calculation, but the band structure was interpolated over a uniform Γ-centered $3 \times 3 \times 3$ k-point grid using the Shirley interpolation scheme[65] in order to generate XAS spectra. The XCH spectra were shifted rigidly by 1560.65 eV and the intensities scaled uniformly by 1.2×10^6 to facilitate comparison with experiment. A 4 x 4 x 4 grid was used to generate the densities of states.

XCH final state electronic wave functions corresponding to core- excitations into the virtual orbital manifold were approximated by unoccupied KS wave functions obtained from the self-consistent occupation-constrained DFT calculation including the core-hole. Orbital isosurfaces were visualized using VESTA-3.[66]

References

1 S. S. Hecker, *Metall. Mater. Trans. A*, 2004, **35A**, 2207-2222.
2 K. T. Moore and G. van der Laan, *Rev. Mod. Phys.*, 2009, **81**, 235-298.
3 J. L. Sarrao, L. A. Morales, J. D. Thompson, B. L. Scott, G. R. Stewart, F. Wastin, J. Rebizant, P. Boulet, E. Colineau, and G. H. Lander, *Nature*, 2002, **420**, 297-299.
4 G. R. Stewart, *Rev. Mod. Phys.*, 1984, **56**, 755-787.
5 G. H. Lander, E. S. Fisher, and S. D. Bader, *Adv. Phys.*, 1994, **43**, 1-111.
6 S. L. Dudarev, D. N. Manh, and A. P. Sutton, Philos. *Mag. B*, 1997, **75**, 613-628.
7 D. J. Scalapino, Rev. *Mod. Phys.*, 2012, **84**, 1383-1417.
8 E. D. Bauer and J. D. Thompson, in *Annual Review of Condensed Matter Physics*, ed. J. S. Langer, 2015, vol. 6, pp. 137-153.
9 H. G. Purwins and A. Leson, *Adv. Phys.*, 1990, **39**, 309-403.
10 K. Kang and M. Lee, *Curr. Appl. Phys.*, 2014, **14**, 383-388.
11 K. Buschow, *Rep. Prog. Phys.*, 1979, **42**, 1373-1477.
12 F. Steglich, *Physica C*, 2007, **460**, 7-12.
13 B. A. Rao, P. Kistaiah, and K. S. Murthy, *Mater. Lett.*,1990, **9**, 410-412.
14 B. A. Rao, P. Kistaiah, and K. S. Murthy, *Phys. Status Solidi A*, 1994, **144**, K1-K3.
15 C. Dallera, E. Annese, J. P. Rueff, A. Palenzona, G. Vanko, L. Braicovich, A. Shukla, and M. Grioni, *Phys. Rev. B*, 2003, **68**, 245114.
16 K. A. Gschneidner, J. *Less-Common Met.*, 1969, **17**, 13-24.
17 E. E. Havinga, K. Buschow, and H. J. Van Daal, *Solid State Commun.*, 1973, **13**, 621-627.
18 F. Merlo, *Thermochim. Acta*, 1983, **64**, 115-122.
19 R. J. Lange, S. J. Lee, K. J. Kim, P. C. Canfield, and D. W. Lynch, *Phys. Rev. B*, 2000, **63**, 035105.
20 S. J. Lee, S. Y. Hong, I. R. Fisher, P. C. Canfield, and B. N. Harmon, *Phys. Rev. B*, 2000, **61**, 10076-10083.
21 J. Klaasse and J. Sterkenburg, *Solid State Commun.*, 1973, **12**, 561-564.
22 A. Iandelli and A. Palenzona, *J. Less-Common Met.*, 1972, **29**, 293-297.
23 H. Wada and M. Shiga, *Physica B*, 1994, **193**, 25-30.
24 T. Jarlborg, A. J. Freeman, and D. D. Koelling, *J. Magn. Magn. Mater.*, 1986, **60**, 291-305.
25 D. Paudyal, A. K. Pathak, V. K. Pecharsky, and K. A. Gschneidner, Jr., *J. Phys. Condens. Matter*, 2013, **25**, 396002.
26 A. K. Pathak, D. Paudyal, K. A. Gschneidner, Jr., and V. K. Pecharsky, *J. Appl. Phys.*, 2014, **115**, 17E109.
27 D. Paudyal, V. K. Pecharsky, and K. A. Gschneidner, Jr., *J. Appl. Phys.*, 2014 **115**, 17E127.
28 A. M. Boring, R. C. Albers, G. R. Stewart, and D. D. Koelling, *Phys. Rev. B*, 1985, **31**, 3251-3259.
29 R. J. Trainor, M. B. Brodsky, and H. V. Culbert, *Phys. Rev. Lett.*, 1975, **34**, 1019-1022.
30 A. T. Aldred, B. D. Dunlap, D. J. Lam, and I. Nowik, *Phys. Rev. B*, 1974, **10**, 1011-1019.
31 G. R. Stewart and R. O. Elliott, *Phys. Rev. B*, 1985, **31**, 4669-4671.
32 H. H. Hill, in *Plutonium 1970 and Other Actinides*, ed. W. N. Miner, AIME, New York, 1970.

33 J. L. Smith and Z. Fisk, *J. Appl. Phys.*, 1982, **53**, 7883-7886.
34 J. M. Wills and O. Erickson, *Los Alamos Sci.*, 2000, **26**, 128-151.
35 A. Benuzzi-Mounaix, F. Dorchies, V. Recoules, F. Festa, O. Peyrusse, A. Levy, A. Ravasio, T. Hall, M. Koenig, N. Amadou, E. Brambrink, and S. Mazevet, *Phys. Rev. Lett.*, 2011, **107**, 165006.
36 A. B. Altman, C. D. Pemmaraju, S. Alayoglu, J. Arnold, C. H. Booth, A. Braun, C. E. Bunker, A. Herve, S. G. Minasian, D. Prendergast, D. K. Shuh, and T. Tyliszczak, *Inorg. Chem.*, 2017, **56**, 5710-5719.
37 P. Ildefonse, D. Cabaret, P. Sainctavit, G. Calas, A. M. Flank, and P. Lagarde, *Phys. Chem. Miner.*, 1998, **25**, 112-121.
38 H. E. van der Bij, D. Cicmil, J. Wang, F. Meirer, F. M. F. de Groot, and B. M. Weckhuysen, *J. Am. Chem. Soc.*, 2014, **136**, 17774-17787.
39 L. R. Aramburo, Y. Liu, T. Tyliszczak, F. M. F. de Groot, J. C. Andrews, and B. M. Weckhuysen, *Chemphyschem*, 2013, **14**, 496-499.
40 A. B. Altman, C. D. Pemmaraju, C. Camp, J. Arnold, S. G. Minasian, D. Prendergast, D. K. Shuh, and T. Tyliszczak, *J. Am. Chem. Soc.*, 2015, **137**, 10304-10316.
41 S. J. Oh, J. W. Allen, M. S. Torikachvili, and M. B. Maple, *J. Magn. Magn. Mater.*, 1985, **52**, 183-186.
42 S. G. Minasian, J. M. Kieth, E. R. Batista, K. S. Boland, C. N. Christensen, D. L. Clark, S. D. Conradson, S. A. Kozimor, R. L. Martin, D. E. Schwarz, D. K. Shuh, G. L. Wagner, M. P. Wilkerson, L. E. Wolfsberg, and P. Yang, *J. Am. Chem. Soc.*, 2012, **134**, 5586-5597.
43 S. G. Minasian, J. M. Keith, E. R. Batista, K. S. Boland, S. A. Kozimor, R. L. Martin, D. K. Shuh, T. Tyliszczak, and L. J. Vernon, *J. Am. Chem. Soc.*, 2013, **135**, 14731-14740.
44 S. G. Minasian, J. M. Keith, E. R. Batista, K. S. Boland, D. L. Clark, S. A. Kozimor, R. L. Martin, D. K. Shuh, and T. Tyliszczak, *Chem. Sci.*, 2014, **5**, 351-359.
45 I. D. Prodan, G. E. Scuseria, and R. L. Martin, *Phys. Rev. B*, 2007, **76**, 033101.
46 C. H. Booth, Y. Jiang, D. L. Wang, J. N. Mitchell, P. H. Tobash, E. D. Bauer, M. A. Wall, P. G. Allen, D. Sokaras, D. Nordlund, T. C. Weng, M. A. Torrez, and J. L. Sarrao, *PNAS*, 2012, **109**, 10205-10209.
47 L. Brewer, *J. Opt. Soc. Am*, 1971, **61**, 1666-1682.
48 W. C. Martin, R. Zalubas, and L. Hagan *Atomic Energy Levels – The Rare Earth Elements*, NSRDS-NBS 60 (U.S. Department of Commerce: Washington, DC, 1978).
49 X. Y. Cao and M. Dolg, *J. Mol. Struct.*, 2004, **673**, 203-209.
50 A. J. Arko, F. Y. Fradin, and M. B. Brodsky, *Phys. Rev. B*, 1973, **8**, 4104-4118.
51 C. H. Booth, Y. Jiang, S. A. Medling, D. L. Wang, A. L. Costello, D. S. Schwartz, J. N. Mitchell, P. H. Tobash, E. D. Bauer, S. K. McCall, M. A. Wall, and P. G. Allen, *J. Appl. Phys.*, 2013, **113**, 093502-093511.
52 S. G. Minasian, J. M. Keith, E. R. Batista, K. S. Boland, J. A. Bradley, S. R. Daly, D. Sokaras, S. A. Kozimor, W. W. Lukens, R. L. Martin, D. Nordlund, G. T. Seidler, D. K. Shuh, T. Tyliszczak, G. L. Wagner, T. C. Weng, and P. Yang, *J. Am. Chem. Soc.*, 2013, **135**, 1864-1871.
53 K. V. Kaznatcheev, C. Karunakaran, U. D. Lanke, S. G. Urquhart, M. Obst, and A. P. Hitchcock, *Nucl. Instr. Meth. Phys. Res.*, 2007, **582**, 96-99.
54 H. Bluhm, K. Andersson, T. Araki, K. Benzerara, G. E. Brown, J. J. Dynes, S. Ghosal, M. K. Gilles, H. C. Hansen, J. C. Hemminger, A. P. Hitchcock, G. Ketteler, A. L. D.

Kilcoyne, E. Kneedler, J. R. Lawrence, G. G. Leppard, J. Majzlan, B. S. Mun, S. C. B. Myneni, A. Nilsson, H. Ogasawara, D. F. Ogletree, K. Pecher, M. Salmeron, D. K. Shuh, B. Tonner, T. Tyliszczak, T. Warwick, and T. H. Yoon, *J. Electron. Spectrosc. Relat. Phenom.*, 2006, **150**, 86-104.

55 A. L. D. Kilcoyne, T. Tyliszczak, W. F. Steele, S. Fakra, P. Hitchcock, K. Franck, E. Anderson, B. Harteneck, E. G. Rightor, G. E. Mitchell, A. P. Hitchcock, L. Yang, T. Warwick, and H. Ade, *J. Synchrotron Rad.*, 2003, **10**, 125-136.

56 H. J. Nilsson, T. Tyliszczak, R. E. Wilson, L. Werme, and D. K. Shuh, *Anal. Bioanal. Chem.*, 2005, **383**, 41-47.

57 T. C. Weng, G. S. Waldo, and J. E. Penner-Hahn, *J. Synchrotron Rad.*, 2005, **12**, 506-510.

58 G. N. George, EDG_FIT, Stanford, CA.

59 D. Prendergast and G. Galli, *Phys. Rev. Lett.*, 2006, **96**, 215502.

60 A. H. England, A. M. Duffin, C. P. Schwartz, J. S. Uejio, D. Prendergast, and R. J. Saykally, *Chem. Phys. Lett.*, 2011, **514**, 187-195.

61 C. D. Pemmaraju, R. Copping, S. Wang, M. Janousch, S. J. Teat, T. Tyliszcak, A. Canning, D. K. Shuh, and D. Prendergast, *Inorg. Chem.*, 2014, **53**, 11415-11425.

62 P. Giannozzi, S. Baroni, N. Bonini, M. Calandra, R. Car, C. Cavazzoni, D. Ceresoli, G. L. Chiarotti, M. Cococcioni, I. Dabo, A. Dal Corso, S. de Gironcoli, S. Fabris, G. Fratesi, R. Gebauer, U. Gerstmann, C. Gougoussis, A. Kokalj, M. Lazzeri, L. Martin-Samos, N. Marzari, F. Mauri, R. Mazzarello, S. Paolini, A. Pasquarello, L. Paulatto, C. Sbraccia, S. Scandolo, G. Sclauzero, A. P. Seitsonen, A. Smogunov, P. Umari, and R. M. Wentzcovitch, *J. Phys. Condens. Matter*, 2009, **21**, 395502.

63 D. Vanderbilt, *Phys. Rev. B*, 1990, **41**, 7892-7895.

64 J. P. Perdew, K. Burke, and M. Ernzerhof, *Phys. Rev. Lett.* 1996, **77**, 3865-3868.

65 D. Prendergast, and S. G. Louie, *Phys. Rev. B: Condens. Matter Mater. Phys.* 2009, **80**, 235126.

66 K. Momma, and F. Izumi, *J. Appl. Crystallogr.* 2011, **44**, 1272-1276.

Chapter 4

Hydride oxidation from a titanium–aluminum bimetallic complex: insertion, thermal and electrochemical reactivity

Overview

The following chapter describes the synthesis and characterization of titanium aluminum bimetallics containing a Ti-μH-Al motif. Titanium aluminum molecules and materials are of importance for applications ranging from catalysis (Ziegler Natta alkene polymerization) to hydrogen storage (doping of aluminum hydride materials with titanium has been shown to promote hydrogen evolution reversibility). Additionally, titanium chemistry can serve as a model and reference for heavier Group IV metals and thorium behavior. Based on the spectroscopic results described in Chapter 1, bimetallics containing bridging hydrides were pursued in order to facilitate metal reduction and hydride activation. It was found that an alanate ligand stabilized a low-valent Ti(III) bimetallic, which underwent reductive elimination of hydrogen upon exposure to oxidizing reagents. This work resulted from a close collaboration with undergraduate student, Alexandra C. Brown, and has recently been published in: A.C. Brown, A.B. Altman, A.B., T.D. Lohrey, S. Hohloch, J. Arnold "Hydride oxidation from a titanium-aluminum bimetallic complex: insertion, thermal and electrochemical reactivity." *Chem. Sci.* 2017, **8**, 5153-5160.

Introduction

Aluminum hydrides are important for a wide range of applications, from organic synthesis to hydrogen storage.[1–7] These species are often poorly defined extended solids with a variety of phase mixtures and defects.[8,9] This complexity obscures the mechanistic details of the varied transformations these materials mediate. In contrast, molecular systems offer well-defined metal sites that allow for in-depth study of the reactivity of aluminum-hydride bonds. Recent synthetic work[10–12] and a spectroscopic study[13] provide evidence that specific ligand frameworks support reductive elimination of aluminum hydrides under mild conditions to yield aluminum (I) compounds. We were interested in exploring the relevance of this chemistry to titanium-aluminum bimetallics, as aluminum materials doped with titanium are used for hydrogen storage, and the redox processes behind the repeated storage and discharge of hydrogen from such materials remain not well understood.[14–20]

Previous work by Wilkinson and coworkers,[21–24] Bulychev and coworkers,[25–36] Stephan and coworkers,[37,38] and Tebbe and coworkers[39,40] found that the reaction of transition metal halides and $LiAlH_4$ formed multimetallic structures containing the TM-μH-Al motif (Figure 4.1). Bulychev and coworkers[25–34] were able to synthesize a variety of titanium-aluminum heterometallics. They explored stoichiometric protonolysis reactivity to form alkoxide and amide complexes[32,33] and showed the promise of these titanium-aluminum hydrides, alkoxides, amides and halides for the catalytic hydrogenation and isomerization of olefins.[26,27,29,33,34]

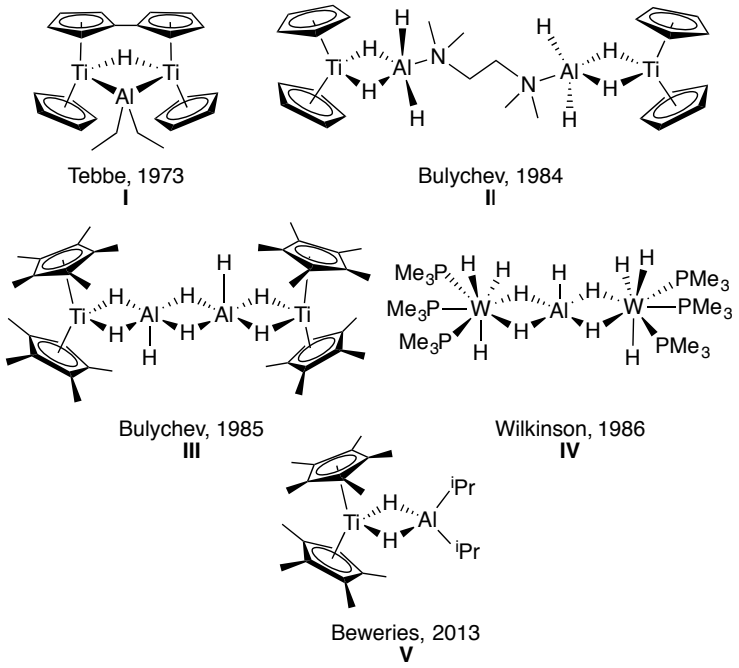

Figure 4.1. Previously synthesized transition metal aluminum hydride heterometallics **I**,[39] **II**[31], **III**[29], **IV**[22] and **V**[41] showing the various motifs that have been isolated.

As outlined in the recent comprehensive review by Crimmin and coworkers,[42] while the structural parameters, protonolysis, and olefin reactivity of aluminum hydride heterobimetallics are well established, opportunities remain to develop other classes of reactions. To this end, there have been recent reports of *in situ* generated titanium aluminum bimetallics for catalytic dehydrogenation of hydrazine borane (**V**)[41] and catalytic hydroalumination of alkynes.[43]

These species offer promising new avenues in catalysis, and to better understand the breadth and opportunities in titanium-aluminum bimetallic reactivity, it is necessary to conduct detailed study of isolated heterobimetallics under a variety of conditions. To form these discrete bimetallics, with thermal stability and potential redox activity, we employed a bulky alanate stabilized by a tris(trimethylsilyl)methyl ligand. This is the only ligand known to support an aluminum(III) alanate as well as a low-valent aluminum(I) species; such redox activity is required for the reversible storage of dihydrogen.[44–51] Here, we report that a titanium(III)-aluminum bimetallic complex incorporating this ligand was found to be indefinitely stable at room temperature under inert atmosphere, but the bridging hydrides were readily oxidized. Utilizing this bimetallic, we further investigated thermal hydrogen evolution and developed of new classes of reactivity for titanium-aluminum hydrides: reduction of heteroallenes and reductive elimination of dihydrogen upon electrochemical oxidation.

Results and Discussion

The reaction of Cp_2TiCl with $KH_3AlC(SiMe_3)_3$ (**4.1**) in 1:1 ratios generated the paramagnetic bimetallic compound $Cp_2Ti(\mu\text{-}H)_2(H)AlC(SiMe_3)_3$ (**4.2**) *via* salt metathesis. Upon addition of **1** to Cp_2TiCl in diethyl ether, there was an instantaneous color change from green to purple. The ^1H NMR spectrum of the crude material revealed two broad resonances at 0.35 ppm and 0.33 ppm; the relative intensities were found to be dependent on the initial ratios of **4.1** to Cp_2TiCl. While these complexes are paramagnetic, the presence of a broad resonance between 0.3

and 0.5 ppm was diagnostic of the -C($SiMe_3$)$_3$ protons. Through optimization of synthetic procedures, we found that compound **4.2** could be formed selectively by reaction of Cp_2TiCl with **4.1** in a 1:2 ratio in 83% yield, while $(Cp_2Ti)_2(\mu\text{-}H)_3(H)AlC(SiMe_3)_3$ (**4.3**) could be formed from a 2:1 ratio of Cp_2TiCl with **4.1** in 32% yield (Scheme 4.1).

Crystallographic characterization of **4.2** and **4.3** (Figure 4.2) confirmed formation of two heterometallic complexes incorporating a Ti(III)-μH-AlH motif. The bimetallic **4.2** contains one titanium (III) atom and one aluminum atom at a distance of 2.7773(8) Å. This separation is very similar to those reported by Bulychev (2.788 Å[31], 2.750(3) Å[29]) and while it is less than the sum of the covalent radii[52] (2.81(9) Å), there is no further indication of metal-metal bonding. In comparison, the trimetallic **4.3** contains two titanium (III) atoms and one aluminum atom as part of a six-membered ring, with the metals bridged by hydrides. The Ti-Al separations (3.286(2) and 3.264(2) Å) and the Ti-Ti separation (3.761(1) Å) are within the sum of the van der Waals radii[53] (Ti/Al: 4.25 Å, Ti/Ti: 4.30 Å), but the metals are much farther apart than in **4.2** and any metal-metal interaction, if present, must be much weaker. The paramagnetism of **4.2** and **4.3** was confirmed using the Evans NMR method;[54,55] after diamagnetic correction[56,57] the magnetic moment of **4.2** was observed to be 1.70(2) μ_B (calculated spin-only moment: 1.73 μ_B), while the magnetic moment of the $[Ti(III)]_2$ unit in **4.3** was observed to be 1.66(2) μ_B (calculated spin-only moment for two independent d^1 Ti(III) centers: 2.83 μ_B) indicative of antiferromagnetic coupling between the two Ti(III) centers.

We investigated the behavior of **4.2** in solution, with the hypothesis that **4.2** might dissociate into $[Cp_2TiH]$ and $H_2AlC(SiMe_3)_3$ since evidence of such dissociation was reported in related zirconium systems.[58–60] However, Cp_2TiH is known to be extremely unstable in solution at room temperature.[61] If the bimetallic were in equilibrium with its dissociated monometallic components, that decomposition of transiently formed Cp_2TiH was expected to drive the dissociation equilibrium towards full decomposition of **4.2**. The observed stability of **4.2** and **4.3** indicated that the solid-state structures were representative of the species present in solution.

Though **4.2** and **4.3** were stable in solution, they interconverted upon addition of additional reagents. Compound **4.2** slowly converted to **4.3** upon addition of KH and **4.3** could be converted to **4.2** by the addition of **4.1** (Scheme 4.1). This explained the optimized stoichiometry; when a 2-fold excess of **4.1** was used, any **4.3** formed transiently was converted to **4.2**. Use of only ½ equivalent of **4.1** favored the formation of **4.3** over **4.2**, but the yield of **4.3** was limited because **4.1** also serves as a source of hydrides in this reaction. While alane products were predicted stoichiometrically, no aluminum byproducts were isolated from these reactions.

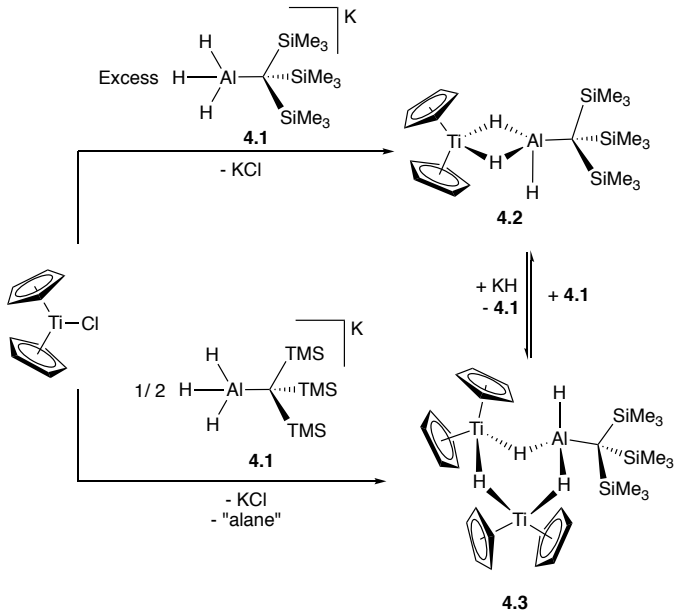

Scheme 4.1. Formation and interconversion of bimetallic **4.2** and trimetallic **4.3**.

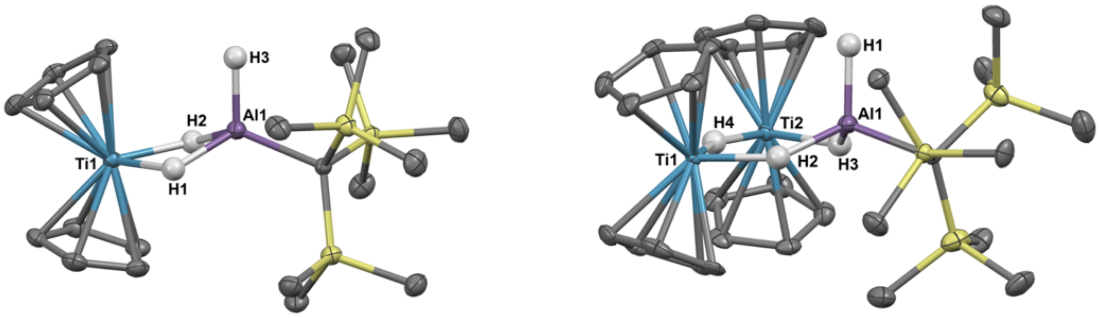

Figure 4.2. Crystallographically determined structures of **4.2** (left) and **4.3** (right). Thermal ellipsoids are shown at the 50% probability level. C-H hydrogens are omitted for clarity. Metal hydrides were located in the Fourier difference map and their positions were refined. Ti(1)-Al(1) distance in **4.2**: 2.7773(8) Å. Metal-metal distances in **4.3:** Ti(1)-Al(1): 3.286(2) Å, Ti(2)-Al(1): 3.264(2) Å, Ti(1)-Ti(2): 3.761(1) Å.

Insertion Reactivity

With a high-yielding synthesis of a titanium-aluminum bimetallic, we had the opportunity to pursue novel reactivity. Addition of 1 atm of CO_2 to **4.2** in solution resulted in a color change from purple to teal. While the FTIR spectrum of the crude product contained a formate stretch, no pure crystalline material could be isolated. We then turned to the reduction of other heteroallenes as analogues to CO_2, where we met more success.

Reaction of **4.2** with an excess of diisopropylcarbodiimide led to the isolation of deep blue crystals of $Cp_2Ti(\mu\text{-}H)(\mu\text{-}(iPr)N(CH)N(iPr))(H)AlC(SiMe_3)_3$ (**4.4**) (Scheme 4.2). Compound **4.4** was characterized crystallographically, and features an anionic formamidinate trapped between titanium and aluminum centers that are 3.300(1) Å apart (Figure 4.3). The formamidinate is asymmetric (1.298(2) Å (N1-C14) and 1.331(2) Å (N2-C14)), which suggests that the anionic

charge of the formamidinate is localized towards the aluminum center. Notably, use of one equivalent of carbodiimide gave incomplete conversion to **4.4**, while use of a large excess did not result in further reactivity. Similar insertions were found to be possible with other carbodiimides of comparable steric bulk such as di(p-tolyl)carbodiimide.

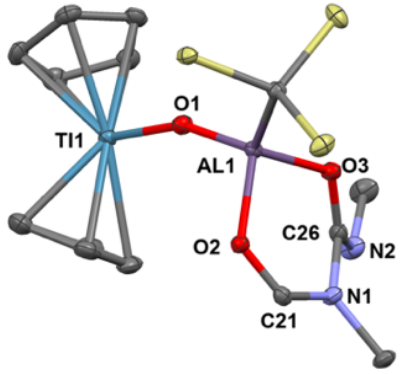

Figure 4.3. Crystallographically determined structure of **4.4**. Thermal ellipsoids are shown at the 50% probability level. Metal hydrides were located in the Fourier difference map and their positions were refined. C-H hydrogen atoms are omitted for clarity. Relevant distances and bond lengths: Ti(1)-Al(1) 3.300(1) Å, N(1)-C(14): 1.298(2) Å, N(2)-C(14): 1.331(2) Å, Ti(1)-N(1): 2.161(1) Å, Al(1)-N(2) 1.892(1) Å.

To investigate if modulating the steric properties of the heteroallene could result in activation of multiple hydrides in the bimetallic, the reactivity of **4.2** with isocyanates was studied. Addition of three equivalents of tert-butylisocyanate to **4.2** in hexane led to the precipitation of a bright green solid, which was crystallographically determined to be $Cp_2Ti(\mu\text{-}O)Al(OCHN^tBuC(N^tBuO)(C(SiMe_3)_3)$ (**4.5**) (Scheme 4.2). No products could be isolated using fewer equivalents of isocyanate.

Complex **4.5** features a bridging titanium-aluminum oxo moiety in addition to a six-membered ring containing the aluminum center and two coupled isocyanates (Figure 4.4). Such isocyanate insertion products are uncommon: a related example was recently reported with a boron-based Lewis acid.[62] Despite isocyanate being a weak oxidizing agent, the product retains the Ti(III) center; one hydride reduced the backbone carbon and two hydrides were transferred to an isocyanate fragment which was presumably the source of the oxo moiety, however no other products could be identified. Bulky isocyanates such as bis(2,6-diisopropylphenyl)isocyanate did not lead to isolable products.

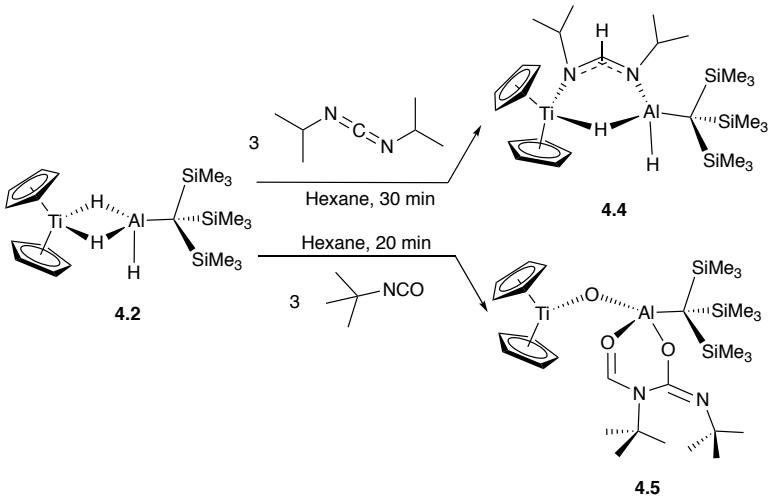

Scheme 4.2. Organic substrate reduction reactivity of **4.2** with diisoproylcarbodiimide and *tert*-butyl isocyanate.

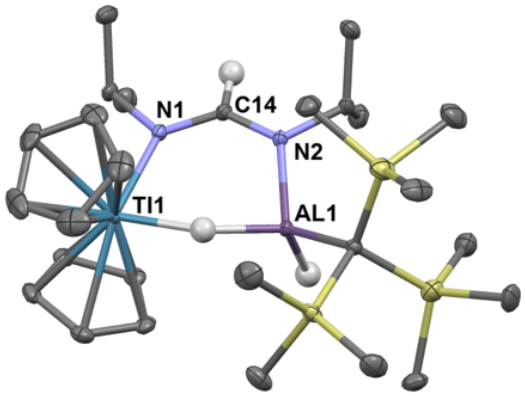

Figure 4.4. Crystallographically determined structure of **4.5.** Metal hydrides were located in the Fourier difference map and their positions were refined. Methyl groups and C-H hydrogens are omitted for clarity. Thermal ellipsoids are shown at the 50% probability level. Relevant bond lengths: Ti(1)-O(1): 1.838(2) Å, Al(1)-O(1): 1.705(2) Å, Al(1)-O(2): 1.845(2) Å, Al(1)-O(3): 1.795(2) Å, O(2)-C(21): 1.268(3) Å, C(21)-N(1): 1.322(3) Å, N(1)-C(26): 1.478(3) Å, C(26)-N(2): 1.262(3) Å, C(26)-O(3): 1.310(3) Å.

While future work will expand substrate scope and explore the mechanism for formation of **4.5**, the reactivity observed showed that **4.2** promoted formal hydride oxidation and reduction of a range of heteroallenes. The differences between **4.4** and **4.5** suggested that decreased steric pressure promotes coupling of the organic substrates. We hypothesize that similar effects are relevant to CO_2 reduction. Overall, this reactivity suggests that bimetallics could be useful for elucidating intermediates in aluminum hydride reductions.

Thermal Reactivity

Previous work with titanium-aluminum bimetallics focused on thermal decomposition *via* hydrogen elimination and C-H bond activation. Compounds **4.2** and **4.3** were heated in solution

and as neat solids to determine if each could undergo similar reactivity. Monitoring the solution-state reactions by ^{1}H NMR spectroscopy revealed that dihydrogen formed at around 100 °C (**4.2**) and 80 °C (**4.3**), concomitant with color changes from purple to blue and from purple to brown for **4.2** and **4.3**, respectively (Scheme 4.3). Both products were crystallographically characterized and shown to be $((Cp)(C_5H_4)Ti(\mu\text{-}H)_2Al(C(SiMe_3)_3))_2$ (**4.6**) and $((Cp)(C_5H_4)Ti)_2(\mu\text{-}H)_2Al(C(SiMe_3)_3)$ (**4.7**) (Figure 4.5). In both **4.2** and **4.3**, heat induced activation of Cp C-H bonds and loss of one bridging hydride generated dihydrogen and new heterometallic complexes with C-Al bonds and η^1:η^5 coordinated activated Cp rings. This mode of reactivity can be compared with previous Ti-Al bimetallic complexes in which Cp C-H activation was observed at or below room temperature.[27,31]

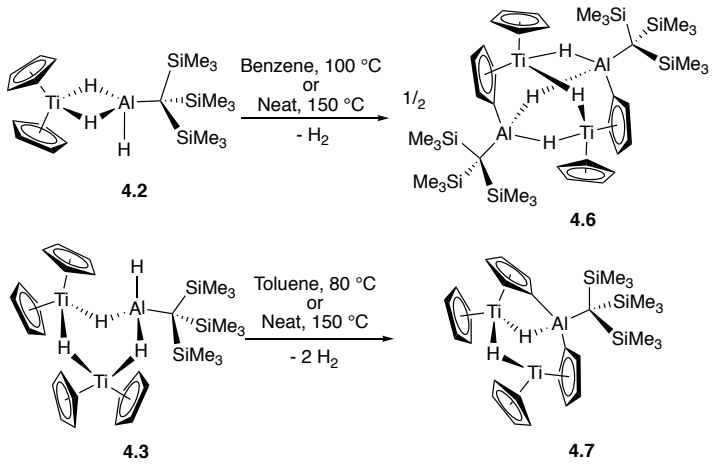

Scheme 4.3. Thermal reactivity of **4.2** and **4.3** leading to **4.6** and **4.7**.

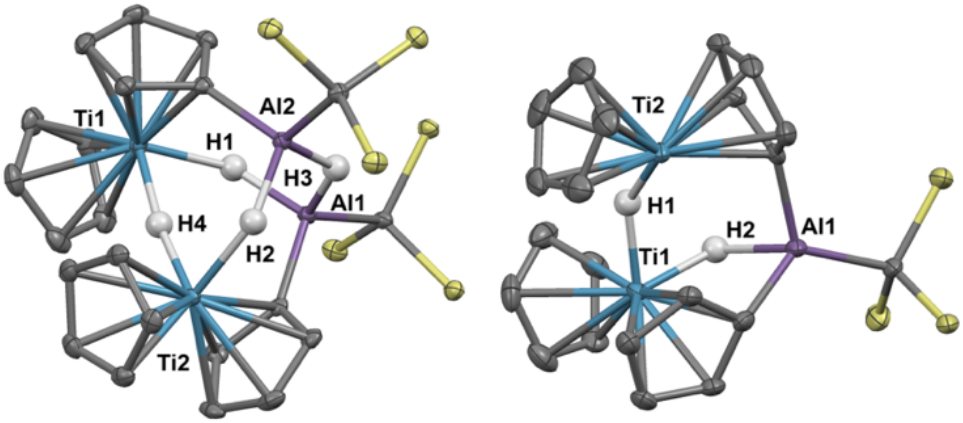

Figure 4.5. Crystallographically determined structures of **4.6** (left) and **4.7** (right). Methyl groups and C-H hydrogens are omitted for clarity. Thermal ellipsoids are shown at the 50% probability level. Metal hydrides were located in the Fourier difference map and their positions were refined. Metal-metal distances in **4.6**: Ti(1)-Al(2) 3.6235(8) Å, Ti(2)-Al(1): 3.6218(7) Å, Ti(1)-Ti(2): 3.6930(6) Å, Al(1)-Al(2): 3.2214(9) Å. Metal-metal distances in **4.7**: Ti(1)-Al(1): 2.976(1) Å, Ti(2)-Al(1): 3.594(1) Å, Ti(1)-Ti(2): 3.3074(7) Å.

Bulychev and coworkers found that substituting pentamethylcyclopentadienyl (Cp*) rings for Cp inhibited C-H activation in $[AlH_4]^-$ based Ti-Al bimetallics.[29,30] The reaction of Cp^*_2TiCl with one equivalent of $Li(THF)_2H_3AlC(SiMe_3)_3$ in hexane or diethyl ether was observed to be significantly slower than the Cp analogue; a color change from dark blue to green occurred over several days at room temperature. X-ray structure determination of the green crystals (Figure 4.6) showed that C-H activation had occurred to form $(Cp^*)(C_5Me_4CH_2)Ti(\mu\text{-}H)_2Al(C(SiMe_3)_3)$ (**4.8**), presumably with the concomitant elimination of one equivalent of dihydrogen (Scheme 4.4). Complex **4.8** was unaffected by heating in the presence of 1 atm of H_2 at 80 °C for 16 hours, which indicated that the elimination of dihydrogen was irreversible. The structure was reminiscent of tuck-in complexes that have been observed in metallocene derivatives across the Periodic Table.[63,64]

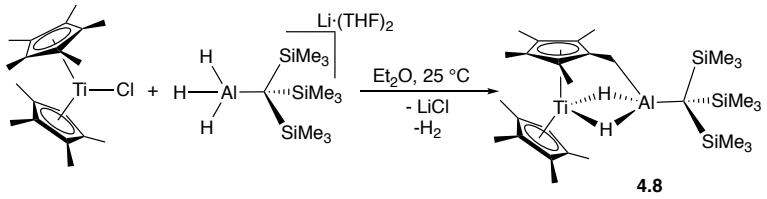

Scheme 4.4. Synthesis of **4.8**.

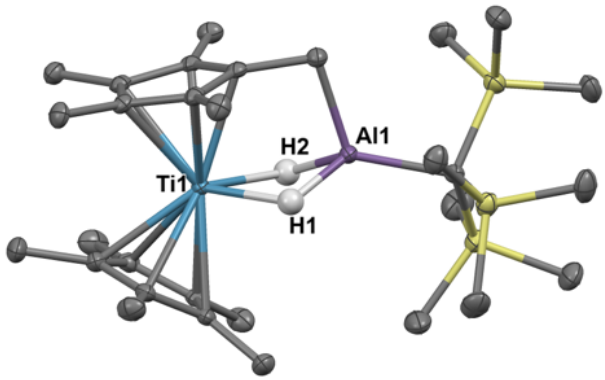

Figure 4.6. Crystallographically determined structure of **4.8**. Metal hydrides were located in the Fourier difference map and their positions were refined. Thermal ellipsoids are shown at the 50% probability level. C-H hydrogen atoms are omitted for clarity. Relevant distances and bond lengths: Ti(1)-Al(1) 2.8133(7) Å, Al(1)-C(11): 1.978(2).

We considered two mechanistic pathways for the formation of **4.6**, **4.7**, and **4.8**. The first – proposed by Bulychev and coworkers[27] – involves reductive elimination of two Al-H hydrogens followed by oxidative addition of a C-H bond. (Figure 4.7). Reductive elimination from a Ti(III) system would be unexpected; however, this pathway was considered because of its presence in the literature and because of recent examples of reductive elimination from Al(III) systems.[10-12] We hypothesized that a σ-bond metathesis mechanism in which one Al-H hydrogen and one C-H hydrogen are eliminated to directly form H_2 and a C-Al bond might be more probable.

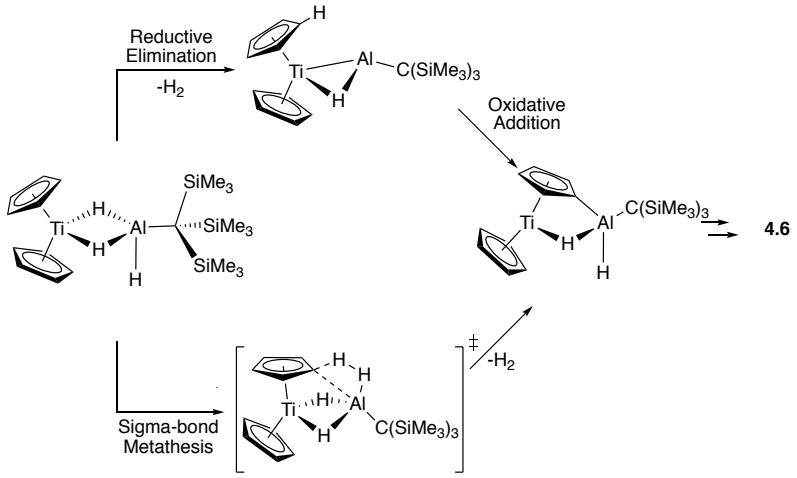

Figure 4.7. Possible model mechanisms for the conversion of **4.2** to **4.6** showing the expected results from deuterium labelling. The reaction may take place through a unimolecular or bimolecular pathways but for simplicity the unimolecular model has been shown.

To differentiate between these two mechanisms, the deuterium labelled analogue of **4.2**, in which the metal hydrides are replaced with deuterium atoms (**4.2D**), was synthesized. Upon heating, a reductive elimination mechanism was expected to result in D_2 loss and leave two bridging deuterium atoms and two bridging hydrogen atoms in **4.6**, while σ-bond metathesis was expected to produce HD and leave four bridging deuterium atoms on **4.6** (Figure 4.7).

Deuteration of both the alanate (**4.1D**) and **4.2D** was confirmed by IR spectroscopy; the strong Al-H stretches around 1646 cm^{-1} in **4.1** and the Al-H stretch at 1834 cm^{-1} in **4.2** were absent, and in both cases new peaks around 1200 cm^{-1} were present. Heating **4.2D** in deuterated benzene overnight resulted in clean conversion to **4.6D**. Deuterium labelling experiments were also carried out with **4.8** by synthesizing **4.8D** from Cp^*_2TiCl and **4.1D**.

Electron-impact mass spectrometry (EI-MS) of **4.6D** and **4.8D** showed a broad isotopic distribution indicative of scrambling of the bridging deuterium atoms throughout the molecule, including the bridging hydride positions as well as the Cp C-H bonds. Furthermore, subjecting **4.6D** to 1 atm of H_2 at 100 °C led to production of HD, though no other products were observed. This combined with EI-MS indicated that the deuterium labels were scrambled into the C-H positions in the Cp rings of **4.6** in solution. While this scrambling inhibited elucidation of previous mechanistic steps, these studies showed that bridging hydrides and Cp C-H hydrogens exchange under the reaction conditions.

To further explore the mechanism of dihydrogen elimination, we carried out DFT calculations using the model system Cp_2TiH_3AlMe (**4.2'**) for **4.2** at the B3LYP/6-31G+(d,p) level of theory (see Experimental Details). The energetic barriers for both σ-bond metathesis and reductive elimination of dihydrogen were found to be approximately 50 kcal/mol. The magnitude of these numbers likely resulted from the simplification of a bimolecular pathway to a unimolecular model. While this simplification hindered definitive assignment of a mechanism, these calculations may be used to frame the mechanistic possibilities.

σ-bond metathesis was found to be the lower energy pathway to the thermal evolution of dihydrogen from **4.2** and **4.3**, as expected. Unexpectedly, the $\Delta\Delta G^{\ddagger}$ for reductive elimination vs. σ-bond metathesis was calculated to be only 7.5 kcal/mol. Given this small difference in $\Delta G^{\ddagger}$, we

hypothesized it might be possible to favor reductive elimination under a different set of conditions. With the information gained from these DFT calculations, we set out to find conditions under which reductive elimination might occur.

Oxidation Reactivity

Since oxidation of Ti(III) to Ti(IV) increases the electron deficiency of the complex, reductive elimination modes of reactivity are expected to be enhanced. Initial attempts to synthesize bimetallics from Ti(IV) starting materials were unsuccessful due to the reducing nature of **4.1**. Instead, the reactivity of **4.2** with oxidizing agents was studied to determine if reductive elimination was possible for a Ti(IV)/Al(III) complex.

Reaction of **4.2** with $[Cp_2Fe][PF_6]$ resulted in vigorous bubbling and the formation of a bright green solution. NMR spectroscopy confirmed the formation of dihydrogen and ferrocene. From this reaction, a new species **4.9** could be crystallized; X-ray structure determination revealed it to be the trimetallic species $(Cp_2Ti)_2(\mu\text{-}F)_3(F)Al(C(SiMe_3)_3)$ (Scheme 4.5 and Figure 4.8). Compound **4.9** is structurally analogous to **4.3**, with fluorides in place of hydrides. Both titanium centers maintain the formally +3 oxidation state; the total magnetic moment including both titanium centers (2.24(2) μ_B) is higher than that observed for **4.3** due to the greater the metal-metal separation in **4.9**, which inhibits antiferromagnetic coupling.

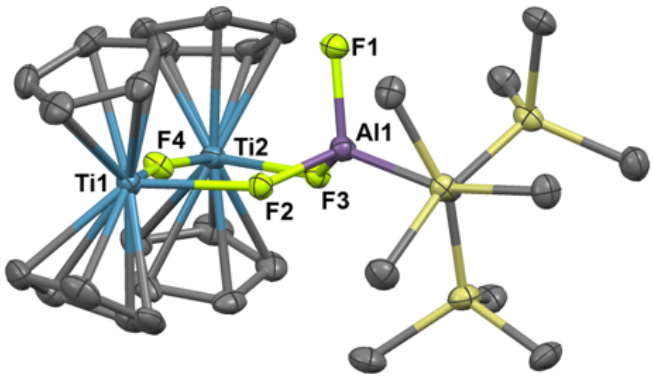

Figure 4.8. Crystallographically determined structure of **4.9**. Thermal ellipsoids are shown at the 50% probability level. C-H hydrogen atoms are omitted for clarity. Relevant distances and bond lengths: Ti(1)-Al(1): 3.640(1) Å, Ti(2)-Al(1): 3.643(1) Å, Ti(1)-Ti(2): 4.085(1) Å, Ti(1)-F(2): 2.156(2) Å, Ti(1)-F(4): 2.051(2) Å, Ti(2)-F(4): 2.060(2) Å, Ti(2)-F(3): 2.186(2) Å, Al(1)-F(1): 1.677(3) Å, Al(1)-F(2): 1.724(2) Å, Al(1)-F(3): 1.725(2) Å.

To avoid the fluoride abstraction evident in the formation of **4.9**, we attempted the reactions of **4.2** with $[Cp_2Fe][BAr_{F24}]$, $[Cp_2Fe][BAr_{F20}]$, $[Cp_2Fe][BPh_4]$, and $CuCl_2$.[‡] In all cases a mixture of products was obtained and no pure materials could be isolated; however, a resonance corresponding to dihydrogen was observed by ^1H NMR spectroscopy.

Cyclic voltammetry of **4.2** in 1,2-difluorobenzene using tetrabutylammonium BAr_{F20} as the electrolyte showed an irreversible oxidation at 1.13 V vs. Cp_2Co/Cp_2Co^+. The observed irreversibility of this wave, combined with consistent production of dihydrogen regardless of the oxidizing agent used, suggested that oxidation of Ti(III) to Ti(IV) prompts dihydrogen evolution to form a highly reactive species capable of activating a variety of counterions.

In an effort to trap a Ti(IV) containing heterometallic, oxidizing agents with coordinating counterions were employed. Reaction of **4.2** with one equivalent of AgOTf (OTf=trifluoromethanesulfonate) in toluene produced a rapid color change from purple to red, followed by the development of a bright blue color and evolution of gas. A blue product (**4.10**) was isolated (Scheme 4.5). Despite a coordinating anion present to stabilize a diamagnetic, oxidized Ti(IV) species, the paramagnetism of the product was evident from ^{1}H NMR spectroscopy. The X-ray crystal structure of **4.10** confirmed formation of the Ti(III) species, $Cp_2Ti(\mu\text{-}H)(\mu\text{-}OTf)Al(H)(C(SiMe_3)_3)$ in which one of the bridging hydrides in the starting material has been replaced by a triflate (Figure 4.9).

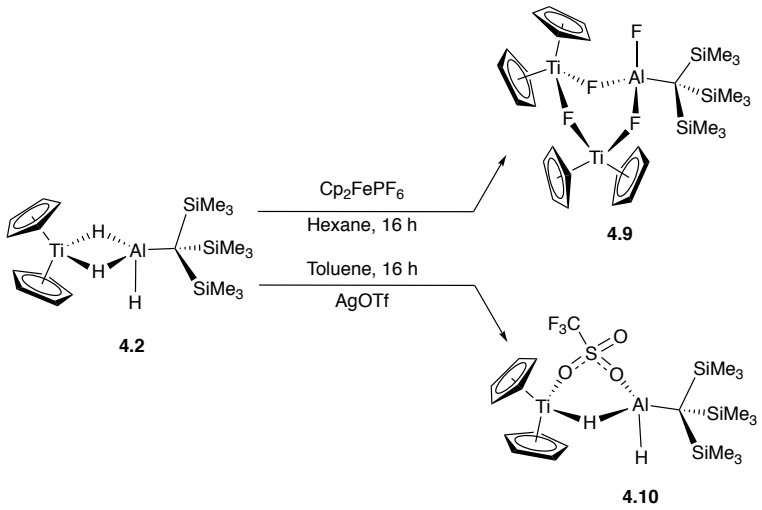

Scheme 4.5. Reactivity of **4.2** upon treatment with oxidizing agents.

The formation of **4.10** and dihydrogen could be rationalized as the reductive elimination of dihydrogen after oxidation by silver. Using data from ^{1}H NMR spectroscopy (which showed that H_2 gas was produced even in deuterated solvents) and EI-MS (which revealed that no deuterium was incorporated into the product), we determined that both the eliminated hydrogen atoms and the remaining hydrides in **4.10** came from **4.2** rather than from the solvent. Therefore, we proposed that a bimolecular reductive elimination process[65,66] occurs after oxidation of Ti(III) to Ti(IV), in which two molecules of **4.2** each eliminate one hydrogen atom. In this process, a one-electron reduction of each heterobimetallic occurs and a triflate anion coordinates to form the product, **4.10** (Scheme 4.6). A related reductive elimination pathway may be operative when non-coordinating anions are used; in these cases, elimination of dihydrogen is followed by activation of the counterion by the coordinatively unsaturated bimetallic, as was seen in the formation of **4.9**.

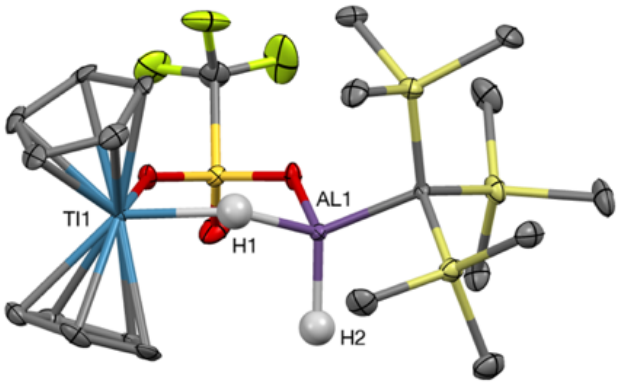

Figure 4.9. Crystallographically determined structure of **4.10**. Metal hydrides were located in the Fourier difference map and their positions were refined. C-H hydrogens are omitted for clarity. Thermal ellipsoids are shown at the 50% probability level. Relevant distances and bond lengths: Ti(1)-Al(1): 3.384(1) Å, Ti(1)-O(1): 2.217(2) Å, Al(1)-O(2): 1.876(3) Å.

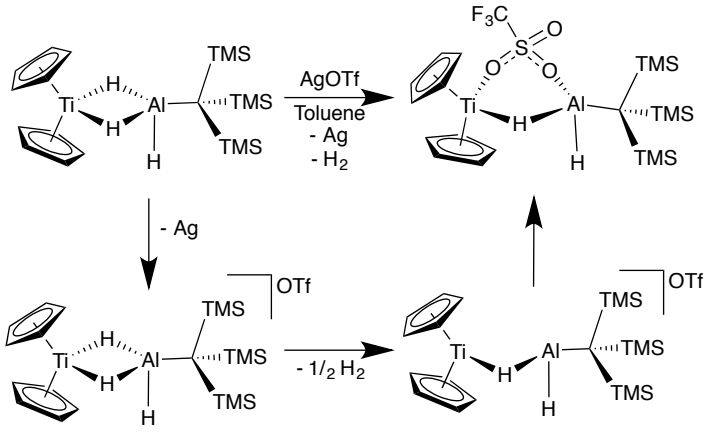

Scheme 4.6. Proposed mechanism for the bimolecular reductive elimination of dihydrogen from **4.2**. While coordination of triflate subsequent to reductive elimination is depicted, the triflate ion could coordinate before reductive elimination. This difference is likely negligible in nonpolar solvents in which ions are tightly paired.

From our DFT calculations (see above), the SOMO for **4.2'** was found to be a Ti-based orbital with Ti-H bonding character (Figure 4.10). Removing an electron from this orbital upon oxidation likely weakens the Ti-H bonds, facilitating reductive elimination of dihydrogen. This is consistent with the expected behavior for a reductive elimination process; a decrease in electron density at the metal center makes reductive elimination pathways more favorable. While we found that Ti(III) containing heterometallics may access σ-bond metathesis pathways to activate hydrides at elevated temperatures, reductive elimination was strongly favored upon oxidation to Ti(IV), allowing for dihydrogen formation without ligand activation at room temperature. In contrast to other proposed mechanisms of dihydrogen elimination,[42] this bimolecular reductive elimination does not require a two-electron reduction at either the transition metal or the aluminum, and

therefore provides new opportunities for dihydrogen elimination from systems in which two-electron reductions are difficult to access.

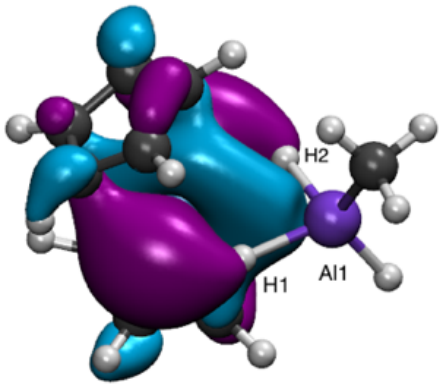

Figure 4.10. DFT calculated SOMO of **4.2**.

Such redox chemistry bears relevance to the reasons titanium dopants improve H_2 elimination performance of aluminum hydrogen storage materials. In our molecular systems, oxidation led to reductive elimination of hydrogen and the formation of a coordinatively unsaturated species that was trapped with a coordinating counterion. The transfer of electrons away from the titanium-aluminum center may encourage the evolution of hydrogen in materials as well; however, the additional electron density may be delocalized across the material to temper the reactivity of the species following reductive elimination. In general, the reductive elimination of dihydrogen from this titanium-aluminum bimetallic suggested that new chemistry may be accessible from aluminum hydride based molecules and materials, and further investigations are necessary to elucidate the underlying causes of this reactivity. Spectroscopic evaluation of the electronic structure in such bimetallic species will be the focus of future work.

Conclusions

Stable, yet reactive paramagnetic titanium aluminum heterometallics, including a titanium-aluminum bimetallic complex with bridging hydrides, were synthesized using an alanate supported by the sterically encumbering tris(trimethylsily)methyl ligand. Treatment of the bimetallic complex with diisopropylcarbodiimide resulted in a hydride insertion product while treatment of the bimetallic complex with *tert*-butylisocyanate resulted in transfer of an oxo moiety and isocyanate coupling. Upon heating the heterometallics, C-H bonds in the Cp ligands on titanium were activated; the thermal evolution of dihydrogen likely occurs via σ-bond metathesis. Oxidation of the heterobimetallic consistently resulted in the formation of dihydrogen regardless of the oxidizing agent used. Trapping experiments showed that oxidation triggered bimolecular reductive elimination of dihydrogen. Such reactivity may provide insights into the mechanism of hydrogen evolution in hydrogen storage materials.

Notes.

‡(BAr_{F24}=tetrakis[3,5-bis(trifluoromethyl)phenyl]borate), (BAr_{F20}=tetrakis(pentafluorophenyl)borate)), (BPh_4=tetraphenylborate)

Experimental Details

General Considerations. Unless otherwise noted, all reactions were performed using standard Schlenk line techniques or in an MBraun inert atmosphere glove box under an atmosphere of nitrogen (<1ppm O_2/H_2O). Glassware and Celite® were stored in an oven at ca. 140 °C. Molecular sieves (4 Å) were activated by heating to 300 °C overnight under vacuum prior to storage in a glovebox. Diethyl ether (Et_2O), tetrahydrofuran (THF), n-hexane and toluene were degassed and dried using a Phoenix solvent drying system commercially available from JC Meyer Solvent Systems and were stored under an atmosphere of nitrogen. Hexamethyldisiloxane (HMDSO) was distilled from sodium/benzophenone, degassed by sparging with nitrogen, and stored over 4 Å molecular sieves. C_6D_6 was dried over Na/benzophenone and degassed by three freeze–pump–thaw cycles before being vacuum transferred and subsequently stored in the glovebox over 4 Å activated molecular sieves. Cp^*_2TiCl,[67] Cp_2TiCl,[68,69] $(SiMe_3)_3CH$,[70] $LiH_3AlC(SiMe_3)_3\bullet(THF)_2$,[51] Cp_2FePF_6[71] were prepared according to literature procedures. Cp_2FeBAr_{F24}, Cp_2FeBAr_{F20} and Cp_2FeBPh_4 were prepared by the same procedure as for Cp_2FePF_6 from $NaBAr_{F24}$,[72] $KBAr_{F20}$ and $NaBPh_4$, respectively. All other reagents were purchased and used as received with the exception of $LiAlH_4$ which was purified by extraction into Et_2O and potassium bis(trimethylsilyl)amide (KHMDS) which was recrystallized from toluene. Isocyanates and carbodiimides were degassed by three freeze-pump-thaw cycles and stored over sieves. NMR spectra were recorded on Bruker AV-600, AV-500, AVB-400, AVQ-400, AV-300, and DRX-500 spectrometers. ^1H and $^{13}C\{^1H\}$ chemical shifts are given relative to residual solvent peaks. ^{27}Al NMR chemical shifts are referenced to an external standard of 1 M $Al(NO_3)_3$ in H_2O/D_2O (δ 0 ppm). For paramagnetic samples, ^1H NMR integrations were not found to be reliable, and the majority of resonances were difficult to assign. However, the presence of a broad resonance between 0.3 and 0.5 ppm, assigned to the Si-CH_3 protons, was found to be diagnostic of one paramagnetic aluminum species in solution. FT-IR samples were prepared as Nujol mulls and were taken between KBr disks using a Nicolet iS10 FT-IR spectrometer. UV–visible spectra were collected in hexane and determined with a Varian Cary 50 UV-visible spectrophotometer, using a Schlenk-adapted 1 cm or 1 mm quartz cell. Melting points were determined using an OptiMelt automated melting point system. Elemental analyses were determined at the School of Human Sciences, Science Center, London Metropolitan University. For several samples, satisfactory elemental analyses could not be obtained after multiple attempts, presumably due to minor decomposition from air exposure or slow solvent loss from the crystal lattice during analysis.

$KH_3AlC(SiMe_3)_3$ (4.1). Synthesized according to a modification of the $LiH_3AlC(SiMe_3)_3\bullet(THF)_2$ procedure.[51] $(SiMe_3)_3CH$ (7.25 mL, 0.026 mol) was dissolved in 30 mL of THF and methyllithium (1.6 M in Et_2O, 17 mL, 0.027 mol) was added via syringe. The solution was heated to reflux for 16 h after which it was cooled to room temperature and added to $LiAlH_4$ (1.2 g, 0.032 mol) in 5 mL of THF. The solution immediately became cloudy white. This mixture was heated to 60 °C for 2 h after which the solvent was removed *in vacuo*. The solid was triturated twice with 5 mL of toluene before extraction into 100 mL of toluene. This solution was added to KHMDS (5.16 g, 0.026 mol) in 10 mL of toluene and stirred overnight. The solvent was removed in vacuo and the solid triturated thoroughly with 5 mL of toluene before it was redissolved in 100 mL of toluene. The cloudy suspension was filtered through Celite® to give a colorless solution. The solvent was removed *in vacuo* and the resulting solid was suspended in hexane and collected on a Schlenk frit. Yield: 5.55 g (71%). ^1H NMR (400 MHz, C_6D_6, 293 K) δ 0.49 ppm (s, 27H, Si-CH_3). ^{27}Al NMR (104 MHz, C_6D_6, 293 K) δ 115.8. FT-IR (KBr, Nujol, cm^{-1}): 1647 (s, br), 1245 (s), 1020 (w), 868 (s, br), 777 (m), 728 (m), 670 (m), 657 (m), 576 (w). MP: dec. 230-286 °C.

$KD_3AlC(SiMe_3)_3$ (4.1D). Synthesized by the procedure reported for **4.1** $(SiMe_3)_3CH$ (3.6 mL, 0.013 mol) was dissolved in 30 mL of THF. Methyllithium (1.6 M in Et_2O, 8.5 mL, 0.014 mol) was added via syringe. The solution was heated to reflux for 16 h. The solution was cooled to room temperature and added to $LiAlD_4$ (0.67 g, 0.016 mol) in 5 mL of THF. The solution immediately turned cloudy white. This mixture was heated to 60 °C for 2 h and the solvent was removed *in vacuo*. The solid was triturated twice with 5 mL of toluene before extraction into 75 mL of toluene. This solution was added to KHMDS (2.59 g, 0.013 mol) in 10 mL of toluene and stirred overnight. The solvent was removed *in vacuo* and the solid triturated thoroughly with 5 mL of toluene before it was redissolved in 75 mL of toluene. The white solution was filtered through Celite® to give a colorless solution. The solvent was removed *in vacuo* and the resulting solid was suspended in hexane and collected on a Schlenk frit. Yield: 2.7 g (69 %). Characterization was identical to that reported for **4.1** but the IR stretch at 1646 cm^{-1} was absent.

$Cp_2TiH_3AlC(SiMe_3)_3$ (4.2). Cp_2TiCl (0.485 g, 2.27 mmol) and $KH_3AlC(SiMe_3)_3$ (1.41 g, 4.69 mmol) were dissolved in 20 mL of $E_{t2}O$ cooled to -78 °C. The solution immediately turned bright purple. The mixture was allowed to warm to room temperature and stirred for 30 min. Solvent was removed *in vacuo* and the solid was triturated with 5 mL of hexane. The solid was then suspended in 50 mL of hexane and stirred for 3 h, over which time the solution became blue-purple. The mixture was concentrated to 20 mL and filtered through Celite®. The solvent was removed *in vacuo* to yield blue-purple crystals. Yield: 826 mg (83 %). $Cp_2TiH_3AlC(SiMe_3)_3$ obtained contained approximately 5% $KH_3AlC(SiMe_3)_3$ which was not found to impede further reactivity studies. X-ray quality and analytically pure crystals were grown by storage of a concentrated hexane solution at -40 °C (Approximate recovery: 40 %). ^1H NMR (500 MHz, C_6D_6, 293 K) δ 0.35 (s, Si-CH_3) $^{13}C\{^1H\}$ NMR (126 MHz, C_6D_6, 293 K) δ 7.2 (Si-CH_3) Anal calcd. (%) for $C_{20}H_{40}AlSi_3Ti$: C, 54.64; H, 9.17 Found: C, 54.63; H, 9.22. MP: dec. 116-148 °C. FT-IR (KBr, Nujol, cm^{-1}): 1831 (m), 1259 (m), 1250 (m), 1201 (m), 1099 (w), 1012 (w), 848 (s, br), 805 (m), 721 (w), 672 (w), 661 (w). UV-Vis: 529 nm (toluene, ε=3000 L/mol.cm) μ_{eff}=1.70 μ_B.

$Cp_2TiD_3AlC(SiMe_3)_3$ (4.2D). Synthesized according to the procedure reported for **4.2.** Cp_2TiCl (0.25 g, 1.17 mmol) and $KD_3AlC(SiMe_3)_3$ (0.710 g, 2.34 mmol) were dissolved in 20 mL of Et_2O cooled to -78 °C. The solution immediately turned bright purple. The mixture was allowed to warm to room temperature and was stirred for 30 min. Solvent was removed *in vacuo* and the solid was triturated with 5 mL of hexane. The solid was then suspended in 30 mL of hexane and stirred for 3 h, over which time the solution became blue-purple. The mixture was concentrated to 10 mL and filtered through Celite®. The solvent was removed *in vacuo* to yield blue-purple crystals. Characterization was identical to that reported for **4.2** but the IR stretch at 1834 cm^{-1} was absent.

$(Cp_2Ti)_2H_4AlC(TMS)_3$ (4.3). Cp_2TiCl (250. mg, 1.06 mmol) and $KH_3AlC(SiMe_3)_3$ (161 mg, 0.535 mmol) were dissolved in 10 mL of hexane. The purple solution was stirred for 4 h and then filtered through Celite®. The resulting pink-purple solution was concentrated to 5 mL and stored overnight at -40 °C to yield dark purple crystals. Yield: 58 mg (32 %). X-ray quality crystals were grown by vapor diffusion of HMDSO into a concentrated hexane solution at room temperature over 3 d. ^1H NMR (500 MHz, C_6D_6, 293 K) δ 0.33 (s, Si-CH_3) $^{13}C\{^1H\}$ NMR (126 MHz, C_6D_6, 293 K) δ 8.1 (Si-CH_3), 100.4 (C-Cp), ^{27}Al NMR (130 MHz, C_6D_6, 293 K) δ 128.5 MP: dec. 177-223 °C. FT-IR (KBr, Nujol, cm^{-1}): 1811 (m), 1564 (m), 1258 (m), 1091 (w), 1012 (m), 849 (s, br), 795 (s), 732 (w), 659 (m). μ_{eff}=1.66 μ_B.

$Cp_2TiH((^iPr)N(CH)N(^iPr))HAlC(SiMe_3)_3$ (4.4). $Cp_2TiH_3AlC(SiMe_3)_3$ (195 mg, 0.444 mmol) was dissolved in 5 mL of hexane and a solution of diisopropylcarbodiimide (165 mg, 1.31 mmol) in 2 mL of hexane was added. The mixture was stirred for 1 h before the solvent was removed *in*

vacuo. The solids were dissolved in 10 mL pentane and the solution was concentrated to 5 mL and stored at -40 °C overnight to yield blue crystals (50 mg). A second crop of crystals could be obtained through further concentration of the solution (25 mg). Yield: 75 mg (30%). ^{1}H NMR (600 MHz, C_6D_6, 293 K) δ 0.44 (s, Si-CH_3), 1.03, 1.73, 5.09. MP: dec. 132-138 °C. FT-IR (KBr, Nujol, cm-1): 1783 (m), 1666 (m, br), 1595 (m), 1367 (m), 1330 (w), 1256 (m), 1246 (m), 1172 (w), 1124 (m), 1097 (w), 1017 (m), 927 (w), 846 (s, br), 797 (s), 765 (m), 677 (m), 657 (m). Anal calcd. (%) for $C_{27}H_{54}AlN_2Si_3Ti$: C, 57.31; H, 9.62; N, 4.95 Found: C, 57.40; H, 9.69; N, 4.85.

$Cp_2TiOAl(OCHN^tBuC(N^tBuO)(C(SiMe_3)_3)$ (4.5). $Cp_2TiH_3AlC(SiMe_3)_3$ (200 mg, 0.455 mmol) was dissolved in 5 mL of hexane and a solution of ^{t}BuNCO (135 mg, 1.365 mmol) in 2 mL of hexane was added. The mixture was stirred for 1 h, then the solution was filtered. The solvent was removed *in vacuo* and the solids were dissolved in 10 mL of toluene. The solution was concentrated to 5 mL and stored at -40 °C overnight to yield green crystals. Yield: 72 mg (24%). ^{1}H NMR (600 MHz, C_6D_6, 293 K) δ 0.30 (s, Si-CH_3), 0.79, 2.44 MP: dec. 103-145 °C. FT-IR (KBr, Nujol, cm^{-1}): 1687 (m), 1600 (m), 1566 (m), 1248 (m), 1016 (m), 906 (s), 860 (s), 790 (s), 722 (w), 669 (m).

$((Cp)(C_5H_4)TiH_2AlC(SiMe_3)_3)_2$ (4.6). Solid $Cp_2TiH_3AlC(SiMe_3)_3$ (260 mg, 0.591 mmol) was heated to 150 °C for 20 min. During this time, the purple solid melted and gas evolution and a color change to dark blue was observed. The solid was cooled to room temperature and extracted with 30 mL hexane, concentrated to 10 mL, and stored at -40 °C overnight to yield dark blue crystals suitable for X-ray analysis. Yield: 86 mg (33 %) Higher yields are possible upon further concentration of the solution. ^{1}H NMR (500 MHz, C_6D_6, 293 K) δ 0.43 (s, Si-CH_3) $^{13}C\{^1H\}$ NMR (126 MHz, C_6D_6, 293 K) δ 12.8 (Si-CH_3) MP: dec. 220-246 °C. FT-IR (KBr, Nujol, cm^{-1}): 1640 (m, br), 1258 (m), 1248 (m), 1043 (w), 1005 (w), 853 (s, br), 786 (m), 661 (w), 643 (w). UV-Vis: 600 nm (toluene, ε=628 L/mol·cm).

$((Cp)(C_5H_4)TiD_2AlC(SiMe_3)_3)_2$ (4.6D). $Cp_2TiH_3AlC(SiMe_3)_3$ (50. mg, 0.11 mmol) was heated to 100 °C in 0.7 mL of C_6D_6 for 2 h. The solvent was removed *in vacuo*. The crude solid was analyzed using EI-MS, and the broad distribution of peaks was indicative of isotopic scrambling.

$((Cp)(C_5H_4)Ti)_2H_2AlC(SiMe_3)_3$ (4.7). $(Cp_2Ti)_2H_4AlC(SiMe_3)_3$ (230. mg, 0.372 mmol) was dissolved in 20 mL of toluene and heated to 80 °C for 16 h. Over this time the color changed from purple to reddish-brown. The solvent was removed *in vacuo* and the solid was extracted into 15 mL of hexane. The solution was concentrated to 10 mL and stored at -40 °C overnight to yield brown crystals. Yield: 123 mg (54 %). X-ray quality crystals were grown by vapor diffusion of hexane into a concentrated toluene solution at -40 °C. ^{1}H NMR (500 MHz, C_6D_6, 293 K) δ 0.16 (s, Si-CH_3) ^{27}Al NMR (130 MHz, C_6D_6, 293 K) δ -134. MP: dec. 215-250 °C. FT-IR (KBr, Nujol, cm^{-1}): 1579 (m, br), 1257 (m), 1248 (m), 1075 (m, br), 1012 (m), 852 (s), 801 (s), 723 (w), 666 (m). UV-Vis: 454 nm (toluene, ε=271 L/mol·cm).

$(Cp^*)(C_5Me_4CH_2)TiH_2AlC(SiMe_3)_3$ (4.8). Cp*TiCl (501 mg, 1.41 mmol) and $LiH_3AlC(SiMe_3)_3\cdot(THF)_2$ (590. mg, 1.43 mmol) were dissolved in 20 mL of Et_2O. The solution was stirred for 10 d at room temperature, over which time the solution turned cloudy and green. The solvent was removed *in vacuo* and the solids were extracted into 20 mL of hexane. The solution was filtered through Celite® and the resulting green solution was concentrated to 15 mL and stored at -40 °C overnight to yield dark green crystals of suitable quality for X-ray analysis. Yield: 395 mg (49%) ^{1}H NMR (500 MHz, C_6D_6, 293 K) δ 0.38 (s, Si-CH_3), MP: dec. 174-241 °C. FT-IR (KBr, Nujol, cm^{-1}): 1248 (m), 1049 (m), 1021 (m), 853 (s, br), 785 (m), 665 (m). Anal calcd. (%) for $C_{30}H_{58}AlSi_3Ti$: C, 62.35; H, 10.12 Found: C, 62.22; H, 9.99.

(Cp*)($C_5Me_4CH_2$)$TiD_2AlC(SiMe_3)_3$ (4.8D). Cp*TiCl (46 mg, 0.13 mmol) and $KD_3AlC(SiMe_3)_3$ (40 mg, 0.13 mmol) were dissolved in 5 mL of Et_2O. The solution was stirred for 5 d at room temperature, over which time the solution turned cloudy and green. The solvent was removed *in vacuo* and the solids were extracted into 5 mL of hexane. The solution was filtered through Celite® and the resulting green solution was concentrated to 2 mL and stored at -40 °C overnight to yield dark green crystals. The crystals were analyzed using EI-MS, and a broad peak molecular ion peak around 575 was observed, indicative of isotopic scrambling.

$(Cp_2Ti)_2F_4AlC(SiMe_3)_3$ (4.9). $Cp_2TiH_3AlC(SiMe_3)_3$ (195 mg, 0.444 mmol) and $[Cp_2Fe][PF_6]$ (147 mg, 0.444 mmol) were suspended in 10 mL of hexane. The solution rapidly became dark green and gas evolution was observed; the mixture was stirred for 16 h. The solution was then filtered to yield a bright green solution. This solution was concentrated to 5 mL and stored at -40 °C overnight to yield green crystals. Yield: 76 mg (50 %). X-ray quality crystals were grown by vapor diffusion of HMDSO into a concentrated hexane solution at room temperature. ^{1}H NMR (500 MHz, C_6D_6, 293 K) δ 0.33 (s, Si-CH_3) $^{13}C\{^1H\}$ NMR (126 MHz, C_6D_6, 293 K) δ 5.51 (Si-CH_3). FT-IR (KBr, Nujol, cm^{-1}): 1256 (m), 1025 (m), 1012 (m), 856 (s), 813 (m), 796 (s), 755 (w), 672 (m), 658 (m), 617 (m). Anal calcd. (%) for $C_{30}H_{47}AlF_4Si_3Ti_2$: C, 52.17; H, 6.86 Found: C, 51.97; H, 6.92. MP: dec. 218-280 °C μ_{eff}=2.24 μ_B.

$Cp_2TiH(OTf)AlH(C(SiMe_3)_3)$ (4.10). In a darkened glovebox, $Cp_2TiH_3AlC(SiMe_3)_3$ (200. mg, 0.455 mmol) was dissolved in 5 mL of toluene and added to AgOTf (117 mg, 0.455 mmol) in 2 mL of hexane. The mixture was stirred in darkness for 16 h and then the solution was filtered. The solvent was removed *in vacuo* and the resulting solid was dissolved in 10 mL of hexane. The solution was concentrated to 5 mL and stored at -40 °C overnight to yield blue crystals. Yield: 109.4 mg (40 %). X-ray quality crystals were grown by slow evaporation of hexane at -40 °C. ^{1}H NMR (500 MHz, C_6D_6, 293 K) δ 0.40 (s, Si-CH_3). FT-IR (KBr, Nujol, cm^{-1}): 1860 (m), 1633 (m, br), 1332 (s), 1253 (s), 1226 (s), 1157 (m), 853 (s) 807 (s), 722 (w), 673 (m), 634 (m), 516 (w). MP: 126-129 °C.

Deuterium labelling of 4.10. In an NMR tube in a darkened glovebox, $Cp_2TiH_3AlC(SiMe_3)_3$ (26.2 mg, 0.059 mmol) in 0.4 mL of d^8-toluene was added to a solution of AgOTf (15.6 mg, 0.059 mmol) in 0.4 mL of d^8-toluene. The solution was allowed to sit for 16 h in the dark. Over this time, the solution turned blue and silver metal precipitated. A ^{1}H NMR spectrum was recorded, and H_2 was observed. The solution was removed from the NMR tube and the NMR tube was washed with 2 mL of hexane. The solution and washings were combined and filtered through Celite®. The solvent was removed *in vacuo* and the remaining blue solid was analyzed using EI-MS, and a molecular ion peak of 587.1174 was observed consistent with $C_{21}H_{39}O_3F_3AlSi_3STi$, indicating that both metal hydrides were hydrogen and not deuterium.

X-ray Diffraction. X-ray structural determinations were performed at CHEXRAY, University of California, Berkeley on a APEX II QUAZAR or SMART APEX Diffractometer or at the Advanced Light Source (ALS) station 11.3.1 using a silicon-monochromated beam of 16 keV (0.7749 Å) synchrotron radiation. In both cases, diffraction data was collected, integrated, and corrected for absorption using Bruker APEX3 software and its associated modules (SAINT, SADABS). Structural solutions and refinements (on F^2) were carried out using SHELXT and SHELXL-2014 in WinGX. Ellipsoid plots and figures were made using Mercury.

Table 4.1. Crystallographic details for compounds **4.1**-**4.5**.

	4.1	**4.2**	**4.3**	**4.4**	**4.5**
Chemical formula	$C_{18}H_{46}AlKO_2Si_3$	$C_{20}H_{40}AlSi_3Ti$	$C_{30}H_{51}AlSi_3Ti_2$	$C_{27}H_{54}AlN_2Si_3Ti$	$C_{30}H_{56}AlN_2O_3Si_3Ti$
Formula weight	444.90	439.67	618.75	565.87	651.91
Color, habit	Colorless, plates	Purple, block	Purple, needles	Blue, blocks	Green, needles
Temperature (K)	100(2)	100(2)	100(2)	100(2)	100(2)
Crystal system	Triclinic	Monoclinic	Triclinic	Monoclinic	Orthorhombic
Space group	P -1	P 2_1/c	P -1	P 2_1/n	Pna2_1
a (Å)	13.5985(5)	18.6834(11)	11.8167(11)	11.686(8)	12.528(7)
b (Å)	13.6009(5)	9.2143(5)	16.7464(16)	15.467(10)	18.992(10)
c (Å)	16.6858(7)	15.3519(8)	18.0477(18)	18.639(12)	15.352(8)
α (°)	106.549(2)	90	105.953(4)	90	90
β (°)	107.020(2)	108.428(2)	103.150(4)	107.884(5)	90
γ (°)	98.456(2)	90	90.965(4)	90	90
V (Å^3)	2737.83(19)	2507.4(2)	3331.8(6)	3212(4)	3653(3)
Z	4	4	4	4	4
Density (Mg m^{-3})	1.079	1.165	1.234	1.170	1.185
F(000)	976	948	1320.0	1228	1404
Radiation Type	MoK_α	MoK_α	MoK_α	Synchrotron	Synchrotron
μ (mm^{-1})		0.522	0.631	0.495	0.468
Crystal size	0.18 x 0.16 x 0.16	0.20 x 0.20 x 0.20	0.16 x 0.06 x 0.04	0.6 x 0.4 x 0.16	0.15 x 0.05 x 0.05
Meas. Refl.	15870	62302	148243	32982	36396
Indep. Refl.	8712	4606	12286	7486	8342
R(int)	0.0402	0.0466	0.0738	0.390	0.0499
Final R indices [I > 2σ(I)]	R = 0.0437 R_w = 0.1307	R = 0.0418 R_w = 0.1113	R = 0.0933 R_w = 0.2365	R = 0.0306 R_w = 0.0735	R = 0.0278 R_w = 0.0630
Goodness-of-fit	1.024	1.101	1.052	1.041	1.037
$\Delta\rho_{max}$, $\Delta\rho_{min}$ (e Å^{-3})		0.760, -0.532	3.734, -0.976	0.346, -0.404	0.195, -0.313
CCDC	1530362	1530361	1530366	1530368	1530367

Table 4.2. Crystallographic details for compounds **4.6-4.10**.

	4.6	**4.7**	**4.8**	**4.9**	**4.10**
Chemical formula	$C_{40}H_{76}Al_2Si_6Ti_2$	$C_{30}H_{47}AlSi_3Ti_2$	$C_{30}H_{58}AlSi_3Ti$	$C_{30}H_{47}AlF_4Si_3Ti_2$	$C_{21}H_{39}AlF_3O_3SSi_3Ti$
Formula weight	875.28	614.72	577.91	690.72	587.73
Color, habit	Blue, block	Brown, needles	Green, blocks	Green, blocks	Blue, plates
Temperature (K)	100(2)	100(2)	100(2)	100(2)	100(2)
Crystal system	Monoclinic	Monoclinic	Monoclinic	Triclinic	Monoclinic
Space group	P 2_1/c	P 2_1/c	P 2_1/c	P -1	P 2_1/n
a (Å)	13.8040(5)	13.9593(11)	17.5367(5)	12.1490(6)	15.9334(5)
b (Å)	20.5426(10)	26.812(2)	11.3812(3)	16.6519(9)	8.8807(2)
c (Å)	18.7994(9)	9.5669(6)	18.6758(5)	18.1791(9)	41.2358(12)
α (°)	90	90	90	105.807(3)	90
β (°)	105.291(2)	90.391(4)	115.366(1)	102.060(2)	92.756(2)
γ (°)	90	90	90	91.054	90
V (Å^3)	5142.2(4)	3580.6(5)	3368.11(16)	3449.4(3)	5828.1(3)
Z	4	4	4	4	8
Densitiy (Mg m^{-3})	1.186	1.140	1.140	1.330	1.340
F(000)	1980.0	1304.0	1260.0	1448.0	2472.0
Radiation Type	MoK_α	MoK_α	MoK_α	MoK_α	MoK_α
μ (mm^{-1})	0.512	0.587	0.404	0.633	0.559
Crystal size	0.30 x 0.20 x 0.20	0.60 x 0.40 x 0.10	0.14 x 0.10 x 0.09	0.08 x 0.06 x 0.05	0.08 x 0.05 x 0.01
Meas. Refl.	127502	73258	44586	113817	127278
Indep. Refl.	9445	6541	6166	12679	10668
R(int)	0.0941	0.1742	0.0395	0.1061	0.0798
Final R indices [I > 2σ(I)]	R = 0.0384 R_w = 0.0896	R = 0.0484 R_w = 0.1128	R = 0.0477 R_w = 0.1232	R = 0.0578 R_w = 0.1261	R = 0.0532 R_w = 0.1174
Goodness-of-fit	1.066	0.945	1.066	1.042	1.038
$\Delta\rho_{max}$, $\Delta\rho_{min}$ (e Å^{-3})	0.529, -0.333	0.937, -0.409	1.450, -0.291	1.452, -0.408	0.616, -0.359
CCDC	1530364	1530360	1530363	1530365	1530369

Computational Details. All calculations were carried out with the Gaussian 09 program (G09),[73] employing the B3LYP[74] functional with standard 6-31G+(d,p)[75] basis set to fully optimize the geometries of the complexes. All resultant stationary points were subsequently characterized by vibrational analyses.

Since a test calculation between two intermediates with the $C(SiMe_3)_3$ and CH_3 ligand showed the same relative energies with the full and model system, the abbreviated methyl model ligand was used for all further calculations. Additionally, we studied a unimolecular pathway rather than a bimolecular pathway. Since the same types of bonds are activated in a unimolecular or bimolecular process, the trends in energies determined for a monomeric system are expected to apply to potential bimolecular pathways while simplifying comparison between systems and pathways. While trends in the energies of the transition states were expected to remain the same comparing a unimolecular or bimolecular reaction mechanism, the absolute barriers to activation

might not remain the same. For this reason, while the calculated barriers are quite high, the different pathways may still be compared.

For the thermal reactivity of **4.2'**, two intermediates were calculated. The intermediate corresponding to reductive elimination (A) of two hydrides is 14.3 kcal/mol higher in energy than that corresponding to elimination via σ-bond metathesis (B). However, the transition states for formation of each intermediate are at similar energies ($\Delta\Delta G^{\ddagger}$ = 7.5 kcal/mol). The small energy difference favors σ-bond metathesis, but it is not significant enough to disregard either pathway given the high reaction temperature (100 °C). The transition state for the oxidative addition of the Cp C-H bond between the two intermediates was also calculated and was found to be 73.3 kcal/mol higher energy than the starting material, suggesting that the oxidative addition of this bond in a unimolecular system is thermally inaccessible (Figure 4.11). Despite the tendency for early metals to react *via* σ-bond metathesis rather than reductive elimination, the transition states for reductive elimination and σ-bond metathesis in this system were at similar energies and could not be differentiated with DFT calculations.

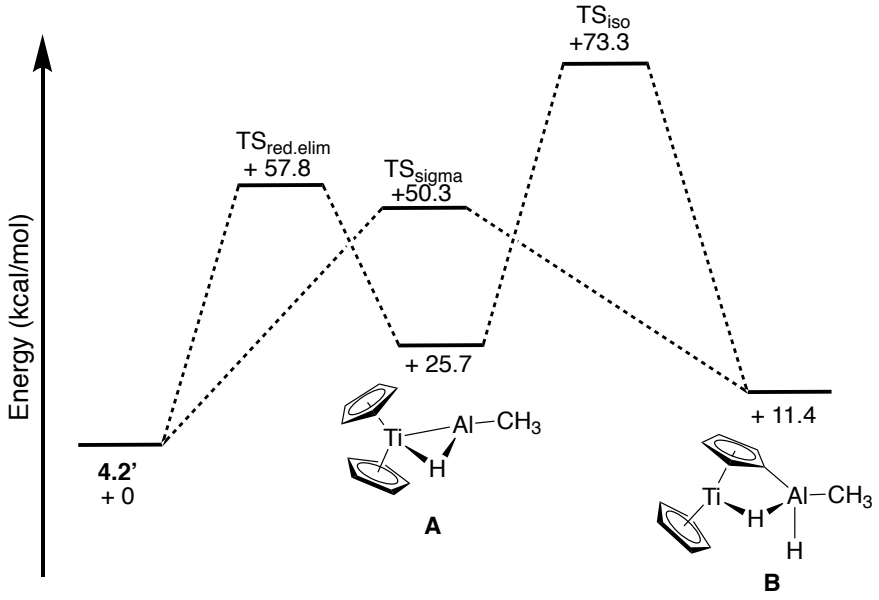

Figure 4.11. DFT Calculated reaction scheme for the conversion of **4.2'** to A and B

References

1 S. Satyapal, J. Petrovic, C. Read, G. Thomas and G. Ordaz, *Catal. Today*, 2007, **120**, 246–256.

2 R. Zidan, B. L. Garcia-Diaz, C. S. Fewox, A. C. Stowe, J. R. Gray and A. G. Harter, *Chem. Commun.*, 2009, **109**, 3717–3719.

3 S. Orimo, Y. Nakamori, J. R. Eliseo, A. Züttel and C. M. Jensen, *Chem. Rev.*, 2007, **107**, 4111–4132.

4 B. Sakintuna, F. Lamari-Darkrim and M. Hirscher, *Int. J. Hydrogen Energy*, 2007, **32**, 1121–1140.

5 J. Graetz, J. J. Reilly, V. A. Yartys, J. P. Maehlen, B. M. Bulychev, V. E. Antonov, B. P. Tarasov and I. E. Gabis, *J. Alloys Compd.*, 2011, **509S**, S517–S528.

6 E. Callini, A. Borgschulte, C. L. Hugelshofer, A. J. Ramirez-Cuesta and A. Züttel, *J. Phys. Chem. C*, 2014, **118**, 77–84.

7 J. Graetz, J. Reilly, G. Sandrock, J. Johnson, W. M. Zhou and J. Wegrzyn, *Aluminum Hydride, AlH_3, As A Hydrogen Storage Compound*, Upton, NY, 2006.

8 D. Sun, T. Kiyobayashi, H. T. Takeshita, N. Kuriyama and C. M. Jensen, *J. Alloys Compd.*, 2002, **337**, L8–L11.

9 B. Bogdanovic, M. Felderhoff, M. Germann, M. Hartel, A. Pommerin, F. Schuth, C. Weidenthaler and B. Zibrowius, *J. Alloys Compd.*, 2003, **350**, 246–255.

10 O. Ekkert, A. J. P. White, H. Toms and M. R. Crimmin, *Chem. Sci.*, 2015, **6**, 5617–5622.

11 T. Chu, I. Korobkov and G. I. Nikonov, *J. Am. Chem. Soc.*, 2014, **136**, 9195–9202.

12 C. Ganesamoorthy, S. Loerke, C. Gemel, P. Jerabek, M. Winter, G. Frenking and R. A. Fischer, *Chem. Commun.*, 2013, **49**, 2858–2860.

13 A. B. Altman, C. D. Pemmaraju, C. Camp, J. Arnold, S. G. Minasian, D. Prendergast, D. K. Shuh and T. Tyliszczak, *J. Am. Chem. Soc.*, 2015, **137**, 10304–10316.

14 D. Sun, S. S. Srinivasan, G. Chen and C. M. Jensen, *J. Alloys Compd.*, 2004, **373**, 265–269.

15 P. Wang and C. M. Jensen, *J. Alloys Compd.*, 2004, **379**, 99–102.

16 B. Bogdanović and M. Schwickardi, *Appl. Phys. A Mater. Sci. Process.*, 2001, **72,** 221–223.

17 T. Kiyobayashi, S. S. Srinivasan, D. Sun and C. M. Jensen, *J. Phys. Chem. A*, 2003, **107**, 7671–7674.

18 B. Bogdanović, M. Felderhoff, S. Kaskel, A. Pommerin, K. Schlichte and F. Schüth, *Adv. Mater.*, 2003, **15**, 1012–1015.

19 M. Fichtner, O. Fuhr, O. Kircher and J. Rothe, *Nanotechnology*, 2003, **14**, 778–785.

20 I. S. Chopra, S. Chaudhuri, J. F. Veyan and Y. J. Chabal, *Nat. Mater.*, 2011, **10**, 884–889.

21 A. R. Barron, J. E. Salt and G. Wilkinson, *J. Chem. Soc. Dalt. Trans.*, 1986, 1329–1332.

22 A. R. Barron, D. Lyons, G. Wilkinson, M. Motevalli, A. J. Howes and M. B. Hursthouse, *J. Chem. Soc. Dalt. Trans.*, 1986, 279–285.

23 A. R. Barron and G. Wilkinson, *Polyhedron*, 1986, **5**, 1897–1915.

24 G. S. Girolami, C. G. Howard, G. Wilkinson, H. M. Dawes, M. Thornton-Pett, M. Motevalli and M. B. Hursthouse, *J. Chem. Soc. Dalt. Trans.*, 1985, 921–929.

25 B. M. Bulychev, *Polyhedron*, 1990, **9**, 387–408.

26 B. M. Bulychev, S. E. Tokareva, G. L. Soloveichick and E. V. Evdokimova, *J. Organomet. Chem.*, 1979, **179**, 263–273.

27 E. B. Lobkovskii, G. L. Soloveichik, A. I. Sizov and B. M. Bulychev, *J. Organomet. Chem.*, 1985, **280**, 53–66.
28 E. B. Lobkovskii, G. L. Soloveichik, B. M. Bulychev, R. G. Gerr and Y. T. Struchkov, *J. Organomet. Chem.*, 1984, **270**, 45–51.
29 V. K. Bel'sky, A. I. Sizov, B. M. Bulychev and G. L. Soloveichik, *J. Organomet. Chem.*, 1985, **280**, 67–80.
30 E. B. Lobkovskii, A. I. Sizov, B. M. Bulychev, I. V. Sokolova and G. L. Soloveichik, *J. Organomet. Chem.*, 1987, **319**, 69–75.
31 E. B. Lobkovskii, G. L. Soloveichik, A. I. Sisov, B. M. Bulychev, A. I. Gusev and N. I. Kirillova, *J. Organomet. Chem.*, 1984, **265**, 167–173.
32 T. Y. Sokolova, A. I. Sizov, B. M. Bulychev, E. A. Rozova, V. K. Belsky and G. L. Soloveichik, *J. Organomet. Chem.*, 1990, **388**, 11–19.
33 A. I. Sizov, T. M. Zvakova, V. K. Belsky and B. M. Bulychev, *Russ. Chem. Bull.*, 1998, **47**, 1186–1192.
34 A. I. Sizov, I. V. Molodnitskaya, B. M. Bulychev, G. L. Soloveichik, *J. Organomet. Chem.*, 1988, **344**, 185–193.
35 A. I. Sizov, T. M. Zvukova, V. K. Belsky and B. M. Bulychev, *J. Organomet. Chem.*, 2001, **619**, 36–42.
36 A. I. Sizov, T. M. Zvukova, V. K. Belsky and B. M. Bulychev, *Russ. Chem. Bull.*, 2001, **50**, 2200–2202.
37 N. Etkin and D. W. Stephan, *Organometallics*, 1998, **17**, 763–765.
38 N. Etkin, A. J. Hoskin and D. W. Stephan, *J. Am. Chem. Soc.*, 1997, **119**, 11420–11424.
39 L. J. Guggenberger and F. N. Tebbe, *J. Am. Chem. Soc.*, 1973, **95**, 7870–7872.
40 F. N. Tebbe and L. J. Guggenberger, *J. Chem. Soc. Chem. Commun.*, 1973, 227-228.
41 J. Thomas, M. Klahn, A. Spannenberg and T. Beweries, *Dalton Trans.*, 2013, **42**, 14668–14672.
42 M. J. Butler and M. R. Crimmin, *Chem. Commun.*, 2017, **53**, 1348–1365.
43 R. Sun, J. Liu, S. Yang, M. Chen, N. Sun, H. Chen, X. Xie, X. You, S. Li and Y. Liu, *Chem. Commun.*, 2015, **51**, 6426–6429.
44 V. V. Gavrilenko, M. I. Vinnikova, V. A. Antonovich and L. I. Zakharkin, *Bull. Acad. Sci. USSR, Diu. Chem. Sci.*, 1982, 2084–2087.
45 C. Eaborn, S. M. El-Hamruni, M. S. Hill, P. B. Hitchcock, M. Hopman, A. Le Gouic and J. D. Smith, *J. Organomet. Chem.*, 2000, **597**, 3–9.
46 C. Eaborn, P. B. Hitchcock, J. D. Smith and S. E. Sözerli, *Organometallics*, 1998, **17**, 4322–4325.
47 K. Goto, J. Kobayashi and R. Okazaki, *Organometallics*, 1999, **18**, 1357–1359.
48 J. C. Fettinger, P. A. Gray, C. E. Melton and P. P. Power, *Organometallics*, 2014, **33**, 6232–6240.
49 R. J. Wehmschulte, J. J. Ellison, K. Ruhlandt-Senge and P. P. Power, *Inorg. Chem.*, 1994, **33**, 6300–6306.
50 C. Schnitter, H. W. Roesky, C. Röpken, R. Herbst-Irmer, H. G. Schmidt and M. Noltemeyer, *Angew. Chemie Int. Ed.*, 1998, **37**, 1952–1955.
51 C. Eaborn, I. B. Gorrell, P. B. Hitchcock, J. D. Smith and K. Tavakkoli, *Organometallics*, 1994, **13**, 4143–4144.
52 B. Cordero, V. Gómez, A. E. Platero-Prats, M. Revés, J. Echeverría, E. Cremades, F. Barragán and S. Alvarez, *Dalton Trans.*, 2008, **40**, 2832–2838.

53 S. S. Batsanov, *Inorg. Mater.*, 2001, **37**, 871–885.
54 D. F. Evans, *J. Chem. Soc.*, 1959, 2003–2005.
55 E. M. Schubert, *J. Chem. Educ.*, 1992, **69**, 62.
56 C. Piguet, *J. Chem. Educ.*, 1997, **74**, 815–816.
57 G. A. Bain and J. F. Berry, *J. Chem. Educ.*, 2008, **85**, 532–536.
58 R. J. Wehmschulte and P. P. Power, *Polyhedron*, 1999, **18**, 1885–1888.
59 K. Khan, C. L. Raston, J. E. Mcgrady, B. W. Skelton and A. H. White, *Organometallics*, 1997, **16,** 3252–3254.
60 S. Yow, S. J. Gates, A. J. P. White and M. R. Crimmin, *Angew. Chem. Int. Ed. Engl.*, 2012, **51**, 12559–125563.
61 J. E. Bercaw and H. H. Brintzinger, *J. Am. Chem. Soc.*, 1969, **91**, 7301–7306.
62 A. C. McQuilken, Q. M. Dao, A. J. P. Cardenas, J. A. Bertke, S. Grimme and T. H. Warren, *Angew. Chemie Int. Ed.*, 2016, **55**, 14335–14339.
63 F. G. N. Cloke, J. C. Green, M. L. H. Green and C. P. Morley, *J. Chem. Soc., Chem. Commun.*, 1985, 945–946.
64 M. E. Thompson, S. M. Baxter, A. R. Bulls, B. J. Burger, M. C. Nolan, B. D. Santarsiero, W. P. Schaefer and J. E. Bercaw, *J. Am. Chem. Soc.*, 1987, **109**, 203–219.
65 L. Oro and E. Sala, *Recent Advances in Hydride Chemistry*, Elsevier Science Ltd, 2001.
66 J. P. Collman, J. E. Hutchison, P. S. Wagenknecht, N. S. Lewis, M. A. Lopez and R. Guilard, *J. Am. Chem. Soc.*, 1990, **112**, 8206–8208.
67 E. Y.-J. Min, J. E. Bercaw, W. Bernskoetter and P. J. Chirik, *Inorg. Synth*., 2014, **36**, 47–51.
68 R. P. Spencer and J. Schwartz, *Tetrahedron*, 2000, **56**, 2103–2112.
69 R. S. P. Coutts, P. C. Wailes and R. L. Martin, *J. Organomet. Chem.*, 1973, **47**, 375–382.
70 A. H. Cowley, N. C. Norman, M. Pakulski, G. Becker, M. Layh, E. Kirchner and M. Schmidt, *Inorg. Synth.,* 1990, **27**, 235–240.
71 N. G. Connelly and W. E. Geiger, *Chem. Rev.*, 1996, **96**, 877–910.
72 N. A. Yakelis and R. G. Bergman, *Organometallics*, 2005, **24**, 3579–3581.
73 M. J. Frisch, G. W. Trucks, H. B. Schlegel, G. E. Scuseria, M. A. Robb, J. R. Cheeseman, G. Scalmani, V. Barone, G. A. Petersson, H. Nakatsuji, X. Li, M. Caricato, A. Marenich, J. Bloino, B. G. Janesko, R. Gomperts, B. Mennucci, H. P. Hratchian, J. V. Ortiz, A. F. Izmaylov, J. L. Sonnenberg, D. Williams-Young, F. Ding, F. Lipparini, F. Egidi, J. Goings, B. Peng, A. Petrone, T. Henderson, D. Ranasinghe, V. G. Zakrzewski, J. Gao, N. Rega, G. Zheng, W. Liang, M. Hada, M. Ehara, K. Toyota, R. Fukuda, J. Hasegawa, M. Ishida, T. Nakajima, Y. Honda, O. Kitao, H. Nakai, T. Vreven, K. Throssell, J. A. Montgomery, Jr., J. E. Peralta, F. Ogliaro, M. Bearpark, J. J. Heyd, E. Brothers, K. N. Kudin, V. N. Staroverov, T. Keith, R. Kobayashi, J. Normand, K. Raghavachari, A. Rendell, J. C. Burant, S. S. Iyengar, J. Tomasi, M. Cossi, J. M. Millam, M. Klene, C. Adamo, R. Cammi, J. W. Ochterski, R. L. Martin, K. Morokuma, O. Farkas, J. B. Foresman, and D. J. Fox, Gaussian, Inc., Wallingford CT, 2016.
74 C. Lee, W. Yang and R. G. Parr, *Phys. Rev. B*, 1988, **37**, 785–789.
75 P. C. Hariharan and J. A. Pople, *Mol. Phys.*, 1974, **27**, 209–214.

Chapter 5

Synthesis and Electronic Structure Investigations of Low-Valent M-Al Bimetallics (M= Ti(III), U(III) and Th(III))

Overview

Performed in parallel to the research outlined in Chapter 4, the following chapter describes the synthesis and characterization of low-valent thorium and uranium analogues to compound **4.2**. Together, these formed a series of isostructural molecules with different valence configurations, $3d^1$ (Ti), $6d^1$ (Th), and $5f^3$ (U), and with different extents of M-Al interactions. Synthetic work presented in the following chapter was supplemented with electron paramagnetic resonance characterization performed with Guodong Rao at the R. David Britt Group facility. Electronic structure analysis was supported by calculations performed by Laurent Maron. Additionally, Alexandra C. Brown provided assistance with synthesis of **4.1** and **4.2**, while Trevor D. Lohrey collected and analyzed X-ray diffraction data.

Introduction

Studies of molecular actinide coordination complexes have consistently demonstrated their unique behavior relative to s, p and d block compounds.[1] The combination of the expanded coordination sphere and increased radial extension of 5f and 6d orbitals due to relativistic effects leads to chemistry that resists understanding based on principles derived from other metals.[2-4] Of particular note is the unique low-valent chemistry demonstrated by uranium, driven by its reducing power and the ability of electrons in the 5f orbitals to engage in covalent interactions.[5-7] In comparison, the chemistry of thorium is relatively underexplored, in part due to the prevalence of its +4 oxidation state with no valence electrons and limited redox chemistry, although recent efforts indicate the high potential for discovering new modes of thorium bonding and reactivity.[8-13] While bonding in thorium complexes is mainly considered ionic, recent research has shown that its behavior also differs from the chemistry of isoelectronic group IV compounds, raising questions concerning the relative roles of the d and f orbitals in thorium-ligand bonding.[14] In order to evaluate and refine existing bonding models, we herein describe our efforts to promote covalent interactions in actinide complexes by synthesizing and characterizing electron rich low-valent thorium, uranium and group IV complexes.

While recent studies have explored relevant differences in bonding between low-valent thorium and uranium complexes,[15] such studies are limited by the scarcity low-valent thorium complexes on which to base comparisons.[16-24] The lack of diverse examples of low-valent thorium complexes has been attributed to the large energetic requirements for the reduction from thorium (IV) materials (+3.7 V vs. NHE relative to +0.6 V for U(IV)/(III) reduction) as well as the sensitivity and propensity for oxidation of isolated species.[25] One promising approach to diversifying thorium reduction chemistry relies on the inclusion of redox active ligands to act as electron reservoirs during redox transformations.[26-28] Most of these examples do not exhibit any low-valent thorium character; however, recent efforts indicated some ligand systems can be used to promote electron delocalization between the redox active ligand and the metal.[29] Similarly, incorporating an additional metal center that can interact cooperatively with thorium offers another potential route to delocalizing the increased electron density in low-valent compounds, an approach successfully used by Lu and coworkers to tune the electronic structure of late transition metal-group 13 bimetallics.[30-32] However, known thorium bimetallics are mainly limited to metals connected through bridging oxygens which rely on strong thorium-oxygen electrostatic interactions that create thermodynamic sinks.[33-38] Similarly, while a handful of complexes with direct thorium-metal bonds are known, they rely on M→Th donor-acceptor interactions that make them not well suited to support a low valent thorium center.[39-42] Thus, to explore the potential

reduction chemistry of thorium bimetallics, it was necessary to pursue systems containing less polarized bonds and less electron rich metals.

Recently, we reported the synthesis of a new titanium-aluminum bimetallic containing the Ti(III)-μH-Al motif.[43] Incorporation of a bulky anionic alanate ligand was shown to mitigate thermal instability and prevent formation of ill-defined polymeric structures previously observed in such systems for both early transition metals and actinides.[44-48] Furthermore, exposing this bimetallic to oxidizing agents did not result in the formation of an isolable Ti(IV) species. Instead, formal hydride oxidation was observed and only Ti(III) compounds were isolated. This reactivity could be understood in terms of recent spectroscopic and synthetic work demonstrating that some aluminum hydrides can support high electron density and undergo reduction chemistry.[49-51] We hypothesized that a similar effect would allow for the stabilization of analogous low-valent actinides using the same alanate ligand, and successfully pursued the synthesis and characterization of a low-valent thorium(III) aluminum heterobimetallic as well as a uranium(III) analogue. Electron paramagnetic resonance studies demonstrated significant aluminum contributions to the orbital containing the unpaired electron in the thorium bimetallic and density functional theory calculations confirmed the presence of a Th→Al interaction.

Results and Discussion

Synthesis of actinide-aluminum bimetallics. To synthesize actinide-aluminum heterometallics, salt-metathesis pathways were employed utilizing known actinide halides as well as $K[H_3AlC(SiMe_3)_3]$ (**4.1**) – an anionic alanate potassium salt recently used to synthesize a $Cp_2Ti(III)(\mu\text{-}H)_2Al(H)C(SiMe_3)_3$ (Cp^- = cyclopentadienyl) bimetallic from Cp_2TiCl (**4.2**).[43] Due to the lack of low-valent thorium starting materials, however, a different synthetic route was required. Initial reactions starting from tetravalent bis(di-*tert*-butylcyclopentadienyl) thorium dichloride (di-*tert*-butylcyclopentadienyl = $^{‡}Cp^-$) and **4.1** resulted in complete conversion to a mixture of two products: the targeted $^{‡}Cp_2ThCl(\mu\text{-}H)_3AlC(SiMe_3)_3$ (**5.1**), and $^{‡}Cp_2Th(H)(\mu\text{-}H)_3AlC(SiMe_3)_3$(**5.2**). From the reaction of $^{‡}Cp_2ThCl_2$ with 1.4 equivalents of **4.1** at low temperatures (0 °C), **5.1** could be isolated in poor yield upon multiple recrystallizations from HMDSO. Meanwhile, **5.2** was selectively synthesized in moderate yield by combining $^{‡}Cp_2ThCl_2$ with 2 equivalents of **4.1** in refluxing toluene (Scheme 5.1).

To improve the efficiency of synthetic routes to **5.1** and to allow for its use as a synthon for reduction chemistry, the chloride/hydride exchange chemistry of **5.2** was investigated. It was observed that **5.1** was converted to **5.2** upon addition of excess **4.1**, although no evidence of the predicted alane byproduct of this hydride transfer reaction was observed. Conversely, stoichiometric amounts of compound **5.2** reacted cleanly with both triphenylchloromethane and chlorotrimethylsilane to give **5.1** and either triphenylmethane or trimethylsilane as observed by ^1H NMR. This chemistry was harnessed to optimize a synthetic route to **5.2** in which a crude mixture of **5.1** and **5.2** was stirred with a commensurate amount of chlorotrimethylsilane, as determined by the ^1H NMR, to convert **5.2** into **5.1**. Evacuation of the solvent and silane byproduct *in vacuo* resulted in the isolation of **5.1** as a white powder in moderate yield (76 %) which could be used without further purification (see Experimental Details).

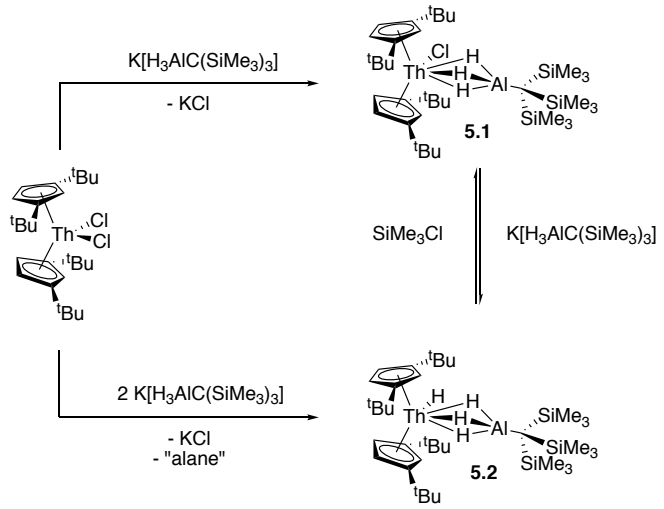

Scheme 5.1. Formation of interconversion of **5.1** and **5.2.**

To target the synthesis of a thorium analogue of the known low-valent titanium bimetallic, the reduction chemistry of **5.1** was explored. Due to the instability of **5.2** in ethereal and halogenated solvents (with the exception of diethyl ether), the chemical space to explore was inherently limited. Initial reactions between **5.1** and KC_8 in toluene resulted in an immediate color change to dark purple, although excess reducing agent and long reaction times (5 days) were needed to allow the reaction to go completion (Scheme 5.2). Dark purple crystals were isolated from concentrated HMDSO solutions stored at -40 °C. The ^{1}H NMR spectrum revealed that the crystals were a mixture of **5.2** and $^{\ddagger}Cp_2Th(\mu\text{-}H)_3AlC(SiMe_3)_3$ (**5.3**), the desired low-valent thorium bimetallic. The ^{1}H NMR spectrum of **5.3** in C_6D_6 consisted of two broad resonances. The resonance at 0.56 ppm was tentatively assigned to a proton in the trimethylsilyl group of the alanate moiety, and was therefore comparable to the resonance at 0.34 ppm corresponding to the trimethysilyl protons of **5.2**. Integration of these observed resonances suggested that the isolated product was ~1:1 mixture of **5.3**:**5.2**. The generation of Th(IV)-H is a known byproduct in the reduction chemistry of Th(IV) complexes to the Th(III) species, although the pathways for its formation remain not well understood.[21] In this instance, the ratio of **5.3**:**5.2** did not change significantly upon recrystallization of the sample or across independent syntheses under these conditions. Variable temperature NMR experiments over a range of temperatures (-60 - 100 °C) did not show significant changes in the ratio of **5.3**:**5.2**, although the paramagnetic resonances assigned to **5.3** broadened upon cooling and sharpened upon heating, as expected. Notably, these paramagnetically broadened peaks shifted according to the Curie law, suggesting that there were no significant temperature dependent equilibria over this temperature range that would require further consideration.[52]

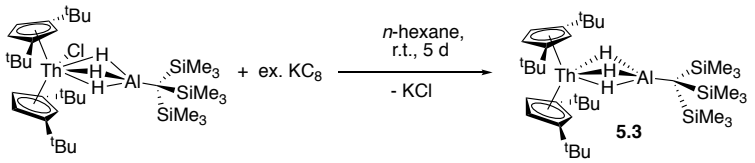

Scheme 5.2. Synthesis of **5.3.**

Together, these studies suggested that the relative ratio of **5.3**:**5.2** was determined during their formation and was fixed upon work up of the reaction mixture. Different reaction conditions

were explored and while similar ratios and yields were obtained for reductions performed with KC_8 in diethyl ether, alkane solvents gave different results. Reductions in hexane with a 4-fold excess KC_8 resulted in the isolation of crystalline purple material for which the ^{1}H NMR spectrum suggested was a 1.0:0.15:0.05 mixture of **5.3**:**5.2**:**5.1**. X-ray quality crystals of **5.3**, determined by ^{1}H NMR spectroscopy to contain a ~13% molar ratio of **5.2** were isolated upon recrystallization of this material and used for further characterization.

The solid-state structure of **5.3** was confirmed using X-ray diffraction techniques (see below). Additionally, the paramagnetism of **5.3** was measured using the Evans NMR method and it was found to have a magnetic moment, after diamagnetic correction, of 1.83 μ_B (c.f. the calculated spin-only value=1.73 μ_B). Optical spectroscopy was also observed to be consistent with known Th(III) compounds (Figure 5.1), which range in color from dark purple to dark green. The UV-vis absorption spectrum for **5.3** was similar in line shape and intensity to that observed for $^{‡}Cp_3Th$ and "Cp_3Th [bis(trimethylsilyl)cyclopentadienyl = "Cp_3] which both demonstrated three intense features between 450 – 680 nm with a maximum extinction coefficient (ε) of 7700 M^{-1} cm^{-1} (513 nm) and 5100 M^{-1} cm^{-1} (654 nm), in their respective UV-vis spectra, compared with 3999 M^{-1} cm^{-1} (520 nm) observed in the spectrum of **5.3**. [15,21] These multiple intense features have been previously assigned to dipole allowed d→f transitions, suggesting that, consistent with other observed Th(III) compounds, **5.3** has a d^1 ground state. This assignment was corroborated by EPR (see below).

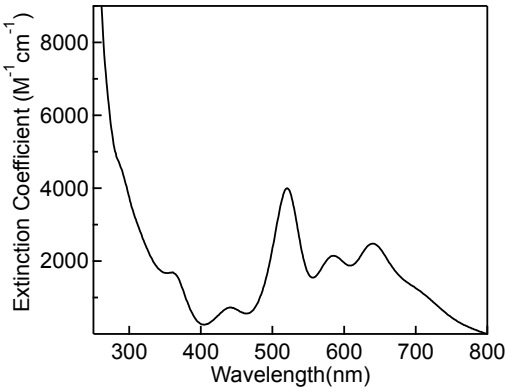

Figure 5.1. Optical spectrum of **5.3** in hexane collected at 295 K.

To gain insight into the behavior of this complex in solution, the oxidation chemistry of **5.3** was investigated. Analogously to what was reported for **4.2**, reactions to make the oxidized cation did not lead to isolable products and the evolution of hydrogen gas was observed. In comparison, stoichiometric amounts of copper (I) chloride was found to readily convert **5.3** to **5.1** without reacting with any of the **5.2** contaminant. Similarly, addition of triphenylchloromethane converted mixtures of **5.2** and **5.3** into **5.1** as well as triphenylmethane and Gomberg's dimer, indicative of the radical chemistry of **5.3**. While **5.3** was generally found to be very reactive towards small molecules such as O_2, CO, and isocyanates, often in unproductive ways, no change was observed upon heating to 100 °C over multiple days, unlike the previously reported chemistry of titanium aluminum hydrides.[43] The reactivity of **5.3** will be the focus of future work.

We also pursued the synthesis of a uranium analogue, which was expected to more closely mirror the behavior of the related titanium system due to the greater accessibility of redox transformations for both uranium and titanium as compared to thorium. Accordingly, while the reactions with tetravalent uranium dihalides resulted in intractable mixtures of tetravalent and

trivalent uranium species due to the reducing nature of alanate salts, reactions with trivalent uranium monohalides met with more success. The targeted bimetallic $^{‡}Cp_2U(\mu\text{-}H_3)AlC(SiMe_3)_3$ (**5.4**) was readily synthesized upon reacting trivalent $^{‡}Cp_2UI$ with a slight excess of **4.1** in toluene (Scheme 5.3). The resulting dark yellow compound was very soluble in non-coordinating solvents and could be isolated as crystalline material in moderate yield (51 %) from HMDSO. The room temperature magnetic susceptibility as measured with Evans NMR method as well as UV-vis and EPR spectroscopy were consistent with the formation of a U(III) f^3 system (see below), while the crystallographically determined solid-state structure was consistent with the targeted bimetallic.

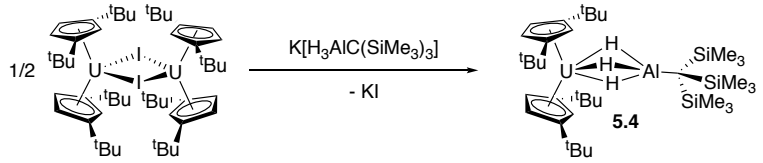

Scheme 5.3. Synthesis of **5.4.**

Structural characterization. All compounds could be characterized crystallographically and were found to be structurally similar (Figure 5.2) For each structure, the metal hydrides were explicitly located and freely refined, confirming that in each bimetallic, the two metals were bridged by all three hydrides of the alanate ligand. Additionally, only slight differences in bonding parameters were observed across all four compounds. In **5.1** and **5.2** this was readily attributed to differences in sterics between the hydride and chloride ligands, respectively, an effect perhaps best demonstrated by the $^{‡}Cp_{centroid}$-Th-$^{‡}Cp_{centroid}$ angles which varied from 117.34° to 121.97° for **5.1** and **5.2**, respectively. Similarly, for **5.2** and **5.3**, all bonds to the thorium center were shorter by 0.01-0.03 Å in the reduced species, consistent with other Th(III) and Th(IV) structural analogues and attributed to steric effects of the hydride.[22] Moreover, the Th-Al bond distance for each differed only slightly: 2.976(1) Å, 2.963(3) Å and 2.942(2) Å for **5.1**, **5.2**, and **5.3**, respectively. While these differences are most likely due to sterics as well, all these values are slightly shorter the sum of the covalent radii for these two atoms (1.75 Å (Th) + 1.26 Å (Al) = 3.01 Å),[53] raising the possibility of a direct Th-Al interaction, especially in the reduced complex. Analogously, the U-Al distance in **5.5** was 2.940(1) Å (c.f. 3.17 Å, the sum of the covalent radii of U and Al).[53]

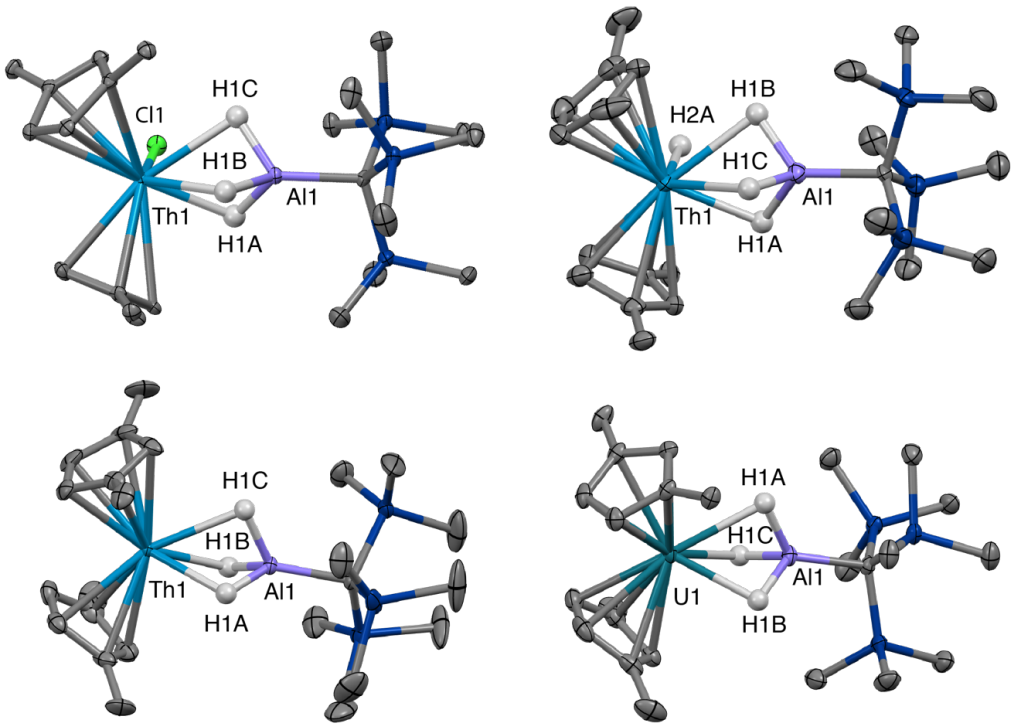

Figure 5.2. Crystallographically determined structures of **5.1** (top left), **5.2** (top right), **5.3** (bottom left) and **5.4** (bottom right). Thermal ellipsoids are shown at the 50% probability level. C-H hydrogens and *tert*-butyl methyl groups are omitted for clarity. Metal hydrides were located in the Fourier difference map and their positions were refined.

EPR spectroscopy. Together, **5.3**, **5.4**, and the previously reported $Cp_2Ti(\mu\text{-}H)_3AlC(SiMe_3)_3$ (**4.2**) form a series of compounds which maintain M-μH-Al motif while varying the orbitals involved in bonding from the Ti(III) $3d^1$ (**4.2**) to the Th(III) $6d^1$(**5.3**) and the U(III) $5f^3$ (**5.4**). To better understand the role these and the aluminum orbitals play in the bonding in the complexes, we employed EPR spectroscopy to study the hyperfine interaction (HFI) of the bridging hydrides and the aluminum. X-band (9 GHz) CW-EPR of **4.2** (2 mM in toluene) was observed up to room temperature. The solution EPR spectrum of **4.2** (200 K) exhibited striking features indicating HFI from the bridging hydride, Al, and Ti (Figure 5.3A). The spectrum was well-simulated with Al and two hydrides interacting with Ti(III) (Figure 5.3A, red trace), consistent with the crystallographically determined solid state structure. The isotropic hyperfine coupling constants were determined to be a_{iso} (^{27}Al, I = 5/2) = 9.4 MHz, a_{iso} ($^1H_{bridge}$) = 9.8 MHz, and a_{iso} (^{47}Ti, I = 7/2) = 17.4 MHz (shown in the zoom-in regions of Figure 5.3A), with the ^{27}Al HFI similar to that found in another Ti(III)-Al bimetallic system.[54] In frozen solution, EPR of **4.2** gave a slight rhombic g tensor that was not well-separated, with much less pronounced hyperfine features (Figure 5.3B). This g tensor was, however, much better resolved in Q-band (34 GHz) pseudo-modulated electron spin-echo detected field swept EPR spectrum (Figure 5.3C), with g = [2.004, 1.993, 1.971]. The g value for **4.2** is consistent with the $3d^1$ configuration of the Ti(III) ion, with d_z^2 ground state, and g_1=g_e>$g_{2,3}$.

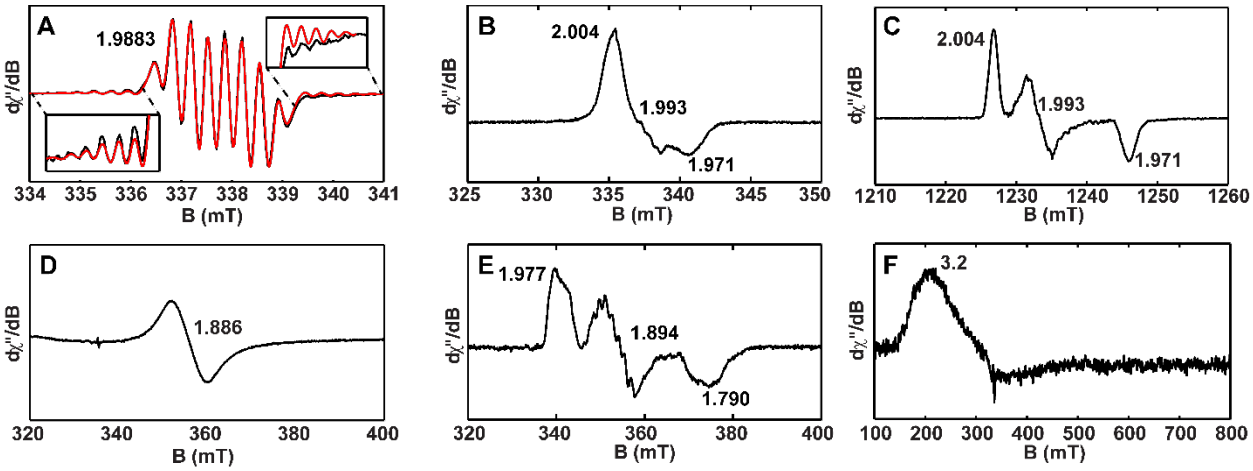

Figure 5.3. EPR spectrum of complexes **4.2**, **5.3**, and **5.4**. (A) X-band solution CW-EPR of **4.2**. Black trace: experimental data. Red trace: simulation. Shown zoomed-in are the wings of the spectrum showing the HFI from Ti. Conditions: temperature, 200 K; microwave power, 0.02 mW; modulation amplitude, 0.2 mT. (B) X-band frozen solution CW-EPR of **4.2**. Conditions: temperature, 50 K; microwave power, 0.01 mW; modulation amplitude, 0.1 mT. (C) Q-band pseudo-modulated electron spin-echo detected field swept EPR spectrum of **4.2**. Conditions: temperature, 30 K; τ = 300 ns; modulation amplitude, 0.2 mT. (D) X-band solution CW-EPR of **5.3**. Conditions: temperature, 230 K; microwave power, 0.5 mW; modulation amplitude, 0.5 mT. (E) X-band solution frozen solution CW-EPR of **5.3**. Conditions: temperature, 50 K; microwave power, 0.1 mW; modulation amplitude, 0.2 mT. (F) X-band solution frozen solution CW-EPR of **5.4**. Conditions: temperature, 6 K; microwave power, 0.02 mW; modulation amplitude, 0.5 mT.

Similar investigations were performed for complex **5.3**. The solution EPR spectrum of **5.3** (2 mM in toluene) showed a broad isotropic signal without any hyperfine features (Figure 5.3D) up to room temperature, while in frozen solution, a well-separated rhombic *g* tensor (*g* = [1.977, 1.894, 1.790]) was observed (Figure 5.3E). The larger separation of *g* values and deviation from g_e in complex **5.3**, compared to complex **4.2**, indicated much stronger spin-orbital coupling for thorium compared with titanium. These *g* values are consistent with previously reported data on other structurally similar Th(III) hydride systems (e.g. for K(18-crown-6)(Et_2O)][{"Cp_2ThH_2}$_2$ in THF at 77 K, g = [1.97, 1.91, 1.77]) and indicated a $6d^1$ configuration of the Th(III) ion.[16,18] However, notably different from previous thorium examples, we observed well-resolved HFI at the g_2 region, with a near sextet pattern and a coupling constant ~ 35 MHz. This splitting was attributed to ^{27}Al, similar to the case in the solution spectrum of **4.2**, albeit ~ 3x larger, indicating a stronger Th-Al covalent interaction.

In contrast to **4.2** and **5.3**, a broad and weak EPR spectrum for complex **5.4** (20 mM toluene) was only observed below 20 K. While the observed g_1 ~ 3.2 value was comparable to values observed for other $5f^3$ U(III) examples, [15,55] g_2 and g_3 remained unresolved even at 5 K (Figure 5.3F), probably due to faster spin relaxation rates for electrons in *f* orbitals as compared to *d* orbitals.[18] Currently, pulsed EPR experiments for complex **4.2** and **5.3** are in progress to further quantify differences in the M-Al interaction between 3d and 6d orbitals.

DFT Calculations. To gain further insight into the nature of this interaction, density functional theory was employed to analyze the valence orbitals in each complex (see Experimental Details). Visualizing the Singly Occupied Molecular Orbitals (SOMOs) confirmed that the

unpaired electron of **4.2** and **5.3** resided in orbitals of d_z^2 character along the axis perpendicular to the plane that bisects the Cp rings, with no evidence of f-orbital involvement for **5.3**, while the SOMOs of **5.4** consisted of three f orbitals (Figure 5.4).

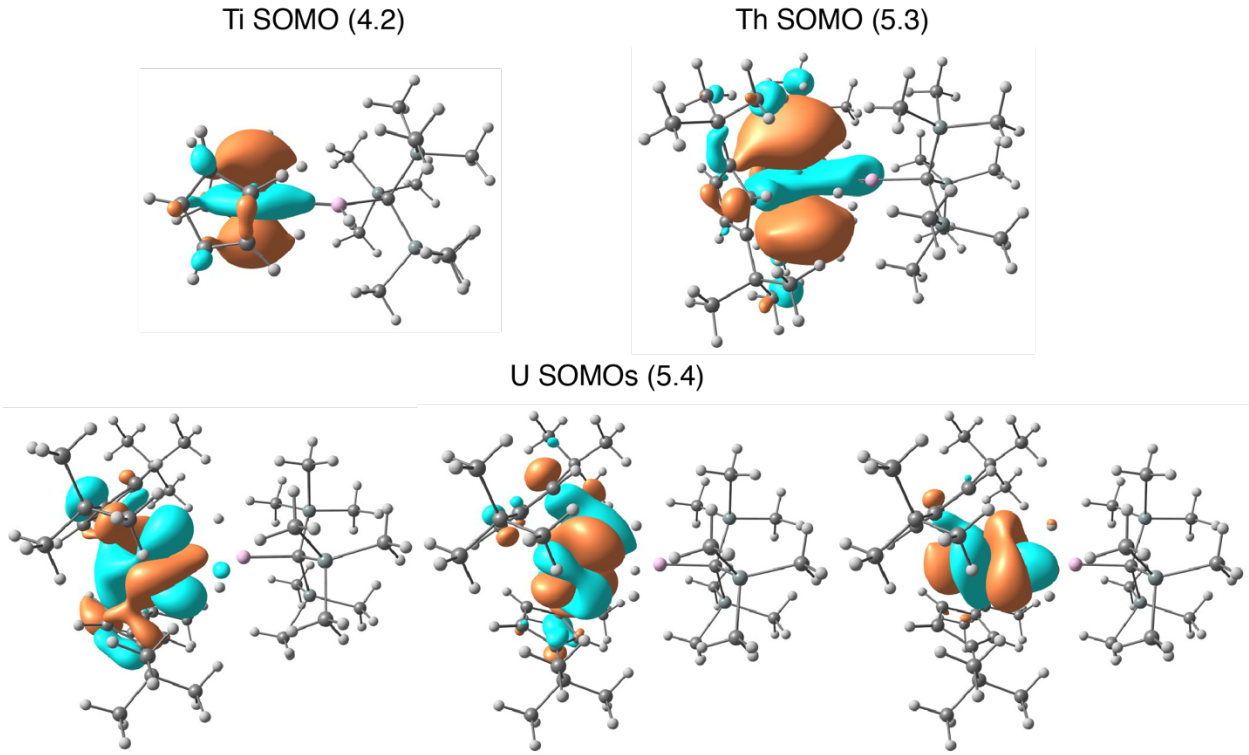

Figure 5.4. Visualization of the SOMOs of **4.2** (top left), **5.3** (top right) and **5.4** (bottom) demonstrating their M 3d, 6d and 5f origins, respectively. Aluminum atom is shown in pink.

Previous calculations have suggested that it is necessary to avoid destabilizing interactions between the SOMO orbital and ligand field in order to generate low-valent thorium; C_{3v} symmetry is common because the d_z^2 orbital remains non-bonding in a three-fold ligand environment.[56-58] However, in **5.3**, strict C_{3v} symmetry is broken, and the SOMO shows evidence of significant electron density between the thorium and aluminum, suggesting the presence of stabilizing Th-Al interaction. Examination of additional valence orbitals identified a bonding interaction in the SOMO-7 and SOMO-8 for both **5.3** and **5.4**, respectively, although none could be found for **4.2**. Furthermore, calculated Wiberg bond indices for **5.3** were found to be 0.38 between thorium and aluminum. In comparison, Wiberg bond indices of 0.07, and 0.29 were calculated for the Ti-Al, and U-Al interactions in **4.2** and **5.4**, respectively. The relative values for **4.2** and **5.3** are consistent with the trend observed from the HFI values in EPR. While these numbers are smaller than would be expected for full bonds, they are similar in magnitude to previous examples of weak donor-acceptor interactions between low valent metals and both thorium and uranium (M→An). [42,59] However, the metal-metal interactions in **5.3** and **5.4** have some metal to aluminum (An→Al) donating character, as confirmed by second order NBO analysis.

Together, the EPR and DFT results suggest that while the bonding between the metallocene fragment and the alanate ligand in these complexes is largely electrostatic, there are significant covalent metal-metal interactions. Therefore, the difference between **4.2** and **5.3** can be readily understood in terms of increased orbital overlap for the more diffuse Th 6d orbitals compared with

the Ti 3d orbitals. In comparison, the difference between **5.3** and **5.4** was found to be much smaller, and could also derive from small differences in orbital overlap due the greater radial extension of the 6d orbitals relative to the 5f orbitals.[60] Notably, the opposite trend was observed between the cyclopentadienyl ligands and the metal in $^{‡}Cp_3Th$ and $^{‡}Cp_3U$ systems,[15] suggesting that incorporation of an alanate ligand imparts significantly different electronic effects compared with previously studied systems. Spectroscopic and theoretical efforts to further understand and quantify the M-Al interaction will be the focus of future work.

Conclusions

Synthetic pathways to low-valent thorium and uranium bimetallics were presented. While structural investigations confirmed the presence of a M-μH-Al motif, significant structural differences across metals and oxidations states were not observed. In comparison, EPR studies of the thorium(III) species showed evidence of a covalent Th-Al interaction which was found to be stronger than in a previously reported titanium analogue. DFT calculations confirmed a metal-metal interaction, and suggested that it was most significant in the thorium system, small for titanium and intermediate for uranium. We posit that the Lewis acidic nature of aluminum allows it to stabilize the increased electron density present in the bimetallic upon reduction. Therefore, incorporation of other Lewis acidic motifs may be useful in expanding the chemistry of low-valent thorium. Similarly, this approach may be applied to other metals with large reduction potentials, such as the heavier group IV transitions metals, of which there are few examples of reduced species. Such complexes are likely to be very reactive; however, if their reactivity can be harnessed, they present promising systems for the development of new chemistry and chemical understanding.

Experimental Details

General Synthetic Details. All reactions were performed under an inert atmosphere either using standard Schlenk technique or in a MBraun glovebox (<0.5 ppm O_2/H_2O). Toluene, *n*-hexane, diethyl ether (Et_2O), tetrahydrofuran (THF) and dimethoxyethane (DME) were dried and degassed using the commercially available Phoenix Solvent Drying System from JC Meyer Solvent Systems. Hexamethyldisiloxane (HMDSO) and C_6D_6 and d^8-toluene were dried over sodium/benzophenone and vacuum transferred to a storage flask. Solution NMR spectra were collected on either Bruker AV-500, AV-600 or DRX-500 spectrometers. ^1H and $^{13}C\{^1H\}$ NMR chemical shifts (δ in ppm) were calibrated to residual solvent peaks. FT-IR samples were prepared as Nujol mulls and were taken between KBr disks using a Nicolet iS10 FT-IR spectrometer. Melting points were determined using an OptiMelt automated melting point system. UV−visible spectra were collected in hexane and determined with a Varian Cary 50 UV-visible spectrophotometer using a Schlenk-adapted 1 cm quartz cell. Elemental analyses were determined at the Microanalytical facility at University of California, Berkeley. All reagents were acquired from commercial sources and used without further purification. $Cp_2TiH_3AlC(SiMe_3)_3$ and $K[H_3AlC(SiMe_3)_3]$,[43] $K^{‡}Cp$[61], $UI_3(1,4\text{-dioxane})_{1.5}$,[62] $ThCl_4(DME)_2$[63] and KC_8[64] were synthesized according to previous literature procedures.

Synthesis of $^{‡}Cp_2ThCl_2$. A modified version of literature procedure was used.[65] A slurry of $K^{‡}Cp$ (3.28 g, 14.4 mmol) and $ThCl_4(DME)_2$ (4.00 g, 7.22 mmol) in THF (60 ml) was stirred for 2 days. Solvent was removed *in vacuo*, and the residue was extracted with *n*-hexane (2 x 40 ml) and filtered. The solution was concentrated until saturation and colorless crystals formed upon storage at -40 °C overnight (3.44 g, 72 % yield). ^1H-NMR data was consistent with reported values.

Synthesis of $^{‡}Cp_2ThClH_3AlC(SiMe_3)_3$ (5.1). A solution of $K[H_3AlC(SiMe_3)_3]$ (0.64 g, 2.1 mmol) in toluene (~25 ml) was added to a solution of $^{‡}Cp_2ThCl_2$ (1.00 g, 1.52 mmol) in toluene (25 ml). The reaction mixture was stirred for 1 h, and the solvent was removed *in vacuo*. The white residue was extracted into *n*-hexane (30 ml) and filtered through Celite®. The solvent was removed *in vacuo* and a ^{1}H-NMR spectrum of the resulting white solid was collected to determine the relative amount $^{‡}Cp_2Th(H)H_3AlC(SiMe_3)_3$ based on the observed integrations. The residue was dissolved in toluene (10 ml) and a stoichiometric amount of chlorotrimethylsilane relative to the $^{‡}Cp_2Th(H)H_3AlC(SiMe_3)_3$ was added. The reaction was stirred overnight. The solvent was removed *in vacuo* and the resulting white solid was found to be analytically pure and used directly for subsequent reactions (1.20 g, 89 % yield). X-ray quality crystals were grown from a HMDSO solution stored at room temperature for 4 days. ^{1}H NMR (500 MHz, C_6D_6, 293 K) δ 6.44 (m, 2H, Cp*H*), 6.29 (m, 4H, Cp*H*), 4.83 (s, 3H, Th-*H*-Al), 1.51 (s, 18H, C-C*H*$_3$), 1.37 (s, 18H, C-C*H*$_3$), 0.38 (s, 27H, Si-C*H*$_3$). ^{13}C{^{1}H} NMR (126 MHz, C_6D_6, 293 K) δ 150.93 (Cp), 149.89 (Cp), 115.40 (Cp), 115.03 (Cp), 113.66 (Cp). 34.24 (*C*-CH$_3$), 33.63 (*C*-CH$_3$), 32.69 (C-*C*H$_3$), 31.93 (C-*C*H$_3$), 5.36 (Si-*C*H$_3$). Anal calcd. (%) for $C_{36}H_{72}AlSi_3ThCl$: C, 48.93; H, 8.21 Found: C, 48.55; H, 8.36. MP: dec > 177°C. FT-IR (KBr, Nujol, cm^{-1}): 1710 (m, Al-H stretch), 1599 (w, Al-H stretch).

Synthesis of $^{‡}Cp_2Th(H)H_3AlC(SiMe_3)_3$ (5.2). A solution of $K[H_3AlC(SiMe_3)_3]$ (0.50 g, 1.7 mmol) in toluene (15 ml) was added to a solution of $^{‡}Cp_2ThCl_2$ (0.50 g, 0.76 mmol) in toluene (15 ml). The reaction mixture was refluxed for 2 days, and the solvent was removed *in vacuo*. The residue was extracted into *n*-hexane (30 ml) and filtered through Celite ®, and the solvent was removed *in vacuo*. The residue was extracted into 10 ml of HMDSO, and concentrated to saturation (~2 ml). The solution was stored at -40 °C overnight to afford colorless crystals of the desired product (0.32 g, 50. % yield). ^{1}H NMR (500 MHz, C_6D_6, 293 K) δ 15.11 (s, Th*H*), 5.85 (m, 2H, Cp*H*), 5.71 (m, 4H, Cp*H*), 3.49 (s, 3H, Th-*H*-Al), 1.59 (s, 18H, C-C*H*$_3$), 1.36 (s, 18H, C-C*H*$_3$), 0.34 (s, 27H, Si-C*H*$_3$). ^{13}C{^{1}H} NMR (126 MHz, C_6D_6, 293 K) δ 150.12 (Cp), 146.94 (Cp), 110.48 (Cp), 110.29 (Cp), 107.94 (Cp). 33.28 (C-*C*H$_3$), 33.24 (*C*-CH$_3$), 33.13 (C-*C*H$_3$), 32.74 (*C*-CH$_3$), 5.11 (Si-*C*H$_3$). MP: dec > 173°C. FT-IR (KBr, Nujol, cm^{-1}): 1682 (m, Al-H stretch), 1602 (w, Al-H stretch). Anal calcd. (%) for $C_{36}H_{72}AlSi_3Th$: C, 50.91; H, 8.66 Found: C, 50.54; H, 8.43.

Synthesis of $^{‡}Cp_2ThH_3AlC(SiMe_3)_3$ (5.3). A solution of $^{‡}Cp_2ThClH_3AlC(SiMe_3)_3$ (0.35 g, 0.40 mmol) in *n*-hexane (6 ml) was added to a stirring suspension of KC_8 (0.083 mg, 0.60 mmol) in *n*-hexane (4 ml) to produce a dark purple solution. The reaction was stirred for 24 h and an additional 1.5 equivalents of KC_8 (0.083 mg, 0.60 mmol) were added to the stirring solution. The reaction was stirred for 4 additional days, and the solvent was removed *in vacuo*. The dark purple residue was extracted into HMDSO and filtered through Celite®. The purple solution was concentrated to saturation, and storage of the solution at -40 °C overnight afforded the desired product as dark purple crystals (0.116 g of 83 % purity as determined by ^{1}H NMR, 28 % yield). ^{1}H NMR (600 MHz, C_6D_6, 293 K) δ 5.81 (s, br), 0.56 (s, br). UV-vis, [nm, ε (M^{-1} cm^{-1}) 360., 1694; 440., 730.; 520, 3999; 585, 2150.; 640., 2482. MP: dec > 190.5 °C.FT-IR (KBr, Nujol, cm^{-1}): 1674 (m, Al-H stretch). Anal calcd. (%) for $C_{36}H_{72}AlSi_3Th$: C, 50.98; H, 8.56 Found: C, 50.68; H, 8.32. μ_{eff}=1.83 μ_B at 297.1 K.

Synthesis of $[^{‡}Cp_2UI]_2$. An adaptation of literature procedure for the synthesis of $[^{‡}Cp_2UCl]_2$ was used.[66] $UI_3(1,4\text{-dioxane})_{1.5}$ was dissolved in THF and stirred for 30 minutes, then the solvent was removed *in vacuo*. The dark blue solid was dissolved in THF, and a solid suspension of K‡Cp in THF was added. The reaction mixture was stirred for 16 hours resulting in a dark green solution. The solvent was removed *in vacuo*. The residue was extracted with hexane, and the green solution

was filtered through Celite®. The solvent was removed *in vacuo* and the crude green solid was used without further characterization. The IR spectrum was consistent with previous literature reports.[52]

Synthesis of $^{‡}Cp_2UH_3AlC(SiMe_3)_3$ (5.4). A solution of $K[H_3AlC(SiMe_3)_3]$ (0.12 g, 0.40 mmol) in toluene (4 ml) was added to a solution of $[^{‡}Cp_2UI]_2$ (0.25 g, 0.35 mmol) in toluene (6 ml) to produce a brown solution. The reaction mixture was stirred overnight, and the solvent was removed *in vacuo*. The brown residue was triturated with *n*-hexane and extracted with HMDSO (10 ml). The brown solution was filtered through Celite®, and concentrated until saturated (~ 4 ml). Storage of the solution at -40 °C overnight afforded the desired product as dark yellow crystals (0.12 g). A second crop was isolated upon further concentration of the remaining solution (0.033 g, 51% total yield). ^{1}H NMR (500 MHz, C_6D_6, 293 K) δ 40.93 (s, br), 2.15 (s, br), -14.03 (s, br), -32.28 (s, br). UV-vis, [nm, ε (M^{-1} cm^{-1}) 337, 2282; 411, 816; 475, 299. MP: dec > 185 °C.FT-IR (KBr, Nujol, cm^{-1}): 1580 (w, Al-H stretch). Anal calcd. (%) for $C_{36}H_{72}AlSi_3U$: C, 50.62; H, 8.50 Found: C, 50.46; H, 8.53. μ_{eff}=2.88 μ_B at 296.8 K.

X-ray Crystallographic Methods. X-ray diffraction data for $^{‡}Cp_2ThClH_3AlC(SiMe_3)_3$ and $^{‡}Cp_2UH_3AlC(SiMe_3)_3$ were collected at CheXray, Berkeley, CA, using a Bruker APEX II QUAZAR instrument outfitted with a microfocus Mo Kα radiation source (λ = 0.71073 Å). Diffraction data for $^{‡}Cp_2Th(H)H_3AlC(SiMe_3)_3$ and $^{‡}Cp_2ThH_3AlC(SiMe_3)_3$ were obtained at the Advanced Light Source (ALS), Lawrence Berkeley National Laboratory, Berkeley, CA, station 11.3.1, using a silicon-monochromated beam of 16 keV (λ = 0.7749 Å) radiation. All data collections were conducted at 100 K. Absorption corrections were performed by a multiscan method, utilizing either Bruker AXS SADABS or TWINABS ($^{‡}Cp_2Th(H)H_3AlC(SiMe_3)_3$) as appropriate.[67] Bruker APEX3 software was used for the data collection, and Bruker SAINT software conducted the cell refinement and data reduction procedures.[68] Initial structure solutions were found using direct methods (SHELXT) and were refined by SHELXL-2014.[69] All non-hydrogen atoms in all structures were refined anisotropically. Hydrogen atoms bound to or bridging between metal centers could be explicitly located in all structures and were refined isotropically with no restraints.

Table 5.1 Crystallographic details for compounds **5.1-5.4.**

	5.1	**5.2**	**5.3**	**5.4**
Chemical formula	$C_{36}H_{72}AlSi_3ThCl$	$C_{36}H_{73}AlSi_3Th$	$C_{36}H_{72}AlSi_3Th$	$C_{36}H_{72}AlSi_3U$
Formula weight	883.67	849.23	848.22	854.21
Color, habit	Colorless, block	Colorless, plate	Purple, tablet	Brown, blocks
Temperature (K)	100(2)	100(2)	100(2)	100(2)
Crystal system	Monoclinic	Monoclinic	Monoclinic	Triclinic
Space group	P 2_1/n	P 2_1/c	P 2_1/m	P -1
a (Å)	14.6013(10	18.541(16)	12.933(8)	10.4534(5)
b (Å)	16.3421(10)	12.528(10)	12.816(8)	12.8540(6)
c (Å)	18.0401(11)	105.644(9)	13.179(8)	17.8476(8)
α (°)	90	90	90	72.090(2)
β (°)	93.323(3)	105.644(9)	94.460(4)	79.893(2)
γ (°)	90	90	90	66.898(2)
V (Å^3)	4297.4(5)	4243(6)	2178(2)	2094.82(17)
Z	4	4	2	2
Density (Mg m^{-3})	1.366	1.329	1.294	1.354
F(000)	1800	1736	866	870
Radiation Type	MoK_α	Synchrotron	Synchrotron	MoK_α
μ (mm^{-1})	3.658	1.962	1.912	4.002
Crystal size	0.20 x 0.20 x 0.10	0.04 x 0.03 x 0.01	0.09 x 0.06 x 0.02	0.2 x 0.2 x 0.2
Meas. Refl.	133659	35013	22006	58071
Indep. Refl.	7921	7699	5198	7694
R(int)	0.0542	0.1080	0.0346	0.0239
Final R indices	R = 0.0254	R = 0.0477	R = 0.0240	R = 0.0188
[I > 2σ(I)]	R_w = 0.0561	R_w = 0.0840	R_w = 0.571	R_w = 0.0437
Goodness-of-fit	1.142	1.034	1.059	1.040
$\Delta\rho_{max}$, $\Delta\rho_{min}$, (e Å^{-3})	2.709, -0.948	2.533, -1.962	1.431, -1.273	1.163, -0.911

EPR spectroscopy. EPR spectroscopy was performed in the Cal-EPR center in Department of Chemistry, University of California at Davis. CW-EPR experiments were performed on the Bruker Biospin EleXsys E500 spectrometer with a super high Q resonator (ER4122SHQE) in perpendicular mode. Cryogenic temperature was achieved by using an ESR900 liquid helium cryostat with a temperature controller (Oxford Instrument ITC503) and gas flow controller. All continuous-wave (CW) EPR spectra were recorded under slow-passage, non-saturating conditions. Spectrometer settings were as following: conversion time = 30 ms, modulation frequency = 100 kHz, and parameters in the corresponding figure legends. Pulsed Q-band electron spin-echo detected field swept EPR (ESE-FS) was recorded on the Bruker Biospin EleXsys 580 spectrometer equipped with a R.A. Isaacson cylindrical TE_{011} resonator. Standard Hahn-echo pulse sequence (π/2-τ-π-τ-echo) was used for ESE-FS experiments. Simulations of EPR spectra were performed in Matlab 2014a with EasySpin 5.1.10 toolbox.[70]

DFT Calculations. Calculations were carried out at the DFT level using the B3PW91 hybrid functional with the Gaussian 09 suite of programs.[71] Thorium, uranium, titanium, aluminum and silicon atoms were treated with a relativistic effective core potential from the Stuttgart-Koln group together with their associated basis sets.[72] Standard polarized double- ζ 6-31G+(d,p) basis sets were used for carbon and hydrogen.[73] The geometry of each complex was optimized without any symmetry restrictions, and the nature of the minima were verified with frequency calculations.

References

1 T. E. Albrecht-Schmitt, *Organometallic and Coordination Chemistry of the Actinides*, Springer, Berlin, 2008, vol. 127.
2 G. Cavigliasso and N. Kaltsoyannis, *Dalton Trans.*, 2006, **112**, 5476–5483.
3 G. Cavigliasso and N. Kaltsoyannis, *Inorg. Chem.*, 2007, **46**, 3557–3565.
4 *Chemistry of the Actinides and Transactinides,* ed. L. R. Morss, N. M. Edelstein, J. Fuger, J. J. Katz, Springer, Dordrecht, 3rd ed*.,* 2008, vol. 1.
5 M. Ephritikhine, *Dalton Trans.*, 2006, **0**, 2501-2516.
6 H. S. La Pierre and K. Meyer, *Activation of Small Molecules by Molecular Uranium Complexes*, John Wiley & Sons, Inc., 2014.
7 S. T. Liddle, *Angew. Chem. Int. Ed.*, 2015, **54**, 8604–8641.
8 J.-C. Berthet, P. Thuéry, N. Garin, J.-P. Dognon, T. Cantat and M. Ephritikhine, *J. Am. Chem. Soc.*, 2013, **135**, 10003–10006.
9 E. Zhou, W. Ren, G. Hou, G. Zi, D.-C. Fang and M. D. Walter, *Organometallics*, 2015, **34**, 3637–3647.
10 C. Camp, N. Settineri, J. Lefèvre, A. R. Jupp, J. M. Goicoechea, L. Maron and J. Arnold, *Chem. Sci.*, 2015, **6**, 6379–6384.
11 N. L. Bell, L. Maron and P. L. Arnold, *J. Am. Chem. Soc.*, 2015, **137**, 10492–10495.
12 D. E. Smiles, G. Wu and T. W. Hayton, *Inorg. Chem.*, 2016, **55**, 9150–9153.
13 D. E. Smiles, G. Wu, P. Hrobárik and T. W. Hayton, *J. Am. Chem. Soc.*, 2016, **138**, 814–825.
14 B. M. Gardner, P. A. Cleaves, C. E. Kefalidis, J. Fang, L. Maron, W. Lewis, A. J. Blake and S. T. Liddle, *Chem. Sci.*, 2014, **5**, 2489–2497.
15 A. Formanuik, A.-M. Ariciu, F. Ortu, R. Beekmeyer, A. Kerridge, F. Tuna, E. J. L. McInnes and D. P. Mills, *Nature Chem*, 2016, **9**, 578–583.
16 R. R. Langeslay, M. E. Fieser, J. W. Ziller, F. Furche and W. J. Evans, *J. Am. Chem. Soc.*, 2016, **138**, 4036–4045.
17 P. C. Blake, N. M. Edelstein, P. B. Hitchcock, W. K. Kot, M. F. Lappert, G. V. Shalimoff and S. Tian, *J. Organomet. Chem.*, 2001, **636**, 124–129.
18 W. K. Kot, G. V. Shalimoff, N. M. Edelstein and M. A. Edelman, *J. Am. Chem. Soc.*, 1988, **110**, 986–987.
19 F. Ortu, A. Formanuik, J. R. Innes and D. P. Mills, *Dalton Trans.*, 2016, **45**, 7537–7549.
20 R. R. Langeslay, M. E. Fieser, J. W. Ziller, F. Furche and W. J. Evans, *Chem. Sci.*, 2015, **6**, 517–521.
21 R. R. Langeslay, G. P. Chen, C. J. Windorff, A. K. Chan, J. W. Ziller, F. Furche and W. J. Evans, *J. Am. Chem. Soc.*, 2017, **139**, 3387–3398.
22 J. R. Walensky, R. L. Martin, J. W. Ziller and W. J. Evans, *Inorg. Chem.*, 2010, **49**, 10007–10012.
23 J. S. Parry, Cloke, S. J. Coles and M. B. Hursthouse, *J. Am. Chem. Soc.*, 1999, **121**, 6867–6871.
24 N. A. Siladke, C. L. Webster, J. R. Walensky, M. K. Takase, J. W. Ziller, D. J. Grant, L. Gagliardi and W. J. Evans, *Organometallics*, 2013, **32**, 6522–6531.
25 L. J. Nugent, R. D. Baybarz and J. L. Burnett, *J. Phys. Chem.*, 1973, **77**, 1528-1539.
26 E. J. Schelter, R. Wu, J. M. Veauthier, E. D. Bauer, C. H. Booth, R. K. Thomson, C. R. Graves, K. D. John, B. L. Scott, J. D. Thompson, D. E. Morris and J. L. Kiplinger, *Inorg. Chem.*, 2010, **49**, 1995–2007.

27 I. Korobkov, S. Gambarotta and G. P. A. Yap, *Angew. Chem. Int. Ed.*, 2003, **42**, 814–818.
28 W. Ren, G. Zi and M. D. Walter, *Organometallics*, 2012, **31**, 672–679.
29 M. E. Garner, S. Hohloch, L. Maron and J. Arnold, *Organometallics*, 2016, **35**, 2915–2922.
30 P. A. Rudd, S. Liu, L. Gagliardi, J. Victor G Young and C. C. Lu, *J. Am. Chem. Soc.*, 2011, **133**, 20724–20727.
31 P. A. Rudd, N. Planas, E. Bill, L. Gagliardi and C. C. Lu, *Eur. J. Inorg. Chem.*, 2013, 3898–3906.
32 M. V. Vollmer, J. Xie and C. C. Lu, *J. Am. Chem. Soc.*, 2017, **139**, 6570–6573.
33 G. M. Smith, M. Sabat and T. J. Marks, *J. Am. Chem. Soc.*, 1987, **109**, 1854-1856.
34 M. Fairley, D. K. Unruh, S. Abeysinghe and T. Z. Forbes, *Inorg. Chem.*, 2012, **51**, 9491–9498.
35 D. K. Unruh, J. de Groot, M. Fairley, A. Libo, S. Miller and T. Z. Forbes, *Inorg. Chem.*, 2015, **54**, 1395–1404.
36 L. Salmon, P. Thuéry, E. Rivière and M. Ephritikhine, *Inorg. Chem.*, 2006, **45**, 83–93.
37 A. D. Sutton, I. May, C. A. Sharrad, M. J. Sarsfield and M. Helliwell, *Dalton Trans.*, 2006, **43**, 5734–5742.
38 O. J. Scherer, J. Schulze and G. Wolmershäuser, *J. Organomet. Chem.* 1994, **484**, C5–C7.
39 R. S. Sternal, C. P. Brock and T. J. Marks, *J. Am. Chem. Soc.*, 1985, **107**, 8270-8272.
40 P. J. Hay, R. R. Ryan, K. V. Salazar, D. A. Wrobleski and A. P. Sattelberger, *J. Am. Chem. Soc.*, 1986, **108**, 313-315.
41 A. L. Ward, W. W. Lukens, C. C. Lu and J. Arnold, *J. Am. Chem. Soc.*, 2014, **136**, 3647–3654.
42 P. Yang, E. Zhou, G. Hou, G. Zi, W. Ding and M. D. Walter, *Chem. Eur. J.*, 2016, **22**, 13845–13849.
43 A. C. Brown, A. B. Altman, T. D. Lohrey, S. Hohloch and J. Arnold, *Chem. Sci.*, 2017, **8**, 5153-5160.
44 A. R. Barron and G. Wilkinson, *Polyhedron*, 1986, **5**, 1897–1915.
45 M. Ephritikhine, *Chem. Rev.*, 1997, **97**, 2193–2242.
46 F. Ossola, N. Brianese, M. Porchia, G. Rossetto and P. Zanella, *J. Organomet. Chem.*, 1986, **310**, C1–C4.
47 N. Brianese, U. Casellato, F. Ossola, M. Porchia, G. Rossetto, P. Zanella and R. Graziani, *J. Organomet. Chem.*, 1989, **365**, 223–232.
48 F. Ossola, N. Brianese, M. Porchia, G. Rossetto and P. Zanella, *J. Chem. Soc., Dalton Trans.*, 1990, **0**, 877–880.
49 A. B. Altman, C. D. Pemmaraju, C. Camp, J. Arnold, S. G. Minasian, D. Prendergast, D. K. Shuh and T. Tyliszczak, *J. Am. Chem. Soc.*, 2015, **137**, 10304-104316.
50 C. Ganesamoorthy, S. Loerke, C. Gemel, P. Jerabek, M. Winter, G. Frenking and R. A. Fischer, *Chem. Commun.*, 2013, **49**, 2858–2860.
51 O. Ekkert, A. J. P. White, H. Toms and M. R. Crimmin, *Chem. Sci.*, 2015, **6**, 5617–5622.
52 W. W. Lukens, S. M. Beshouri, A. L. Stuart and R. A. Andersen, *Organometallics*, 1999, **18**, 1247–1252.
53 P. Pyykkö, M. Atsumi, *Chem. Eur. J.* 2009, **15**, 186-197.
54 E. Morra, E. Giamello, S. Van Doorslaer, G. Antinucci, M. D'Amore, V. Busico and M. Chiesa, *Angew. Chem. Int. Ed.*, 2015, **54**, 4857–4860.
55 W. W. Lukens, M. Speldrich, P. Yang, T. J. Duignan, J. Autschbach and P. Kögerler, *Dalton Trans.*, 2016, **45**, 11508–11521.

56 B. E. Bursten and L. F. Rhodes, *J. Am. Chem. Soc.* 1989, **111**, 2756-2758.
57 B. E. Bursten and L. F. Rhodes, *J. Am. Chem. Soc.*, 1989, **111**, 2758–2766.
58 J. S. Parry, Cloke, S. J. Coles and M. B. Hursthouse, *J. Am. Chem. Soc.*, 1999, **121**, 6867–6871.
59 S. G. Minasian, J. L. Krinsky, V. A. Williams and J. Arnold, *J. Am. Chem. Soc.*, 2008, **130**, 10086–10087.
60 M. L. Neidig, D. L. Clark and R. L. Martin, *Coord. Chem. Rev.*, 2013, **257**, 394–406.
61 W. W. Lukens, S. M. Beshouri, L. L. Blosch, A. L. Stuart and R. A. Andersen, *Organometallics*, 1999, **18**, 1235–1246.
62 M. J. Monreal, R. K. Thomson, T. Cantat, N. E. Travia, B. L. Scott and J. L. Kiplinger, *Organometallics*, 2011, **30**, 2031–2038.
63 T. Cantat, B. L. Scott and J. L. Kiplinger, *Chem. Commun.*, 2010, **46**, 919–921.
64 M. A. Araya, F. A. Cotton, J. H. Matonic and C. A. Murillo, *Inorg. Chem.*, 1995, **34**, 5424–5428.
65 W. Ren, G. Zi, D.-C. Fang and M. D. Walter, *Chem. Eur. J.*, 2011, **17**, 12669–12682.
66 A. Zalkin, A. L. Stuart and R. A. Andersen, *Acta Crystallogr. C Struct. Chem.*, 1988, **44**, 2106–2108.
67 SADABS: Bruker-Nonius Area Detector Scaling and Absorption, V2.05, Bruker Analytical X-ray Systems Inc., Madison, WI, 2003.
68 SAINT: SAX Area-Detector Integration Program, V6.40, Bruker Analytical X-ray Systems, Inc., Madison, WI, 2001–2003.
69 G. M. Sheldrick, *Acta Crystallogr. C Struct. Chem.*, 2015, **71**, 3–8.
70 S. Stoll and A. Schweiger, *J. Magn. Reson.*, 2006, 1**78**, 42-55.
71 M. J. Frisch, G. W. Trucks, H. B. Schlegel, G. E. Scuseria, M. A. Robb, J. R. Cheeseman, G. Scalmani, V. Barone, G. A. Petersson, H. Nakatsuji, X. Li, M. Caricato, A. Marenich, J. Bloino, B. G. Janesko, R. Gomperts, B. Mennucci, H. P. Hratchian, J. V. Ortiz, A. F. Izmaylov, J. L. Sonnenberg, D. Williams-Young, F. Ding, F. Lipparini, F. Egidi, J. Goings, B. Peng, A. Petrone, T. Henderson, D. Ranasinghe, V. G. Zakrzewski, J. Gao, N. Rega, G. Zheng, W. Liang, M. Hada, M. Ehara, K. Toyota, R. Fukuda, J. Hasegawa, M. Ishida, T. Nakajima, Y. Honda, O. Kitao, H. Nakai, T. Vreven, K. Throssell, J. A. Montgomery, Jr., J. E. Peralta, F. Ogliaro, M. Bearpark, J. J. Heyd, E. Brothers, K. N. Kudin, V. N. Staroverov, T. Keith, R. Kobayashi, J. Normand, K. Raghavachari, A. Rendell, J. C. Burant, S. S. Iyengar, J. Tomasi, M. Cossi, J. M. Millam, M. Klene, C. Adamo, R. Cammi, J. W. Ochterski, R. L. Martin, K. Morokuma, O. Farkas, J. B. Foresman, and D. J. Fox, Gaussian, Inc., Wallingford CT, 2016.
72 W. Küchle, M. Dolg, H. Stoll and H. Preuss, *Mol. Phys.*, 1991, **74**, 1245–1263.
73 P. C. Hariharan and J. A. Pople, *Mol. Phys.*, 2006, **27**, 209–214.

Future Directions

Overview

While aluminum is traditionally well regarded as a Lewis acidic, electropositive metal, the results presented in the previous five chapters illustrate ways in which "unusual" aluminum behavior can be harnessed to perform new chemistry with f-elements. However, there remain some fundamental questions about the generality of the observations and the limits of the synthetic techniques. Nevertheless, the tools and techniques described can be easily applied to a variety of systems. The focus of the following chapter will be to highlight some promising areas for further study both spectroscopically and synthetically.

Al K-edge XAS

The results presented in this work illustrate the rich information Al K-edge XAS can provide for even simple molecular systems. For example, Chapter 1 demonstrated the electron rich character of the BDI supported aluminum dihydride suggesting that covalency is an important part of the Al-H bond. Such a model can be used to explain recent examples in aluminum chemistry of aluminum hydrides undergoing redox events under mild conditions (*Chem. Commun.* **2013**, *49*, 2858-2850); however, further studies are necessary to explore whether this model applies more generally. To this end, efforts have begun to synthesize and characterize more aluminum hydrides beginning with the Cp* ligand system which stabilizes a diverse array of aluminum complexes in various oxidation states and coordination environments (Figure FD.1). The main pre-edge feature in each spectrum was assigned to π type interactions between the Al 3p orbitals and the Cp* aromatic p orbital system; however, further ground state calculations are needed to determine how the energy of this orbital and the core orbital change with changes in ligand environment and oxidation state. To expand this comparison, it would be useful to synthesize and characterize a series of simple alane, AlR_3, and alanate, AlR_4^-, complexes stabilized by different bases.

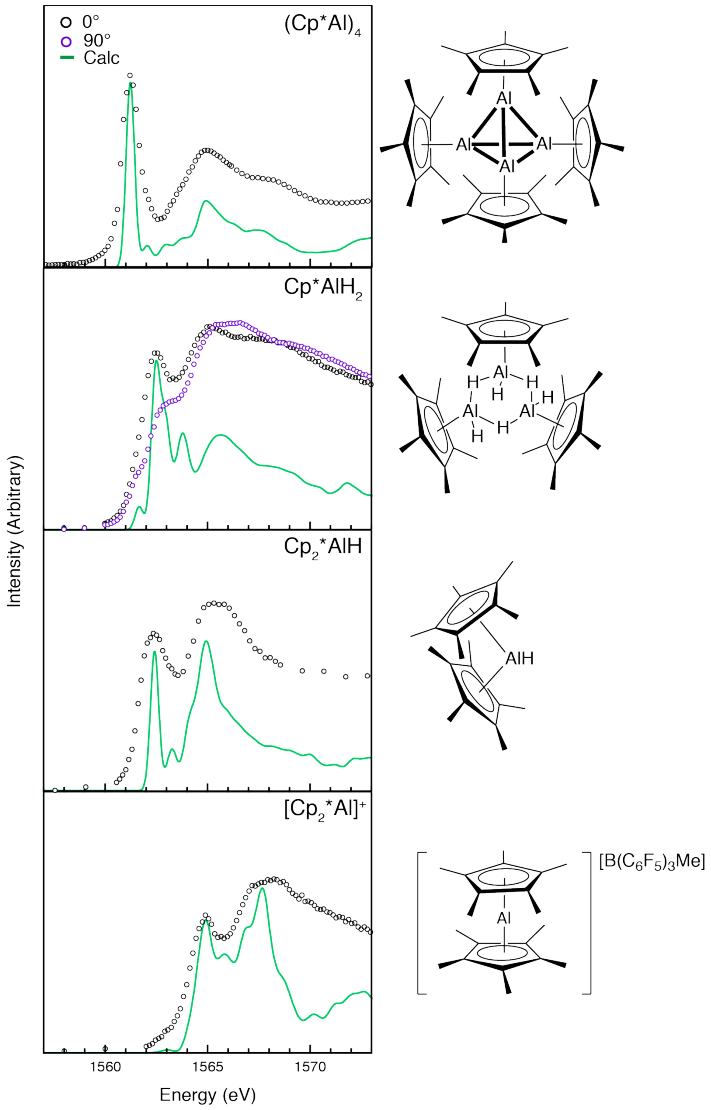

Figure FD.1 Al K-edge XAS observed (black and purple circles) and calculated (green line) spectra collected on a series of relevant Cp*Al compounds. $(Cp^*AlH_2)_3$ demonstrated polarization dependence.

Similarly, it is hypothesized that the geometry around aluminum centers greatly influences observed spectra, potentially obscuring other factors; however, this effect remains difficult to probe experimentally due to the lack of comparable but geometrically varied aluminum systems. While aluminum is most commonly found in a tetrahedral or octahedral environment, the Berben group at University of California, Davis, has implemented a tridentate bis(imino)pyridine ligand ($^{Ph}I_2P$) to stabilize a series of square planar aluminum complexes. Collaboration with this group has the potential to elucidate differences in electronic structure between square planar and tetrahedral aluminum, and preliminary studies comparing the isostructural square planar hydride with the chloride have been performed (Figure FD.2). The significant differences in observed features suggest that these may be productive analytes for in-depth study.

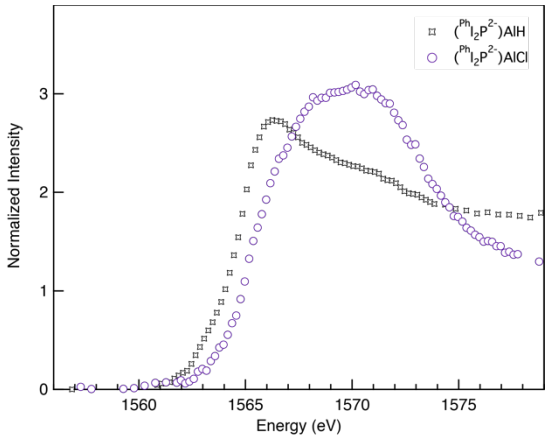

Figure FD.2 Al K-edge XAS spectra observed for a square-planar aluminum hydride (black squares) and chloride (purple diamonds) provided by the Berben group.

However, in general such compounds resist ready analysis due to their multimetallic structure and varied geometries, suggesting that theoretical tools will be vital for validating spectroscopic interpretations. The XCH approach used was remarkably successful at capturing relevant spectroscopic features across the BDI molecular systems as well as aluminum metal and f-element alloys, providing an accessible and low-cost computational tool for gaining fundamental information. One question raised during these studies is what energetic shift should be applied to calculated spectra to match observed data. Ideally, a constant should be used for all aluminum calculations, and one value was found to be consistent across the metallic systems. However, this approximation broke down for the molecular systems. Such issues need to be resolved or at least better understood to allow for successful "black box" style implementation using the WebXS tool developed in the Prendergast group at Lawrence Berkeley National Laboratory. The analytes described above provide a good starting point to further calibrate these calculations.

These fundamental studies will aid in the development of Al K-edge XAS as a technique that can be applied to a variety of systems with wide-ranging applications. For example, solution state capabilities are currently being developed at the Scanning Transmission X-ray Microscope (STXM) used for these Al K-edge measurements. The ability to study solution state transformations offers the tantalizing potential of detecting *in situ* generated species which are active in reactions such as Friedel Craft alkylation, Ziegler Natta alkene polymerization and frustrated Lewis pair chemistry. The detailed and element specific information provided by Al K-edge XAS has the potential to inform and improve the myriad of ways in which aluminum is already used.

Molecular aluminum heterobimetallics

Characterization: This work presents preliminary characterization of the first low-valent thorium heterobimetallic molecular complex using Continuous Wave (CW) EPR to highlight the unique aspects of its electronic structure; however, additional characterization remains to be explored. In particular, aluminum specific characterization would provide a complimentary "perspective" that can be compared directly across the series. While Al K-edge XAS has high potential for providing such information, the sensitivity of **5.3** has been prohibitive, and while preliminary results are presented in Figure FD.3, they resist ready explanation. Spectral simulations that incorporate higher levels of theory are needed to describe these open shell systems. In the

meantime, pulsed ^{27}Al Electron Nuclear Double Resonance (ENDOR) experiments have been performed to compliment CW results and will be the subject of a future publication.

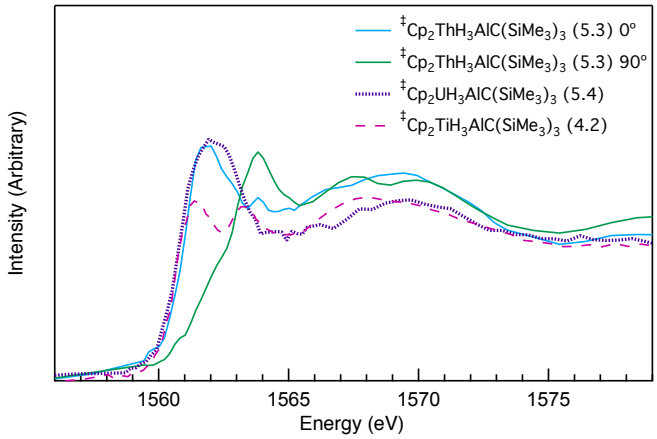

Figure FD.3 Al K-edge XAS spectra of **4.2** (long dashed pink line), **5.3** (solid blue and green line), and **5.4** (short dashed purple line). Both **4.2** and **5.3** exhibited polarization effects, and while representative spectra of relevant features are displayed, intensities were dependent on analyte alignment with incoming beam and are not comparable.

Reactivity studies could also prove useful in revealing relevant differences in electronic structure. For example in the titanium systems, while **4.10** was isolated upon oxidation of **4.2** with silver triflate, limited oxidation chemistry was explored for the thorium and uranium analogues. Preliminary results suggested that the **5.3** also undergoes hydrogen evolution upon exposure to oxidizing agents (other than copper chloride), which may result in a new low-valent species. In comparison, electrochemical studies suggest that **5.4** may be more tolerant of redox chemistry (Figure FD.4). The observed reversibility in the cyclic voltammogram of the event assigned to the U(III)/(IV) couple suggests that an oxidized species may be isolable.

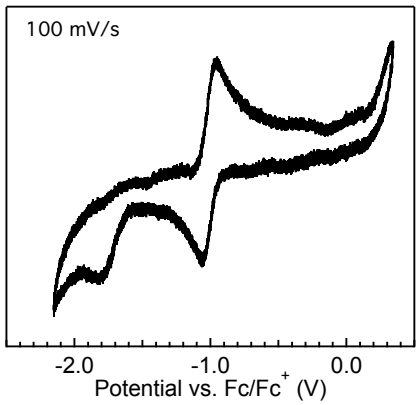

Figure FD.4 Cyclic voltammogram of complex **5.4** in 0.1 M solution of NBu_4BAr_{F20} in 1,2 difluorobenzene at 25 °C. The feature at ~ -1.0 V was assigned to the U(III)/(IV) couple, while the irreversible feature at ~-1.8 V was present in the background.

These low-valent actinide species may perform unique chemical transformations. To this end, comparable reactivity to what was explored for the titanium system should be studied for the thorium and uranium systems as well. While the sensitivity of **5.3** has proven limiting, uranium(III) compounds are known to perform productive reduction chemistry (*Angew. Chem.*

Int. Ed. **2015**, *54*, 8604-8641). The Al-H motif in **5.4** may promote reduction coupled with hydride transfer, an important but challenging step in the activation of small molecules.

Synthesis: The synthetic pathways developed in this work appear readily adaptable to other trivalent systems. Of immediate interest are trivalent lanthanides, such as cerium and neodymium, as 4f analogues for the actinide systems studied. Similarly, heavier group IV metals provide important 4d and 5d analogues to the titanium and thorium systems, but due to the lack of low-valent examples of these metals, they would be interesting compounds to isolate and study in their own right.

Lastly, while the alanate system was chosen because the tris(trimethysilyl)methyl ligand is the only known ligand to stabilize a low-valent aluminum center and an anionic alanate species, it presents multiple variables for systematic variation. One aspect to explore includes the use of alanate ligands with only two hydrides available for coordination, which may potentially open up additional coordination sites on the other metal. Similarly, gallium hydride chemistry can be pursued to introduce additional redox behavior. Such studies would address the underlying question raised by this work: is aluminum necessary for stabilizing low-valent heterobimetallics, or can this approach be used more generally to access low-valent actinide chemistry?